M 2021

U.PORTO
FEUP FACULDADE DE ENGENHARIA
UNIVERSIDADE DO PORTO

INVESTIGATION OF STRESSORS FOR PEMFC IN DIFFERENTIAL CELL FOR TRANSPORT APPLICATIONS

RAQUEL CARDOSO MOREIRA DE VASCONCELOS RIBEIRO

CHEMICAL ENGINEERING

MASTER THESIS´ DISSERTATION PRESENTED

TO ENGINEERING FACULTY OF PORTO UNIVERSITY

Integrated Master´s in Chemical Engineering

Investigation of Stressors for PEMFC in differential cell for transport applications

Master dissertation

of

Raquel Cardoso Moreira de Vasconcelos Ribeiro

Developed within the course of dissertation

Held in

German Aerospace Center (DLR) – Institute of Engineering Thermodynamics

Supervisor at FEUP: **Prof. Adélio Mendes**

Coordinator at DLR: **Dr. Krishan Talukdar**

Department of Chemical Engineering

October 2021

"Mudam-se os tempos, mudam-se as vontades,

Muda-se o ser, muda-se a confiança;

Todo o mundo é composto de mudança,

Tomando sempre novas qualidades"

Luís Vaz de Camões

Acknowledgment

I would like to start by thanking Professor K. Andreas Friedrich for accepting my application, giving me the possibility to work in DLR, which is such a prestigious and recognized research center. I want to express my gratitude to Dr. Krishan Talukdar for being such an amazing supervisor and an incredible person. Thank you for all the scientific knowledge, the guidance, and the motivation, that allowed me to finish my work. I appreciate the encouragement you gave me to always ask questions, the constant non-stop support, and the wise advice you shared with me. I want to show my deep appreciation to Dr. Pawel Gazdzicki for the regular meetings we had, the valuable scientific input shared, and for keeping track on my work and giving suggestions on how to improve it. I am grateful to my supervisor from FEUP, Professor Adélio Mendes, for always pushing me to do my best and providing me with great guidance during my work.

I want to thank all my colleagues and friends from DLR that contributed to an amazing working atmosphere. I owe a special thanks to Sofia Delgado, for the valuable and important knowledge she provided me regarding fuel cells and for taking my doubts and giving suggestions throughout all my research work at DLR. Thank you Indro Biswas, Ms. Ina Plock, Mr. Günter, Tobias Morawietz and Kim Mehnert for the excellent work you did in analyzing my samples with SEM and XPS. I want to thank Siegfried Graf for the testbench modifications that allowed me to complete all my experiments, and Nina, for teaching me how to use it. Cristóvão, thank you for the nice company during lunch and coffee breaks, and for checking my test bench water level.

Maria Inês, Cristóvão, Freddy and Jorge, thank you for being such good friends and for being the greatest company ever during these seven months in Stuttgart. Thank you, Fabian, for showing me the city when I first arrived in Germany. Thank you, Adrian, for the amazing travels that have kept my spirits up. A big heartfelt thanks to my dearest friends that always cheered me up, Magda Dias and Francisco Barbosa.

I want to give a special thanks for my family, especially my parents and my siblings, for all the constant support, love, and motivation. Thank you, mom, and dad, for encouraging me to go on this journey that allowed me to grow as a person and as a scholar. Thank you for all the long talks we had and for never letting me give up. I dedicate this thesis to you both.

Professor Adélio Mendes, supervisor of this dissertation is an integrated member of LEPABE – Laboratory for Process Engineering, Environment, Biotechnology and Energy, financially supported by: Base Funding - UIDB/00511/2020 of the Laboratory for Process Engineering, Environment, Biotechnology and Energy – LEPABE - funded by national funds through the FCT/MCTES (PIDDAC).

Abstract

Stability is one of the major challenges of the polymer electrolyte membrane fuel cells (PEMFCs) for transport applications, especially for heavy duty applications, as membrane electrode assembly (MEA) degrades over time, decreasing its performance and limiting its fast commercialization. The most typical **degradation mechanisms** of the MEA involve membrane degradation, due to mechanical and thermal stress, cathode catalyst layer (CCL) degradation as result of carbon corrosion, ionomer degradation, as well as platinum dissolution and sintering.

Fuel cell load cycles simulate the operating conditions that a fuel cell stack would experience during a vehicle operation. Moreover, the specific conditions within each cell of the stack are inhomogeneous, depending on gradients of gas concentrations, temperature and humidity along the gas flow channels. In this thesis, was given focus on the middle area condition of a flow field. From sophisticated driving cycle tests, performed with 17.7 % and 15 % oxygen feed concentration, most detrimental operating conditions for the MEA were identified, allowing the development of an accelerated stress test (AST) to isolate the individual **Stressors**. These tests were implemented on a differential single cell with 12 cm^2 active, including cell temperature and oxygen concentration as main stressors, allowing to determine the effect of these parameters on MEA degradation. Various *in-situ* and *ex-situ* characterization methods were used, to determine the degradation of the MEAs.

Load cycling induces catalyst activity loss, seen by a 34.4 % reduction in ECSA after 400 cycles operation. This can be due to holding time at higher potentials that causes Pt dissolution. Furthermore, carbon corrosion, due to high potentials or start/stop operation present in driving cycle, may cause this big reduction in catalyst activity. High temperature had the strongest effect, among all investigated stressors, on polymer electrolyte membrane (PEM) degradation, yielding a potential degradation rate of 0.93 $mV \cdot h^{-1}$. Reference test was performed with low temperature and 21 % oxygen concentration, presenting the least stressing operating conditions on the MEA. Reduction of oxygen concentration, from 21 % to 15 %, leads to severe increase in mass transport resistance, due to oxygen starvation. Highest increase in mass transport resistance was observed when combining lowered oxygen concentration with elevated cell temperature, being attributed to the detrimental effect of high temperature. Moreover, improving mechanical stability of the CCM by appropriate cell assembly allows to mitigate membrane degradation upon high temperature operation.

Keywords: Polymer electrolyte membrane fuel cell (PEMFC); Durability; Degradation mechanisms; Accelerated stress tests (AST); Membrane electrode assembly (MEA);

Resumo

A durabilidade é um dos maiores problemas das células de combustível com membrana electrolítica polimérica (PEMFC) para aplicações de transporte, uma vez que a MEA se degrada com o tempo, diminuindo o seu desempenho e limitando a sua rápida comercialização. Os mecanismos mais típicos de **degradação** da PEMFC, em particular a MEA, envolvem degradação da membrana devido a tensão mecânica e térmica, degradação da camada catalítica do cátodo (CCL) como resultado da corrosão do carbono, degradação do ionómero, e dissolução e sinterização da platina.

Os **ciclos de carga** simulam as condições de funcionamento que uma pilha de células de combustível estaria sujeita, em utilização num veículo. Além do mais, as condições específicas dentro de cada célula da pilha não são homogéneas, dependendo dos gradientes de concentração de gás, temperatura e humidade, ao longo do flowfield. Nesta tese, foi dada ênfase às condições representativas da área central de um flowfield. A partir de sofisticados testes de ciclo de condução, realizados com 17,7 % e 15 % de concentração de oxigénio, foram identificadas as condições de funcionamento mais prejudiciais para a MEA, permitindo o desenvolvimento de um teste de degradação acelerado (AST), para isolar **Stressors** individuais. Estes Stressors foram implementados numa única célula de comfustível diferencial, com 12 cm^2 de área ativa, incluindo a temperatura e concentração de oxigénio como principais fatores de stress, permitindo determinar o efeito destes parâmetros na degradação da MEA. Foram utilizados diversos método de caracterização *in-situ* e *ex-situ*, para determinar a degradação da MEA.

O **ciclo de carga** induz a perda de atividade do catalisador, observada por uma redução de 34,4 % na ECSA, após 400 ciclos de operação. Uma causa poderá ser o tempo de retenção a potenciais mais elevados, que causam a dissolução da Pt. Além do mais, a corrosão de carbono, devido a potenciais elevados ou operação de arranque/paragem presentes no ciclo de condução, poderá causar esta grande redução na atividade do catalisador. A Temperature elevada – 95 ºC- teve o efeito mais forte, de entre todos os **Stressors** investigados, na degradação da membrana eletrolítica polimérica (PEM), apresentando a maior taxa de degradação de potencial de 0,93 mV h^{-1}. O teste de referência, realizado a baixa temperatura e 21 % de concentração de oxigénio, apresentou as condições operatórias menos prejudiciais para MEA. A redução da concentração de oxigénio leva a um aumento severo da resistência ao transporte de massa. O maior aumento na resistência ao transporte de massa foi observado quando se combinou uma menor concentração de oxigénio com uma temperatura elevada, atribuído ao efeito prejudicial do aumento da temperatura. Além do mais, a melhoria da estabilidade mecânica da CCM, através de uma montagem apropriada da célula, permite mitigar a degradação da membrana, no caso de operação da célula a elevadas temperaturas.

Palavras-chave: Células de combustível com membrana eletrolítica polimérica (PEMFC); Durabilidade; Mecanismos de degradação; Testes de degradação acelerados (AST); MEA

Declaration

I hereby declare, under word of honour, that this work is original and that all non-original contributions is indicated, and due reference is given to the author and source

Raquel Ribeiro

Index

List of Figures

List of Tables

Notation and Glossary

A	Area	cm^2
d	Thickness of membrane	cm
E	Electrode potential	V
F	Faraday constant	96 485 C mol^{-1}
G	Gibbs free energy	J
H	Enthalpy	J
k_{H_2}	Hydrogen permeation coefficient	mol cm^{-1} s^{-1} Pa^{-1}
ℓ	Spacing between the electrodes	cm
L	Pt loading in the electrode	$g_{Pt}\ cm^{-2}_{electrode}$
i	Current density	A cm^{-2}
I	Current	A cm^{-2}
i_0	Exchange current density	A cm^{-2}
i_ℓ	Limiting current density	A cm^{-2}
I_{H_2}	Hydrogen crossover current	A cm^{-2}
J_{H_2}	Hydrogen crossover flux	mol cm^{-2} s^{-1}
n	Number of moles of electrons transferred	mol
P	Pressure	bar
q_{Pt}	Charge density	µC $cm^{-2}_{electrode}$
r_f	Roughness factor	$m^2_{Pt}\ m^{-2}_{MEA}$
$\mathcal{R}$	Gas constant	8.314 J mol^{-1} k^{-1}
R	Resistance	Ohm
T	Temperature	° C
U	Potential	V
X	Length of the Warburg-like region for ICR determination	
Z	Impedance	Ohm

Greek Letters

γ	Stoichiometric flow	
Γ	Charge required to reduce a monolayer of protons	210 µC cm^{-2}_{Pt}
Δ	Variation	
η	Potential losses	V
σ	Conductivity	S cm^{-1}
Ω	Electric resistance unit	

Indexes

°	Standard state conditions
Ω	Ohmic resistance
act	Activation losses
cell	Single fuel cell
conc	Concentration losses
contact	Contact resistance
cross	Crossover current
CT	Charge transfer
electric	Electric resistance
ionic	Ionic Resistance
MT	Mass transfer
Ohmic	Ohmic losses and ohmic resistance
Rev	Reversible cell potential
Sc	Short-circuit current and short-circuit resistance

List of Acronyms

AST	Accelerated Stress Test
BoL	Beginning of Life
BP	Bipolar Plate
CCL	Cathode Catalyst Membrane
CCM	Catalyst Coated Membrane
CE	Counter Electrode
CL	Catalyst Layer
COR	Carbon Oxidation Reaction
CPE	Constant Phase Element
CS	Cold Soak
CV	Cyclic Voltammetry
DOE	(US) Department of Energy
EC	Equivalent Circuit
ECSA	Electrochemical Surface Area — Unit: $m_{Pt}^2\ g_{Pt}^{-1}$
EDX	Energy Dispersive X-Ray Spectroscopy
EIS	Electrochemical Impedance Spectroscopy

EoL	End of Life
EW	Equivalent Weight
FC	Fuel Cell
FCEV	Fuel Cell Electrical Vehicle
FCH-JU	Fuel Cells and Hydrogen Joint Undertaking
GDL	Gas Diffusion Layer
GDE	Gas Diffusion Electrode
GHG	Greenhouse Gas
HFR	High Frequency Resistance
HOR	Hydrogen Oxidation Reaction
HP	High Pressure
HSAC	High Surface Area Carbon
HT	High Temperature
ICEV	Internal Combustion Engine Vehicle
ICR	Ionic Conductivity Resistance
ID-FAST	FCH JU Project on operando AST for PEMFC
LFR	Low Frequency Resistance
LP	Low Pressure
LS	Long Stop
LSAC	Low Surface Area Carbon
LSS	Long Side Chain
LSV	Linear Sweep Voltammetry
LT	Low Temperature
MEA	Membrane Electrode Assembly
ML1	Middle Life 1
ML2	Middle Life 2
MP	Medium Pressure
MPL	Micro Porous Layer
OC	Oxygen Concentration
OCP	Open Circuit Potential
ORR	Oxygen reduction Reaction
PEM	Polymer Electrolyte Membrane
PEMFC	Polymer Electrolyte Membrane Fuel Cell
PFSA	Perfluorosulfonic Acid

PTFE	Polytetrafluoroethylene
RE	Reference Electrode
RH	Relative Humidity
RHE	Reversible Hydrogen Electrode
SEM	Scanning Electron Microscopy
SS	Short Stop
SSC	Short Side Chain
TEM	Transmission Electron Microscopy
TLM	Transmission Line Model
WE	Working Electrode
XPS	X-ray Photoelectron Spectroscopy

1 Introduction

1.1 Background

The reduction of greenhouse gas (GHG) emission, caused by the use of fossil energy carriers, is presently the greatest challenge of modern society. Therefore, it is essential to replace the conventional energy system with a sustainable and clean one, in which renewable and suitable energy carriers, such as hydrogen, will have a crucial role [1]. European Union has set a target for the year 2050 to reduce GHG emissions by 90 % in the transportation sector, comparing with 1990´s levels. Fuel cell and hydrogen technologies hold great promise and may contribute for achieving this goal [2]. Hydrogen fuel cell is an electrochemical device, that generates electricity and heat through a redox reaction, yielding water as the only product. It is expected to attract numerous niche markets due to its superior characteristics and power density [3][4][5]. Among other type of fuel cells like alkaline and solid oxide fuel cells, there are the polymer electrolyte membrane fuel cells (PEMFC), which are characterized by its low operating temperatures, high energy-conversion efficiency, short start-up times, quiet operation, low emission, compactness, and fast load response [6][7][8]. Furthermore, typical hydrogen refuelling time is much shorter compared with the charging time of a battery, being advantageous for end consumers [9].

Great effort is being achieved towards implementation of reliable, highly efficient, and durable PEMFC for automotive applications, as evidenced by the launch of PEMFC based vehicles like Hyundai Nexo, Honda Clarity and Toyota Mirai, in recent years [10][11][12]. Regarding automotive fuel cell system costs, at low manufacturing levels of 1000 units per year, the MEA (membrane electrode assembly) accounts almost for 50 % of all costs, with 28 % contribution from catalyst coated membrane (CCM) and 14 % contribution from gas diffusion layer (GDL), to the overall system cost [13]. Bipolar plates contribute 33 % to the overall system cost, as result of its complex fabrication and high number of required plates for a fuel cell stack [13]. Toyota Mirai PEMFC is projected to cost 233 USD/kW at 1000 stacks/year, which is quite above the target cost for a fuel cell system proposed by DOE (US Department of Energy) of 30 USD/kW, by the year 2025 [14].

Two major barriers for the worldwide deployment of PEMFC are durability and cost [12]. The price of a fuel cell electrical vehicle (FCEV) is still high compared to internal combustion engine vehicle (ICEV), which hinders its larger scale implementation. The high costs are mainly due to difficult market penetration, along with the high platinum loading needed on the cathode to achieve the demanded lifetime and performance [5][11][13]. The high oxygen reduction reaction (ORR) activity and relatively high stability in the acidic environment of the PEMFC makes it hard to find a suitable substitute for Pt catalyst [14]. State of the art FCEV uses around 30 g of Pt, while ICEV only requires 5 g of PGM (platinum group metals) comprising Pt, Pd and Rh [15]. Cost reduction can be achieved by reducing Pt loading through developing highly efficient cathode catalyst layer (CCL) that can

be achieved by supporting Pt particles over higher surface area carbon support [5][16]. The use of non-Pt based electrocatalyst can also be adopted. Nevertheless, it still on an early research phase [15]. The stability of PEMFC remains one of the most crucial technical challenge for the developing of FCEV [9] and especially heavy duty transport applications [17]. Therefore, understanding its degradation phenomena is crucial to improve PEMFC materials to better resist stressing conditions like high temperatures, high cell potentials and low relative humidity [18]. When fabricating a CCM using same materials and coating techniques, durability as well as performance decreases, as electrocatalyst loading is decreased [19], making it hard to meet both cost and durability targets defined by DOE [12] and European Commission [20].

1.2 Framing of the thesis

There are challenges to be solved that affect the PEMFC performance, such as the degradation of fuel cell components under severe conditions, the presence of contaminants, and fuel cell design and assembly. Fuel availability and public acceptance are also big factors determinant for the technology success [1][10][21]. PEMFC must present good performance under thermal cycling (subfreezing and high temperatures). Operation at higher temperatures allows for better heat rejection and simpler fuel cell stack design, as well as improved electrochemical kinetics and simplified water management. However, the cathode catalyst degradation is accelerated at higher temperatures, which lead to drying, and membrane protonic conductivity drops significantly, with water content decrease [10][22].

An automotive fuel cell requires around 300 cells stacked in series, each of around 300 cm^2 of electrochemically active area, to deliver high power required for vehicle propulsion. At nominal power, each cell operates at around 0.6 V and delivers a current of around 450 A (*ca.* 81 kW) [15]. At high current densities, such as 1.5 A cm^{-2}, water production increases, which can hinder mass transport due to flooding of porous media of CL, and lead to the fast aging of the fuel cell and power output decrease [23]. Other challenges are the inevitable start-up and shut-down events in PEMFC, especially for automobile applications, that causes cathode fast degradation of the MEA [11][24]. Durability is a major challenge for PEMFC to be accepted as a viable product, which is highlighted in this thesis. The 2030 durability target of a PEMFC is 7000 h (*ca.* 600 000 km) and 28 000 h for car and buses, respectively [20]. To study the performance degradation, the dependence of PEMFC on different operating conditions must be analysed. Degradation rate of fuel cell components can be reduced by understanding and investigating failure mechanisms. For that, Accelerated Stress Test (AST) may be performed in attempt to reduce duration and high costs of time consuming real lifetime tests [10]. The focus of this thesis is to investigate the effect of different stressors on the performance and durability of a single cell. It was adopted the drive cycle from the EU project ID-FAST, and numerous *ex-situ* and *in-situ* analysis were performed to scrutinize the critical stressors on the MEA in PEMFC operation.

1.3 Contributions to the work

The work conducted during this thesis is related to the Fuel Cells and Hydrogen Joint Undertaking (FCH-JU) ID-FAST project. The main goal of ID-FAST is to develop Accelerated Stress Tests (AST) for PEMFC to be able to predict performance degradation applied to real world operation, as means of supporting and promoting the deployment of fuel cell vehicles [25].

Previous experiments had been done in DLR regarding the implementation of ID-FAST driving cycle test on a single zero-gradient cell, simulating the middle condition of a fuel cell stack. These experiments were conducted with 17.7 % and 15 % of oxygen feed concentration [26]. My contributions to this work started with identification of the main stressors from the driving cycle, evaluating the potential degradation on a single cell, at specific operating conditions. Once the main stressors were identified, a protocol was developed to study the degradation effect of these stressors on a single PEMFC, which involved performing *in-situ* and *ex-situ* characterization. *In-situ* characterization was performed in all experiments. However, *ex-situ* characterization involving scanning electron microscopy (SEM) and X-ray photoelectron spectroscopy (XPS) analysis were performed at DLR and at the University of Esslingen by someone else. After having a protocol defined, four stressor tests on a single cell were conducted, which allowed to study MEA components degradation, under specific operating conditions. A driving cycle test, with 15 % of oxygen feed concentration, was also evaluated for a different catalyst coated membrane (CCM) than previous tests. This way, it would be possible to evaluate different CCM performances under the same operating conditions and take conclusions regarding the effect of critical stressors in different MEAs.

1.4 Thesis Outline

This thesis follows the conventional organisation of a master thesis, being organized in six chapters. It begins with the Introduction, followed by the Context and State of the Art, Materials and Methods, Results and Discussion, Conclusions, and finally, the Assessment of the work done.

1.5 Presentation of the institution

The work presented in this thesis was carried out at the German Aerospace Center (DLR) in the Institute of Engineering Thermodynamics in Stuttgart. DLR is Germany´s research centre for aeronautics and space and it conducts research in diverse sectors such as space, aeronautics, energy, transport, and security. DLR is active in all areas of hydrogen research, from production to storage and use. It is developing fuel cells that can be integrated in cars, aircrafts, ships, and buses [27].

2 Fundamentals and state of the art

2.1 PEMFC principle and components

Fuel cell was first invented by Sir William Robert Grove in 1839 and it has attracted much attention since its development by General Electric in the 1960s [13][28]. PEMFC is an energy conversion device that produces electricity and heat (exothermic process), consisting of two electrodes separated by an electrolyte. It involves hydrogen oxidation reaction (HOR) on the anode, yielding electrons and protons (equation (1)), and oxygen reduction reaction (ORR) on the cathode, generating water (equation (2)) [1][5][13]. HOR involves its adsorption into Pt catalyst surface, followed by H_2 molecule dissociation and electrochemical reaction to originate two hydrogen ions [29]. Fuel and the oxidant are fed to the anode and cathode, respectively, being conducted by the gas diffusion layers (GDL) to reach the active catalyst sites. The ionic charges are transported through the electrically insulating polymer electrolyte membrane to the cathode side, while electrons travel through an external circuit. The overall electrochemical reaction is represented by equation (3) [1][5][4].

Anodic Reaction (HOR):): $\mathrm{H_2} \rightleftharpoons 2\mathrm{H^+} + 2\mathrm{e^-},\ E^0 = 0\ \mathrm{V}$ (1)

Cathodic reaction (ORR): $\frac{1}{2}\ \mathrm{O_2} + 2\mathrm{H^+} + 2\mathrm{e^-} \rightleftharpoons \mathrm{H_2O},\ E^0 = 1.23\ \mathrm{V}$ (2)

Overall reaction: $\mathrm{H_2} + \frac{1}{2}\mathrm{O_2} \rightleftharpoons \mathrm{H_2O},\ \Delta E^0 = 1.23\ \mathrm{V}$ (3)

A PEMFC has four main components: the polymer electrolyte membrane, the electrocatalyst layer, the GDL and the flow field plates. The membrane electrode assembly (MEA) consists of the assembly of the electrolyte membrane and the two electrodes [1], also named catalyst layers. Atop the CLs, GDL are placed, being in contact with the bipolar plate (BP), which usually contains the flow field [5]. It is usually referred as 5-layer MEA as it is composed by 5 different layers (one membrane, 2 CLs and 2 GDL).

There are two ways for fabricating a MEA, the catalyst layer can be either directly deposited on the membrane, forming a CCM, or it can be deposited on the GDL originating a gas diffusion electrode (GDE). The porous CL is composed of proton conductive ionomer and the catalyst, which is usually the Pt supported by electrically conductive carbon particles [4][8][13]. In Figure 2.1 it is shown a representation of the main constituents of a PEMFC as well as its functioning. The ionomer, Pt catalyst, and carbon support constitute the triple-phase boundary, which is addressed in subsection 2.1.4.

In the following subsections, the individual PEMFC components will be addressed in more detail.

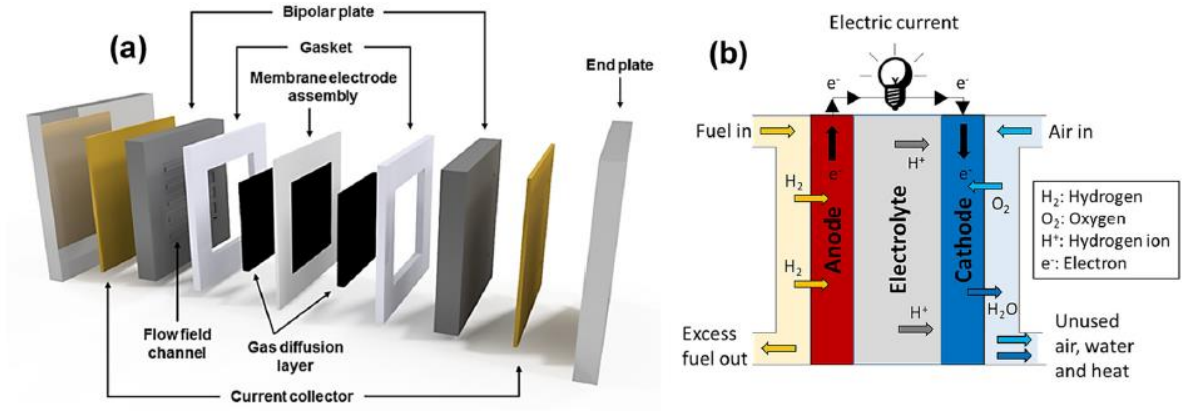

***Figure 2.1** – Schematics of main components of a PEMFC (a) and functioning of a hydrogen/fuel cell (b), extracted from* [30].

2.1.1 Bipolar plates (BPs) and sealing gasket

BP supports the structure of the fuel cell, and its main function is the electrical contact between the cells as well as to accommodate the flow-field and keep the contact pressure into the MEAs. It allows homogeneous gas distribution over the active area of the MEA, through a flow pattern. It acts as a current collector and therefore, it must have high electrical conductivity [4][5][13]. BP should also display high corrosion and chemical resistances, low gas permeability, low cost, and high thermal conductivity, which allows fast dissipation of the heat by the electrochemical reactions from the CL to the coolant (since a coolant, typically a fluid is normally used, that flows within the BP) [10][31]. Initially, graphite BP was popular as result of its high electrical conductivity and high corrosion resistance. However, its brittleness and gas permeability gave rise to a need to seek other materials, like carbon composites and metals with proper coating [12]. Regarding automotive applications, due to its better large scale processability, BPs are usually made of stainless steel, with a coating to mitigate corrosion and reduce the contact ohmic resistance [13].

Gaskets are placed between the bipolar plates to prevent gas and coolant crossover and leakage. Appropriate rubber seals and PTFE coated fiberglass gaskets are usually used to seal the bipolar plates towards atmosphere [5][13][10].

2.1.2 Gas diffusion layer (GDL)

GDL typically consists of a thermally and electrically conductive carbon-based porous layer standing between the flow field plate and the CL [1][13][10]. The GDL has a thickness of around 100 to 300 µm. Low contact resistance of GDL towards CL and flow field is achieved with high compression of the GDL, which can be controlled by the amount of torque exerted on the bolts of the fuel cell. The GDL is based on carbon materials impregnated by polytetrafluoroethylene (PTFE) to tailor its hydrophobicity. PTFE is important for proper transport of product water from the CL to the BP and to balance the humidity of the ionomer in the membrane and in the CL (water management) [1][4].

It is composed of (i) a macro-porous carbon fiber paper or carbon cloth substrate, the so called backing of the GDL which is in contact with the BP, and a micro-porous layer (MPL) which is in

contact with the CL. Carbon paper has smoother surface and high tortuous pore structure, that allows to retain water in the MEA, being commonly used in commercial GDL [1][4][6]. The GDL facilitates water management by ensuring humidification of the membrane, but at the same time prevents water flooding at CL by conducting water flow out of the MEA [1][4].

GDLs must have an optimum pore dimension, for effective water management, as higher pores enhance species gas diffusion, but they increase ohmic losses. While the MPL reduces liquid flooding and contact resistances and enhances electrochemical performance due to introduction of micro-porosity in GDL, the backing of the GDL optimizes reactant distribution from flow field channels to catalyst layer, due to its macro-porosity properties [6]. If the MPL is too thin, then the contact between the CL and the GDL increases. PTFE, present in both GDL and MPL, allows to obtain the desired water-repellent behaviour, with a polymer loading on the layer surface in a range between 5 % and 30 %, by weight [1][4][6].

2.1.3 Membrane

The electrolyte or ionomer is typically composed of PTFE backbone, which is hydrophobic, and perfluoroalkyl ether side chains terminated with sulfonic acid group (PFSA), that is hydrophilic fragment. The polymer electrolyte membrane, with a thickness on the order of 20 μm (automotive applications), conducts solvated protons, isolates the anodic from the cathodic reaction chamber, mitigates gas crossover and prevents electrons from crossing the membrane, originating electrical short within the cell [5][13][31]. The membrane must have thermal and chemical stability, up to at least 100 ºC, low reactant gas permeability and high protonic conductivity. Lower protonic resistance is usually associated with higher water uptake, that represents membrane ability to absorb water [7]. Membrane hydration is crucial for a good performance of a PEMFC, and must have an optimal value that allows good proton conduction without risk of flooding the CL and GDl [12]. There are three main proton transport mechanisms through the membrane, which are surface, vehicle and Grotthuss mechanisms. The surface transport considers the proton to jump from sulfonic to sulfonic group; in the vehicle mechanism, protons combined with water molecules (hydrated ions) are transported through electro-osmosis. On the other hand, Grotthuss mechanism considers the jump of protons from one water to another water molecule [29].

In early 1970s, perfluorosulfonic acid (PFSA) membranes were developed by Dupont, with high stability and protonic conductivity. Ever since, several of PFSA membranes have been launched in the markets due to its low fabrication cost, such as Nafion® (Dupont™), Gore-Select® (Gore™), Aciplex® (Asahi Chemical™) and Flemion® (Asahi Glass™) [7][13]. FUMATECH BWT GmbH also manufactures long chain and short chain PFSA membranes [32].

PFSA membranes, depending on length of side chain, can be divided in long side chain (LSC) and short side chain (SSC) membrane, represented by Nafion membrane (produced by Chemours) and Aquivion membrane (produced by Solvay Specialty Polymers), respectively [7][13]. The chemical

structure of these membranes can be seen in the paper from Pan *et al.* [7]. The equivalent weight (EW) is the mass of polymer per mole of sulfonic acid and it increases with the increase of the side chain length [7][13]. SSC with low EW present better protonic conductivity, leading to higher current density of the cell [5] and better thermal stability, as result of higher polymer glass transition temperature, (140-160 ºC) when comparing with LSC membrane. However, they degrade more under humidity cycling tests, due to higher O_2 transport resistance through the liquid film, as result of stronger water absorption of the ionomer. Regarding LSC, they present thermal and chemical stability, high mechanical strength, fast ORR, and low conduction resistance [7][13][33].

Membrane thickness is an important parameter since membranes with excessive thickness causes high ohmic resistance [7]. Thinner membranes allow achieving higher power densities due to improved water management and proton conductivity. On the other hand, if the membranes are too thin, they suffer from lowered mechanical stability; gas permeability and electron conductivity may increase, causing mixed potentials on cathode side and parasitic hydrogen consumption with possible formation of pinholes [34][35]. The hydrogen permeation coefficient can be expressed as a function of the crossover current density, i_{H_2}, the Faraday constant, F, the number of electrons per molecule, n, partial pressure of hydrogen, p_{H_2}, and thickness of membrane, d, as can be seen in equation (4) [34].

$$k_{\mathrm{H}_2} = \frac{i_{\mathrm{H}_2}}{n \cdot F} \frac{d}{p_{\mathrm{H}_2}} \tag{4}$$

2.1.4 Catalyst Layer (CL)

Conventional CL is composed of platinum particles, carbon powder support and ionomer. Pt catalyses the electrochemical reactions, by lowering the energy barrier for HOR and ORR [8][31]. CL´s main function involves providing a path for proton transport, a passage for electron conduction and a pore network for gaseous reactant supply and water removal [12]. Pt metal is the state-of-the-art catalyst for PEMFC, on both cathode and anode side. To maximize the effective area of platinum, the 2-3 nm platinum particles are spread onto the surface of larger carbon particles (50-70 nm), which enables high dispersion of catalyst particles, and avoids agglomeration. The carbon support is necessary for stabilisation, and it creates a porous structure in the CL for gas transport, ensuring electrons are conducted to and from the reaction sites [13][12][14][31][36]. The most used carbon supports are "Vulcan XC-72" and "Ketjenblack", with a surface area of 228 $m^2 \cdot g^{-1}$ and 890 $m^2 \cdot g^{-1}$. Pt alloys can also be used as cathode catalyst for ORR in PEMFC, being PtNi and PtCo the more frequently used [13][12].

According to Harzor (2018) low surface area carbon (LSAC) supported catalyst has good performance at high current densities, as oxygen does not need to diffuse into carbon pores to reach active sites. However, high surface area carbon (HSAC) is associated with higher catalyst activity as there can be more Pt particles inside carbon primary particles, that are less prone to poisoning and can still contribute to ORR [13].

A triple-phase boundary, which is also known as reactive interphase, is a crucial requirement for a good electrode, in which the ionic conductor, the catalyst particle and the gas supply are all in direct contact. It facilitates the transport of reactant gas (through porosity to catalyst layer), electrons (via carbon support) and protons (from catalyst through ionomer network). It is achieved by impregnating the catalyst with a binder, the ionomer, before pressing the electrode into the membrane. An imbalance in the ionomer loading may cause ohmic or transport losses, as a thick ionomer can cause diffusion problems and a thin ionomer may decrease proton conductivity [5] [29][37].

Figure 2.2 a) demonstrates a representation of the triple-phase boundary, observed by transmission electron microscopy (TEM) analysis. A study performed by More *et al.* [37] has shown that there is a non-homogeneous distribution of constituents within CL, as can be observed in Figure 2.2 b). In fact, by TEM analysis, it can be observed ionomer regions of varying thickness clustered around and between the carbon support agglomerates. Many of the Pt particles were no longer attached to carbon surface, but isolated instead within ionomer pockets or strands, as can be seen in Figure 2.2 c) and d). These isolated Pt particles were no longer catalytically active since they were not part of the 3-phase interface [37].

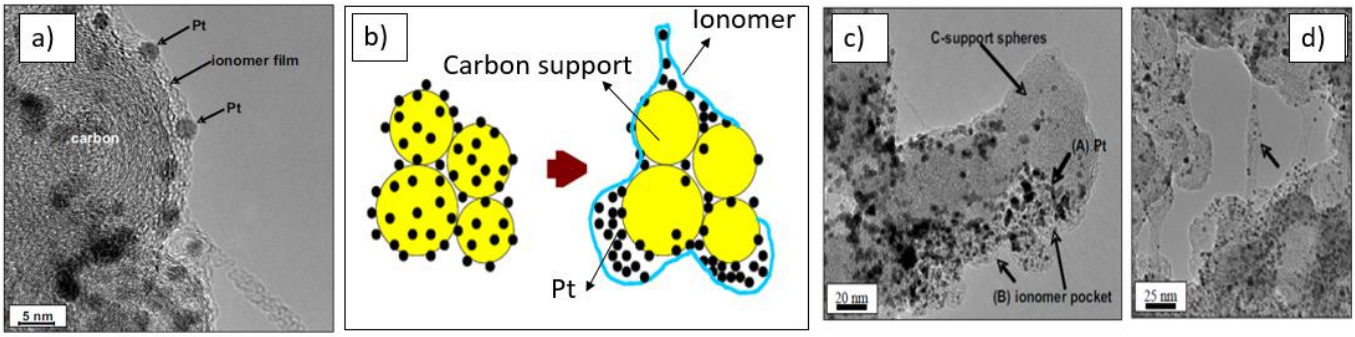

***Figure 2.2** – TEM image representing model structure of a) triple-phase boundary. Scheme representing b) non-homogeneous distribution of Pt particles. TEM images representing c) ionomer pockets and d) ionomer strands, adapted from* [37].

2.2 Thermodynamics and overpotential

The Gibbs free energy is the theoretical maximum energy the electrochemical system can provide [31]. The variation of Gibbs free energy, ΔG^0, for the reaction at standard state conditions (25 ºC and 1 atm) is -237.2 kJ mol^{-1}, assuming water produced in liquid state. *F* and *n* are the Faraday constant, and the number of electrons involved in the reaction, respectively (*F*= 96 485 C mol^{-1} and *n* = 2). The reversible open circuit potential (OCP), E^0, of the cell is 1.23 V, and it is calculated trough equation (5).

$$E^0 = -\frac{\Delta G^0}{nF} = 1.23\ \text{V} \qquad (5)$$

Most fuel cells do not run at standard conditions, being subjected to changes in temperature and pressure. Therefore, the reversible cell potential is given by Nernst equation, expressed by equation (6), in which T is the cell temperature, $\mathcal{R}$ is the gas constant (8.314 J mol^{-1} K^{-1}) and P_{H_2O}, P_{H_2}, and P_{O_2} are the partial pressures of water, hydrogen and oxygen, respectively.

$$E = E^0 - \frac{\mathcal{R}T}{nF}\ln\left[\frac{P_{H_2O}}{P_{H_2}P_{O_2}^{0.5}}\right] \quad (6)$$

The potential achieved by cells is usually lower than the theoretical value, due to irreversible losses that occur during PEMFC functioning. In fact, the energy loss in each component will appear in the form of activation, ohmic or mass transport overpotential. The performance of a fuel cell can be presented through a polarisation curve, which consists of a plot of potential against current density [1]. It measures the fuel cell performance by showing how much the potential drops with the increase on current density, as can be seen in Figure 2.3 [31].

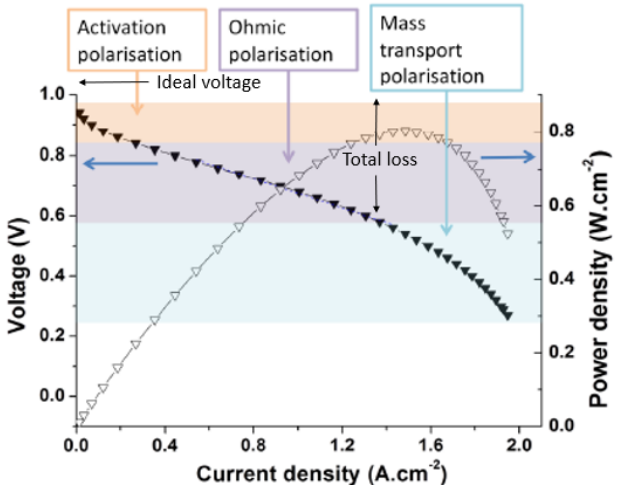

***Figure 2.3** - PEMFC polarisation curve, adapted from* [1].

2.2.1 Activation Losses

The activation losses, η_{act}, are due to the activation energy necessary for the chemical reaction to occur at the electrode surface, and it occurs at low current densities [1][38]. Pt catalyses both the HOR and ORR, but since catalytic activity of Pt on HOR is several orders of magnitude higher than ORR, the anode overpotential is negligible, which makes activation potential losses from cathode to be dominant [31][39]. Activation losses can be approximated by Tafel equation, given by equation (7), in which i_0 is the exchange current density, and i is the current density [38]. The exchange current density can be increased by increasing the reactant concentration and the temperature, by enhancing the number of probable reaction sites and decreasing the activation barrier [5].

$$\eta_{act} = \frac{\mathcal{R}T}{nF}\ln\left[\frac{i}{i_0}\right] \quad (7)$$

A cause for kinetic overpotential can be anode poisoning, in which the surface of the anodic catalyst is covered with contaminants from the fuel, like CO or NH_3, decreasing active catalyst sites and

decreasing hydrogen reduction kinetics. The surface of cathodic catalyst can also be covered with platinum oxides that decrease electrocatalytic activity of ORR. This oxide formation is known to be present at high cathode potential and during low current densities or OCP. Other contaminants present in the air, such as SOx or NOx, can also adsorb onto the catalytic surfaces, reducing the active area [3][8].

2.2.2 Ohmic Losses

Ohmic loss, η_{ohmic}, given by equation (8), results from the flow of ions trough the electrolyte and the flow of electrons throughout the GDL, CL and bipolar plate [1][31]. The ohmic resistance is given by equation (9), where R_{ionic}, R_{electric} and R_{contact} are the proton resistance, electronic resistance, and contact resistance, respectively. Electrical resistance can be caused from insufficient compression of the MEA with the bipolar plates [5]. As the GDL, catalyst layer and bipolar plates are made of materials with high electrical conductivity, they present low electronic resistance. This way, the ohmic resistance is dominated by ionic resistance [31], given by equation (10), in which σ is the conductivity, A is the active area of the membrane, and ℓ the spacing between electrodes [5][7].

$$\eta_{\text{ohmic}} = i \cdot R_{\text{ohmic}} \cdot A \tag{8}$$

$$R_{\text{ohmic}} = R_{\text{ionic}} + R_{\text{electric}} + R_{\text{contact}} \tag{9}$$

$$R_{\text{ionic}} = \frac{\ell}{\sigma A} \tag{10}$$

2.2.3 Concentration Losses

Concentration losses, η_{con}, also referred as mass transport losses occur mainly at high current densities, when sufficient reactant is not transported to the electrodes, hindering the reaction [1]. Indeed, while travelling throughout the cell, there is a point in which the fuel will be depleted, and the current density can no longer increase [31]. At this point, when the current density reaches its maximum value and the reactant concentration in CL falls to zero, the limiting current density, i_ℓ has been reached [5][38]. Increased concentration losses can be due to water accumulation in electrodes that partially block the mass-transport of reactants, decreasing cell performance [3][39]. Concentration polarization can be written as follows [5]:

$$\eta_{\text{con}} = -\frac{\mathcal{R}T}{nF}\ln\left[1 - \frac{i}{i_\ell}\right] \tag{11}$$

Oxygen transport resistance is inversely proportional to the electrode roughness factor,r_f, which is defined as Pt surface area per MEA geometric area ($\text{m}_{\text{Pt}}^2\text{m}_{\text{MEA}}^{-2}$), and results of the product between electrochemical active surface area (ECSA) ($\text{m}^2\text{g}_{\text{Pt}}^{-1}$) and MEA Pt loading ($\text{g}_{\text{Pt}}\text{m}_{\text{MEA}}^{-2}$) [29][39][40]. Concentration losses are due to oxygen pathway from flow field to the reaction site, in which there is likely to be a gas/ionomer film interface, an ionomer film resistance and an ionomer/Pt interface [41]. The real cell potential, having in account the overpotentials, is provided by equation (12):

$$U_{\text{cell}} = E_{\text{rev}}^{\circ} - \eta_{\text{act}} - \eta_{\text{ohmic}} - \eta_{\text{conc}} \tag{12}$$

2.3 Degradation Mechanisms

Reduction in cell performance, caused by chemical and physical degradation phenomena, limits PEMFC durability and hence hinders its commercialization. Main failure modes of PEMFC applied in vehicles are related to dry operation conditions, GDL hydrophobicity loss leading to poor water management, reactant starvation, presence of contaminants in fuel stream like CO, S and NH_3, and dynamic operating conditions like load changes cycles and start-up/shutdown cycles [3][9][12]. Activity loss of the electrocatalyst is detrimental for the fuel cell and can be caused by degradation of the polymer electrolyte membrane as well as the ionomer, due to formation of hydrogen peroxide, and carbon corrosion [28]. Table 2.1 presents a scheme of the most important faulty conditions for PEMFC degradation, along with its main effects.

Table 2.1- PEMFC degradation main faulty conditions, adapted from [42] *and* [43].

PEMFC Faulty conditions	Factor	Degradation Mechanism	Irreversible degradation	Effects
Flooding and starvation	-water condensation and accumulation inside porous structure of electrode; -O_2 pathway to catalyst site is hindered; -Dynamic and start up operating conditions -Load cycling	-Hydrogen evolution reaction on cathode side (oxygen depletion)	-Thermal Ostwald ripening	-Loss of ECSA
		-Platinum dissolution	-Electrochemical Ostwald ripening	-Loss of ECSA
		-Carbon corrosion	-Catalyst thinning -Catalyst particle detachment	-Electronic resistance increase -Membrane mechanical strength decrease -Loss of ECSA
Dehydration	-Stack Temperature and relative humidity	-Radicals and peroxide attack on ionomer	-Membrane thinning -Pinhole formation	-Membrane mechanical strength decrease -Gas crossover increase
Poisoning	-CO present in H_2 streams produced via steam reforming; -Air pollutants; -Cations that can exchange with protons from ionomer SA groups	-Impurities adsorption on the catalytic sites	-Blockage of catalytic sites	-Loss of ECSA
		-Impurities accumulation in ionomer membrane	-Ion exchange with protons of sulphonic groups in the ionomer	-Lowering of protonic conductivity

2.3.1 Membrane

Mechanical degradation of membrane results from cyclic compression, material expansion that can occur during wet/dry cycling and leading to crack and pinhole formation [12][39]. Pinholes cause crossover of reactant gases into respective reverse electrodes. As result, the direct combustion of oxidant and reductant, which is highly exothermic, occurs on catalyst surface, generating local hot points which enhances the pinhole formation effect. Local areas corresponding to the interface between the sealing edges of PEMFC are susceptible to mechanical degradation, as they are under excessive or non-uniform mechanical stress [10]. Membrane suffers **thermal degradation** when subject to high temperatures as first glass transition temperature of PFSA polymer occurs at around

110-130 ºC. However, PTFE backbone gives Nafion membranes relative stability until beyond 150 ºC due to shielding effect of electronegative fluorine atoms and C-F bond strength [10].

Chemical degradation of membrane may result from peroxide radicals that can degrade the membrane, being enhanced under high potential (OCP), low humidity, and high temperature conditions. Impurities in air stream, humidifier reservoirs and corrosion of stack components are possible sources of catalyst poisoning. Also, membrane sulfonic sites have higher affinity to other cations than H^+, reducing proton conductivity [12][39]. Contamination by trace metal ions, the Fenton reagents, from corrosion of the metal bipolar plates (such as Fe^{2+} or Cu^{2+}), can accelerate membrane thinning by catalysing radicals' formation reactions (equation (13)) [10][39].

$$H_2O_2 + Fe^{2+} \rightarrow HO^{\bullet} + OH^- + Fe^{3+} \quad (13)$$

Chemical degradation occurs mainly by means of unzipping reaction. During membrane polymerization, small quantities of carboxylate end groups are inevitably formed, that are susceptible to $HO^{\bullet}$ radical attack. HF and CO_2 are released, and new carboxylate groups are formed at the chain ends, as can be seen in Equation (14), (15), and (16) [13][10]. $HO^{\bullet}$ radicals can also attack the $R_f{-}CF_2{-}SO_3H-$ group, which will decompose to $R_f{-}CF_2^{\bullet}$, in a similar manner [13]. Membrane ohmic losses increase, since the ionic conductivity of the membrane is decreased by side chain cutting of polymer. The chemical degradation by peroxide radical formation can lead to fuel cell failure and mixed potentials, as result of membrane thinning and pinhole formation, causing hydrogen crossover current to increase. While water can seal membrane defects and eliminate crossover during fuel cell operation, drying condition of membrane can cause membrane shrinking, increasing gas crossover by enlarging microcracks [3][10].

$$R_f{-}CF_2COOH + HO^{\bullet} \rightarrow R_f{-}CF_2^{\bullet} + CO_2 + H_2O \quad (14)$$

$$R_f{-}CF_2^{\bullet} + HO^{\bullet} \rightarrow R_f{-}CF_2OH \rightarrow R_f - COF + HF \quad (15)$$

$$R_f - COF + H_2O \rightarrow R_f - COOH + HF \quad (16)$$

The rate of fluoride loss is considered an excellent measurement of PFSA membrane degradation.

2.3.2 Catalyst layer (CL)

Loss of electrochemical active surface area (ECSA), as result of platinum catalyst and carbon support corrosion, are common degradation phenomena that lead to activation losses and increased ohmic resistance [3][21][12]. Degradation of Pt catalyst is related to high temperature fuel cell operation [36]. However, under low RH, Pt may suffer less degradation due to lower mobility of dissolved Pt ions [39].

- **Platinum dissolution and sintering**

Pt dissolution occurs mainly under potential cycling or at relatively high potentials (above 900 mV). Pt dissolution into the electrolyte can be considered the primary catalyst degradation mechanism, while Pt sintering, Ostwald ripening and Pt particle detachment are considered secondary mechanisms [21][39][44]. **Sintering**, also referred as agglomeration or coalescence, is caused by

particle migration, and occurs when several nanoparticles in contact with each other merge to form larger particles with decreased surface energy [36][39]. In **Ostwald ripening** mechanism, Pt surface atoms from nanoparticles can dissolve into the electrolyte as ionic species, which can lead to particle growth by redeposition on the surface of larger particles. Ostwald ripening is more pronounced for small particles. Therefore, ECSA reduction is more critical for low loaded cathodes, comparing with high loaded cathodes, as smaller particles are more likely to endure Ostwald ripening. **Pt particle detachment** from carbon support also causes ECSA loss, as detached particles will no longer be part of the triple-phase boundary [21][39][40].

Dissolution of Pt from cathode is observed when residual oxygen concentrations inside cathode are kept high under low current density conditions. Dissolution of anodic Pt can be observed under constant-current operation when hydrogen feed is low enough to induce hydrogen shortage on Pt surface. Pt at both electrodes is dissolved electrochemically (equation (17)), when exposed to high potentials [28][39]. Then, the Pt ions that are dissolved in water will migrate to membrane phase, undergoing repeated reduction/deposition by crossover hydrogen (equation (18)) and repeated oxidation/dissolution by crossover oxygen (equation (19)). Redissolution of Pt can occur in the presence of water at cathode (equation (20)). Crossover oxygen pushes Pt particles in the membrane towards the anode side, via oxidation mechanisms, while crossover hydrogen reduces migrated Pt ions, stopping the movement of dissolved Pt towards the anode. This way, it will be deposited a Pt band, usually between 1 to 10 μm from cathode-membrane interface, whose location will be at the point where oxygen concentration is depleted [28]. The formation of platinum precipitations is correlated with increased ohmic resistance and cell performance loss. In fact, dissolved Pt ions tend to migrate into the membrane close to sulfonic acid groups, causing Pt reprecipitation in the ion channels, blocking them [21].

$$\mathrm{Pt} \rightarrow \mathrm{Pt}^{2+} + 2\mathrm{e}^{-} \quad (17)$$

$$\mathrm{Pt}^{2+} + \mathrm{H}_2 \rightarrow \mathrm{Pt} + 2\mathrm{H}^{+} \quad (18)$$

$$\mathrm{Pt} + \frac{1}{2}\mathrm{O}_2 \rightarrow \mathrm{PtO} \quad (19)$$

$$\mathrm{PtO} + 2\mathrm{H}^{+} \rightarrow \mathrm{Pt}^{2+} + \mathrm{H}_2\mathrm{O} \quad (20)$$

Pt dissolution in the anode is not so common but can occur at high current densities where there may be shortage of both hydrogen and oxygen. In fact, fuel shortage at the anode electrode, while operating the PEMFC at constant current, means that an additional fuel supply is necessary to keep the current production at a constant level, that can lead to Pt being oxidized electrochemically (equation (21)) [28].

$$\mathrm{Pt} + \mathrm{H}_2\mathrm{O} \rightarrow \mathrm{PtO} + 2\mathrm{H}^{+} + 2\mathrm{e}^{-} \quad 0.98\ \mathrm{V\ vs.\ SHE} \quad (21)$$

An alternative process can be electrochemical decomposition of water to generate oxygen, H^+ and current (equation (22)). The produced O_2 causes oxidation of Pt to PtO, that undergoes anodic Pt dissolution and migration to membrane phase [28].

$$2\mathrm{H}_2\mathrm{O} \rightarrow \mathrm{O}_2 + 4\mathrm{H}^{+} + 4\mathrm{e}^{-} \quad (22)$$

- **Carbon Corrosion (CC)**

CC is boosted at high temperatures, and it originates loss of electrical contact between the nanoparticles and the support, loss of porosity, and decrease of catalyst activity. It affects water management and mass transport losses in the cathode, due to decrease in hydrophobicity for oxidized carbon surfaces and can lead to Pt particle detachment [16][35][36]. CC of catalyst support, it is dominated by two main mechanisms, which are cell reversal due to fuel starvation, and high potentials generated at the cathode side, as result of transitioning between start-up and shut-down [9]. Fuel starvation occurs when reactant supply at the inlet is sufficient to support the load current, but its concentration in some areas may be close to zero. It can occur due to ice formation leading to gas flow blockage [10][45].

Carbon oxidation reaction (COR) potential is 0.2 V vs RHE, making it unstable under fuel cell operating conditions. However, the sluggish kinetics of COR enables its use as catalyst support in cathode catalyst, as high corrosion rates only appear at potentials above 0.9 V vs RHE. During start-up air can be present in both cathode and anode, after a long shut-down, as result of imperfect sealing of the cell, which originates a hydrogen/air front that crosses the anode. The hydrogen/air front passing through the anode can create high potentials on the cathode (≈1.5 V), due to ORR occurring in the air-filled part of anode compartment, shifting the adjacent cathode electrode potential, leading to carbon structure oxidation and cathode catalyst layer thinning [11][14][21]. The temporary coexistence of hydrogen and oxygen at the negative electrode divides the cell in two sections. Indeed, during the H_2/air front passage, the active part of the cell acts as fuel cell, with H_2 and air in the anode and cathode, respectively; the reverse current flows in the passive part, that was not yet supplied with hydrogen and presents air on both sides, according to Figure 2.4 [24][40][46].

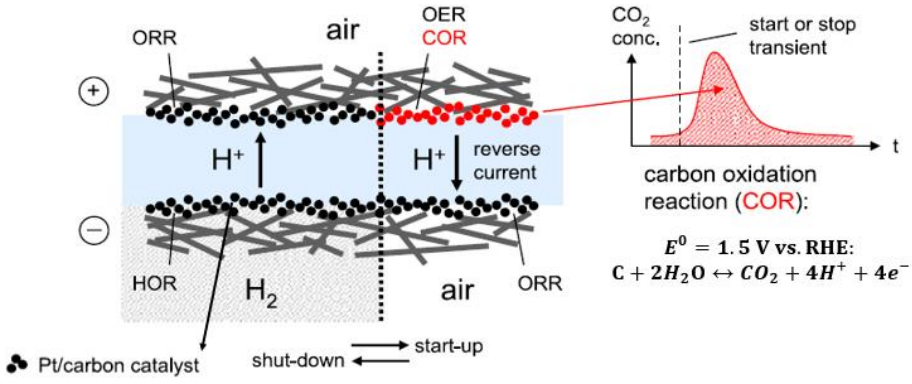

***Figure 2.4** - PEMFC reversal during start-up/shut-down, adapted from* [46].

The carbon oxidation reaction, upon high cathode potential formation, can increase the oxygen transport resistance, particularly at high current densities. In fact, the loss of void volume within CCL is crucial for oxygen transport [9][11]. For both start-up and shut down, as well as fuel starvation, water and carbon oxidation occur, as follows [10]:

$$2H_2O \leftrightarrow O_2 + 4H^+ + 4e^- \quad E^0 = 1.229\ \text{V vs. RHE} \qquad (23)$$

$$C + 2H_2O \leftrightarrow CO_2 + 4H^+ + 4e^- \quad E^0 = 0.207\ \text{V vs. RHE} \qquad (24)$$

When the fuel cell is provided with enough water, carbon corrosion is avoided since water oxidation takes place instead. However, if cell is subjected to high current densities, or if the water in electrode is depleted, then it cannot be avoided [10].

2.3.3 Gas diffusion layer (GDL)

Degradation of GDL is related to loss of hydrophobicity, leading to wetting behaviour changes, mainly in MPL, after long operation time and with increasing operating temperature. Changes in MPL are observed due to carbon corrosion, according to equation (24). Chen *et al*. studied that at high potentials, significant loss in carbon originated thinning of GDL fibers, causing ohmic, charge transfer and mass transfer resistance increase [1][10]. Furthermore, as fuel cell operates, PTFE of GDLs is susceptible to chemical attack. The loss of PTFE and carbon leads to a decrease of GDL hydrophobicity and conductivity, affecting mass transport and water management ability [3][10]. High cell potentials, HT and low RH accelerate GDL degradation, as well as dynamic loading and potential cycling. Mechanical degradation in GDL is mainly due to compression applied to PEMFC during assembling, or erosion by the reactant and water flows. HP results on irreversible variations in GDL thickness, due to breakage and displacement of fibers and deterioration of the hydrophobic coating [1].

2.4 Accelerated Stress Tests

All the degradation phenomena previously shown have a negative influence on the power density of the fuel cell. To support the market introduction of fuel cells, numerous projects have been created at European level [3]. PEMFC degradation is expensive to study experimentally, as it occurs over an exceptionally long period of time. Therefore, accelerated stress tests (AST) were implemented to reduce experimental time, and they allow to have a faster and more real evaluation of the fuel cell material´s durability and performance, without carrying out tests for thousands of hours. Durability is associated with the chemical and mechanical stability of the MEA and it is commonly measured in terms of potential loss per hour, under a fixed current [12][6]. These tests have been proposed and implemented by several research institutes around the globe, fuel cell developers, and companies, such as Ballard Power systems, DuPont, Gore and General Motors. AST should activate the target failure mode of the specific component in study, as well as minimizing the effects from other components [10]. The main target is to investigate as well as understand the main degradation phenomena for PEMFC and prevent it from happening in future. ID-FAST project deals with the development of AST protocols for PEMFC in automotive applications [47].

3 Material and Methods

3.1 MEA specifications and hardware used

The MEAs used during this research were tested in an in-house built test bench, which allows the control of pressure, temperature, flow rate of gases and humidity of the reactants. For the data acquisition control, it was used the SIMATIC WinCC software. The testbench, as well as the potentiostat used for cell characterization can be seen in Figure A.1.1 of Appendix A.1. Two different kinds of tests, driving cycle and stressor tests, were performed on a zero-gradient single cell with parallel channels. **Driving cycle test** had the aim to simulate the middle part cell condition of a fuel cell stack (see Table 3.2), and it was conducted by performing load cycling on a single cell. **Stressor tests,** on the other hand, consisted of specific conditions of the driving cycle particularly stressing for the MEA, and they were performed at stationary conditions.

Both tests were executed at qCf Liquid Cooling high amp single cell hardware from BalticFuelCells GmbH, with 12 cm^2 active area, designed for operating at high current densities, up to 5 $A \cdot cm^{-2}$. The zero-gradient Baltic fuel cell allows for homogenous conditions (differential test cell), and it allows to control the pneumatic clamping pressure, applied directly on the active area of the fuel cell. An absolute compression pressure of 4 bar was used in all experiments. This value was already optimized in previous experiments conducted at DLR. Two commercial catalyst coated membranes (CCM), were used for the tests performed, which were designated as CCM_1 and CCM_2**.** Specifications regarding these CCMs are present on Table 3.1. A commercial GDL was used for both tests, which consists of a backing made of carbon fibers along with a MPL.

Table 3.1 *– CCM specifications, used for stressor and driving cycle tests.*

	Commercial CCM_1	**Commercial CCM_2**
Catalytic active phase	Pt suported on carbon	Pt supported on carbon
Cathode catalytic loading	0.4 mg cm^{-2}	0.5 mg cm^{-2}
Anode catalytic loading	0.08 mg cm^{-2}	0.1 mg cm^{-2}
Mebrane thickness	15 µm	15 µm
CCL thickness	10 µm	10 µm
ACL thickness	7 µm	5 µm

3.2 Implemented protocols for stressor and driving cycle tests

The **cell conditioning,** or break-in, is necessary to activate the cell and bring it to stable operating conditions, being the first step to execute after assembling the MEA, for both tests. The conditioning or break-in aims to assure the cell potential will be stable before the test initiation [48]. The cell conditioning was executed at 80 ºC, on a differential cell, with air gas flow rate of 6 L min^{-1} and hydrogen gas flow rate of 2 L min^{-1}. Hydrogen and air flow rates were kept at a stoichiometry of 8 and 10, respectively. The RH at the cathode and anode was 100 %. The gas outlet pressure (absolute)

at the cathode and anode was set as 2.5 and 2.3 bar, respectively. The conditioning was performed at both galvanostatic and potentiostatic mode, using the electronic load type Höcherl & Hackl ZS1806NV. Firstly, the potential was set at 0.6 V for one hour. Afterwards, the load was set as 2 A cm^{-2} for one hour, and as 3 A cm^{-2} for the following hour. Finally, the load was set as 2 A cm^{-2} overnight. Figure 3.1 summarizes the AST protocol followed for the implemented stressor tests and driving cycling test.

In accordance with Figure 3.1, regarding **stressor tests** with CCM_1 (after conditioning the cell), it was performed the beginning-of-life (BoL) *in-situ* characterization. *In-situ* characterization throughout all experiments involved 2 polarisation curves followed by cyclic voltammetry (CV), linear sweep voltammetry (LSV), ionic conductivity resistance (ICR), and electrochemical impedance spectroscopy (EIS) measurements. Then, the AST was initiated for around 110 hours and afterwards, it was performed a long stop (LS) of 24 hours, in which the gas supply was interrupted, and the load was switched off. The middle-life characterization was performed (ML1) similarly to BoL, and then AST was continued again for 110 hours. Another LS was performed for more 24 hours and thereafter, the second middle-life characterization was performed (ML2). Finally, the AST was conducted for more 110 hours, being followed by the third LS of 24 hours, ending with the end-of-life characterization (EoL). The LS consists of a total shutdown of cell , in which gas supply is stopped and cell temperature reduced to room temperature, allowing recovery of reversible potential losses. Three LS of 24 hours were performed, and irreversible degradation rate can be described by a linear regression of potential values after recovery steps. In case of **driving cycle** test conducted with CCM_2 and CCM_1, it was performed *in-situ* characterization at BoL, ML and EoL. Two LS of around 12 h were performed after 200 driving cycles duration test, as can be seen in Figure 3.1.

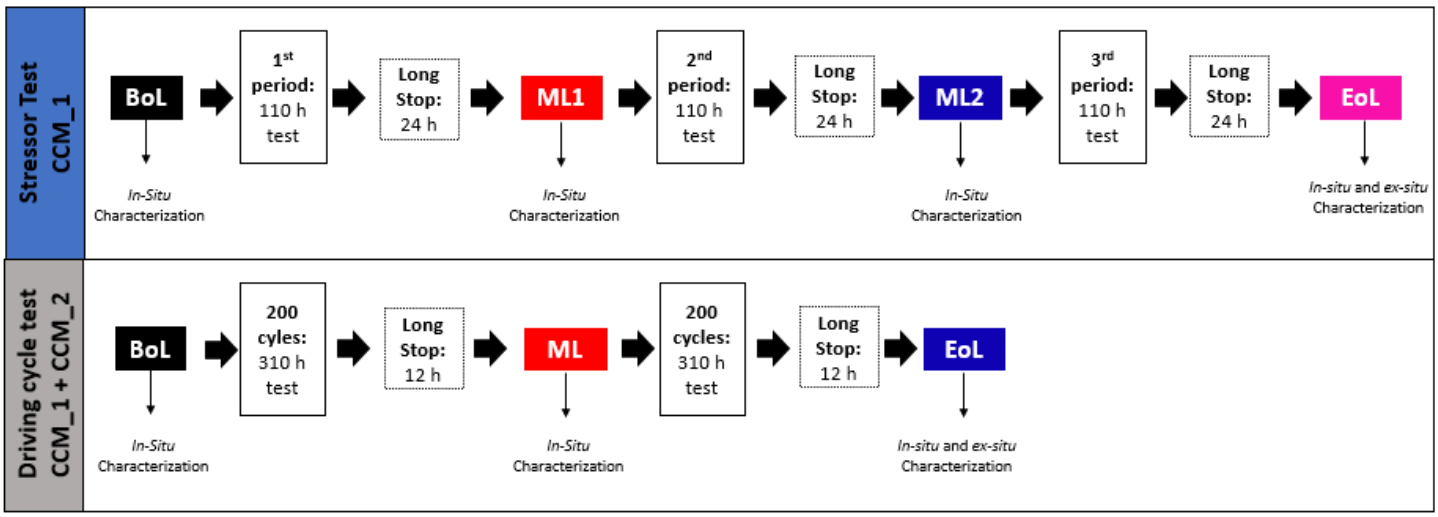

***Figure 3.1**- AST implemented for the degradation study of CCM_1 (stressors) and CCM_1 and CCM_2 (driving cycle) and commercial GDL.*

3.2.1 Operating conditions for driving cycle test

The single cell test hardware, along with suitable operating conditions, minimizes both operation and degradation heterogeneity induced by state-of-the-art flow fields, regarding distribution of temperature, liquid water, and oxygen and hydrogen concentration [47]. The aim of using a

differential cell is to simulate and study in a single cell, the effect of local conditions representative of certain areas of a large area cell of a stack. These areas of a fuel cell stack, with parallel channels and counter-flow configuration, can be defined as inlet, middle and outlet conditions, according to the cathode flow field of a single cell within a stack. The main difference in inlet, middle and outlet stack regions is related to local temperature (mainly driven by increase of coolant temperature from inlet to outlet of the cell), oxygen concentration (decrease of O_2 concentration along flow field channels due to consumption for fuel cell reaction) and relative humidity (increase of RH along the channel due to accumulation of the water product), as defined in public deliverable report D4.3 of the FCH JU ID-Fast project [26]. In this thesis, the focus is on the middle area conditions, which are defined as shown in Table 3.2.

To simulate FC operation in automotive conditions, a driving cycle developed within the ID-FAST project was used [26]. Driving cycle test was carried out in a differential cell (see Figure A.3.2 from Appendix A.3), also called zero-gradient cell (details specified in subsection 3.1), which means that there are minimized and negligible gradients regarding gas concentration, humidity, and temperature [47]. Fixed gas flows were used corresponding to λ_{Anode} = 8 and $\lambda_{Cathode}$ = 10, at current density of 3 A cm^{-2}. Hydrogen and air flow feed to the cell was 2 L min^{-1} and 6 L min^{-1}, respectively. However, additional 2.4 L min^{-1} of N_2 gas was supplied to the cathode side, to achieve 15 % oxygen concentration, by reducing the partial pressure of oxygen in the feed gas. In a single cycle, the load varied from 0 A till 21 A (1.75 A cm^{-2}), adopting the following values: 0 A cm^{-2}; 0.1 A cm^{-2}; 0.25 A cm^{-2}; 0.59 A cm^{-2}; 1.28 A cm^{-2} and 1.75 A cm^{-2}. The temperature was maintained constant at the beginning of the cycle, at a temperature of 71 ºC. It was increased, however, for 90 ºC, at the high load region of 1.28 A cm^{-2} (15.3 A) and 1.75 A cm^{-2} (21 A), as can be seen in Figure 3.2. The pressure also increased for high load operation. The high load operation and low load operation, intend to simulate highway and urban driving, respectively. In table A.2.1 from Annex A.2, it can be seen in detail the load steps as well as operating conditions specifications applied in a single cycle. The differential cell used in the tests is shown in Figure A.3.2 of Appendix A.3.

Figure 3.2 shows the specific operating conditions, represented by a yellow indicator, which are of particular interest for potential degradation study. It was intended to understand how different operating conditions of the driving cycle, such pressure and temperature, would affect potential decay rates and the MEA performance. Therefore, in subsection 4.1.1 of results and discussion, potential decay rates were studied for 1.75 A cm^{-2} (21 A) and 1.28 A cm^{-2} (15.3 A), for high temperature (HT) and low temperature (LT). LT and HT were defined as FC operating temperatures between 70 and 80 ° C, and between 80 ºC and 90 ºC, respectively. Also, pressure was thought to influence cell performance. Thus, potential degradation rate study was conducted for 0.25 A cm^{-2} (3 A) and 0.59 A cm^{-2} (7.1 A), for low pressures (LP) of 1.4 bar and 1.9 bar, medium pressure (MP) of 1.52 bar and 1.9 bar, and high pressures (HP) of 2.48 bar and 2.75 bar, for cathode and anode side, respectively.

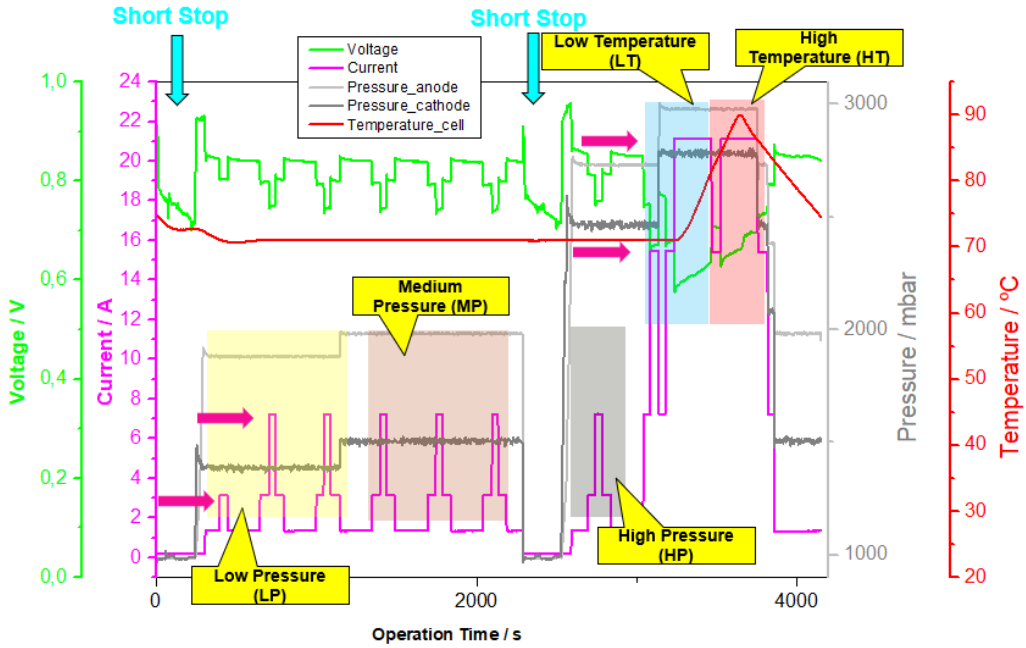

Figure 3.2 *– Test bench parameters during an ID-FAST load cycle recorded at 15 % oxygen concentration, with CCM_2. Short stops (SS) are identified in the figure and specific operating conditions within a cycle.*

Table 3.2 *– ID-FAST driving cycle different operating conditions representing cathode inlet, middle and outlet area of a generic parallel stack flow field. In this thesis, the focus was on middle conditions highlighted in bold face. Time duration percentage of each current density step, excluding SS, in a single cycle is also represented* [26].

		Low Temperature (LT)					High Temperature (HT)	
	Current density, ($A \cdot cm^{-2}$)	**0.1**	**0.25**	**0.59**	**1.28**	**1.75**	**1.75**	**1.28**
	Time percentage of total cycle duration, excluding SS (%)	**51.0**	**19.1**	**10.3**	**3.1**	**6.6**	**6.6**	**3.3**
Cathode inlet (21% O_2)	T cell, (°C)	68	68	68	68	68	85	85
	RH anode, (%)	100	100	100	100	100	100	100
	RH cathode, (%)	30	30	30	30	30	30	30
Cathode middle (15% O_2)	**T cell, (°C)**	**71**	**71**	**71**	**71**	**71**	**90**	**90**
	RH anode, (%)	**71**	**71**	**71**	**71**	**71**	**71**	**71**
	RH cathode, (%)	**59**	**59**	**59**	**59**	**59**	**59**	**59**
Cathode outlet (9% O_2)	T cell, (°C)	74	74	74	74	74	95	95
	RH anode, (%)	49	49	49	49	49	49	49
	RH cathode, (%)	77	77	77	77	77	77	77

The driving cycle contains both **short stop (SS)** and **cold soak (CS)** procedures, of four minutes and two hours' time duration, respectively. The SS represents the situation in which a real vehicle is rarely operated for several hours, without stopping. Therefore, the SS occurs with high frequency, always in the start and middle of each cycle, without cooling down of the system; a single driving cycle has approximately one hour duration. During SS the load and air flow are turned off and gas pressure is reduced to ambient; minimum fuel flow is kept at 0.2 L min^{-1}. On the other hand, the CS occurs every 5 cycles and mimics the situation in each a vehicle is stopped enough time to allow complete cool down of system. Therefore, the temperature of the cell is brought around 25 °C, which is the only difference from SS. A **long stop** occurs every 200 cycles and it represents the situation in which a fuel cell device is left in shut-down state without being started for an extended

period of time (days). Therefore, diffusion between anode and cathode will lead to gas mixture and to a significant concentration of oxygen on the anode side. It originates the hydrogen/air front that goes through the anode during start-up, being the main cause for carbon corrosion on CCL. It is considered a rare event, only occurring every 200th cycle. For the LS, both fuel and gas flow are stopped. In Figure 3.3 is present a scheme regarding driving cycle durability test program.

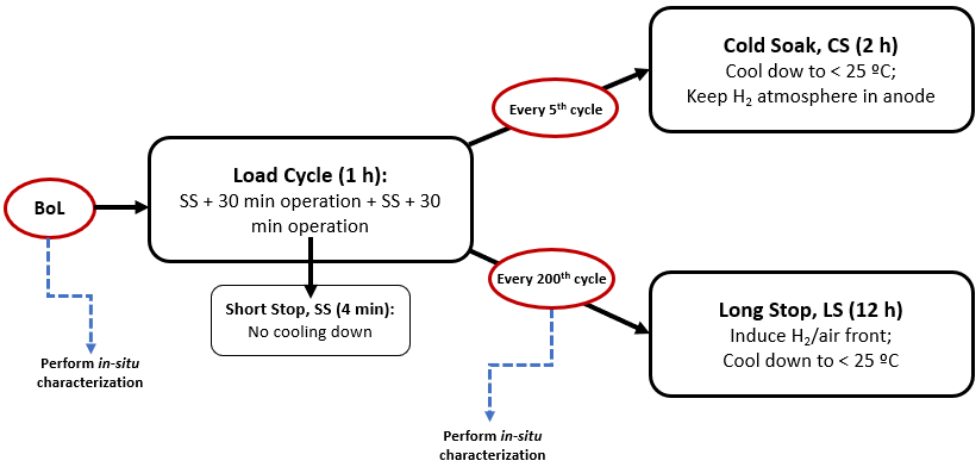

***Figure 3.3** – ID-FAST driving cycle durability test program.*

3.2.2 Operating conditions for stressor tests

Particularly stressing conditions for fuel cell were identified analysing the potential degradation at specific operating conditions, from previous driving cycle experiments data. Most stressing operating conditions were thereafter applied on a single cell test, denominated as stressor test. Four stressor tests were defined. Stressor tests differed only in cell operation temperature and the oxygen concentration (compare Figure 4.4 shown in section 4.1.1). It was intended to determine the effect of these parameters' variation on MEA degradation. The load, RH, and pressure was the same in all stressors; the applied load was 21 A (1.75 A cm^{-2}) and the cathode and anode outlet pressure was 2.3 and 2.5 bar, respectively. The cathode and anode RH was defined as 59 % and 71 %, respectively. For all tests, air gas flow rate of 6 L min^{-1} and hydrogen gas flow rate of 2 L min^{-1} were used. The hydrogen and air flow rates were kept at a stoichiometry of 8 and 10, respectively. Procedure for determining stressor´s operating conditions is explained in detail in subsection 4.2.1 of results and discussion.

3.3 Electrochemical characterization (*in-situ*)

3.3.1 Polarization curves

Polarization curves, or *I-V* curves, were obtained by monitoring the fuel cell current and potential during operation, by using an electronic load in galvanostatic mode, from open circuit potential (OCP) to high current densities (4 A cm^{-2}), with retention time of 3 minutes. The data was acquired every 3 seconds. For the polarisation curves presented in this thesis, it was considered an average of potential and current values over the last 21 s of dwell time. Two polarization curves (for each life stage) were recorded in both ascending and descending direction, being performed at 80 ºC, with air gas flow rate of 6 L min^{-1} and hydrogen gas flow rate of 2 L min^{-1}. The hydrogen and air flow

rates were kept at a stoichiometry of 8 and 10, respectively. The RH of cathode and anode was 100 %. The gas outlet pressure of cathode and anode was set as 2.5 and 2.3 bar, respectively. Polarisation curves were performed at 21 % oxygen concentration, for all tests performed (stressor test and driving cycle test).

3.3.2 Cyclic voltammetry (CV)

The CV allows to measure the electrochemical surface area (ECSA) of CL [49]. The cathode was chosen to be the working electrode (WE), while the anode is used as CE/RE, since the ORR has more interest due to its sluggish kinetics [35]. CV measurements were performed using Zahner potentiostat IM6 with PP240 load. To measure cathode CV, 200 mL min^{-1} of H_2 and N_2 were fed to anode and cathode, respectively, with 100 % RH, at ambient pressure and temperature. The potential of the WE was swept at 20 mV s^{-1} and three cycling potentials were performed ranging from 0.06 to 1.0 V. Firstly, it was swept in the anodic direction, to oxidize the adsorbed hydrogen to H^+. Then, in the cathodic reaction, to reduce H^+ back to adsorbed hydrogen, as can be seen in Figure 3.4. The potential range between 400 and 600 mV is usually the limiting current region which is free of adsorption and desorption processes on Pt, which corresponds to the double layer [34].

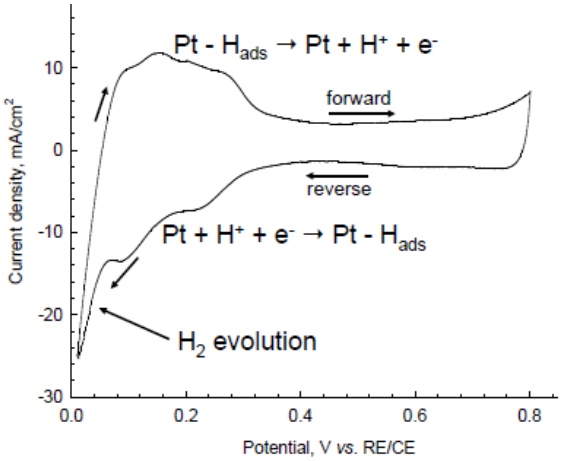

***Figure 3.4** - Cyclic voltammogram of PEM fuel cell catalyst layer for ECSA analysis, extracted from* [50].

The electrochemical surface area (ECSA) is calculated accordingly to equation (25), by measuring the charge area of hydrogen adsorption or desorption peak in the CV measurements, in which q_{Pt} is the charge density obtained from the CV experiment (μC $cm^{-2}_{electrode}$), L is the Pt loading in the electrode ($g_{Pt}\ cm^{-2}_{electrode}$), and Γ is the charge required to reduce a monolayer of protons (Γ=210 μC cm^{-2}_{Pt}) [24][50].

$$ECSA = \frac{q_{Pt}}{\Gamma \cdot L} \tag{25}$$

3.3.3 Linear Sweep Voltammetry (LSV)

LSV was conducted for determining the crossover current of hydrogen from the anode to the cathode. During LSV, a suitable inert gas, such as nitrogen, must be used to purge the fuel cell cathode, while hydrogen is fed to the anode. The anode functions as both counter electrode (CE) and reference electrode (RE). The working electrode (WE) was swept by means of a linear potential scan to potentials at which hydrogen gas present at the cathode is oxidized [35]. Humidified nitrogen and hydrogen, with 100 % RH, were supplied to the cathode and anode, respectively, both at flow rates of 200 mL min^{-1}. Pressure of the cathode and anode outlet was defined as 1.5 bar. The working electrode was scanned at 2 mV s^{-1}, from 0.01 V to 0.8 V *vs.* CE/RE. The electrolyte is intended to be ionic but not electronic conductor. However, with membrane thinning or pinhole formation, cell electrical resistance decreases, and internal short circuits between electrodes may occur. The hydrogen crossover flux (J_{H_2} in mol cm^{-2} s^{-1}) is determined by the output hydrogen limiting current density (I_{H_2} in A cm^{-2}), according to equation (26) [35]. A cell with high electrical resistance (infinite) will present a constant electrode potential-independent current. However, linear increasing current means there may be internal shorting, I_{SC}, and therefore, the cell will present a finite and lower electrical resistance [35]. The electrical resistance, R_{sc}, can be estimated according to equation (27) and it represents the electrical insulation of the MEA, whose decrease can accelerate the MEA aging by creating some local hot spots on the MEA at high potentials. I_{cross} is the cross leakage current, while $I_{H_2}$and I_{SC} represent the hydrogen crossover current and the short-circuit current, respectively [49].

$$J_{H_2} = \frac{I_{H_2}}{nF} \quad (26)$$

$$I_{cross} = I_{H_2} + I_{SC} = I_{H_2} + \frac{U}{R_{sc}} \quad (27)$$

3.3.4 Ionic Conductivity Resistance (ICR)

The ionic conductivity resistance, which is the proton conductivity resistance through the catalyst layer, was analysed by performing EIS measurement. The IC was measured in 0.5 V potentiostatic mode, with 5 mV amplitude from 500 mHz to 100 KHz frequency, passing nitrogen and hydrogen on the working and counter electrode, respectively. Operating conditions used were the same as LSV. It allows to discriminate ionic transport limitations in the membrane and CCL. In fact, ionic resistance, R_{ionic}, through the CCL manifests trough a straight line at high frequencies (ideally 45º) in Nyquist plot. R_{ionic} is obtained by the length of the Warburg-like region (X), that has 45º slope, projected onto the real impedance axis, XX, with transmission line model (TLM), as can be seen in Figure A.i from Annex A.i [5][51]. Equation (28) depicts how to determine the $R_{ionic,}$ according to TLM.

$$X = \frac{R_{ionic}}{3} \quad (28)$$

3.3.5 Electrochemical Impedance Spectroscopy (EIS)

EIS allows to quantify the different components of the cell potential losses [6]. EIS measurements were performed in galvanostatic mode, in the frequency range of 100 mHz to 100 kHz. The operating conditions were the same used for the polarization curves. EIS experiments were conducted at three different current densities: low current density (0.2 A cm^{-2}), medium current density (1.75 A·cm^{-2}) and high current density (3 A cm^{-2}) for 100 mA, 500 mA and 1 A of amplitude, respectively. These current densities were chosen as they provide crucial information regarding ohmic phenomena, charge transfer kinetics and mass transport losses, respectively [48][49]. In EIS measurement, the impedance of the fuel cell is measured through the response of an alternating current with varying frequency [20]. The obtained impedance values are plotted in a Nyquist plot, that consists of one or several arcs resulting of different impedance elements. System impedance is a combination of resistance, capacitance, and inductance. While capacitors and inductors result in the imaginary vector of impedance and affect both phase and amplitude of the signal, resistance on the contrary presents the real vector of impedance and has no effect on the phase [1].

At low current densities, the impedance of the cell is influenced by the electrode kinetics of ORR. The EIS shape forms a single semi-circle, in which the high frequency resistance (HFR) that is intersected with the real axis in the spectrum, corresponds to the ohmic resistance, R_Ω [20]. HFR is composed by proton conduction resistance of the membrane and electrical contact resistances, that are compression dependent, at the flow field/GDL and GDL/CL interface [11]. The difference between the low frequency resistance (LFR) and HFR corresponds to charge transfer resistance, R_{CT}, (measure of electrode kinetics), due to ORR, given by the arc diameter. At medium current densities, there is a decrease in R_{CT}, which means the diameter of the circle decreases; moreover, mass transport resistance of oxygen in the cell, R_{MT}, can be seen at low frequency impedance region, represented by a second semi-circle. Finally, at high current densities, R_{MT} becomes more accentuated, leading to a larger mass transport semi-circle [1][20]. Figure 3.5 represents a typical PEMFC Nyquist plot with HFR and LFR identified. In the figure is represented the total resistance, R_T, which corresponds to the arc diameter (summation of R_{MT} and R_{CT}). R_Ω includes electrolyte, contact resistance, and electronic resistance, and R_T envolves mass and charge transfer resistance.

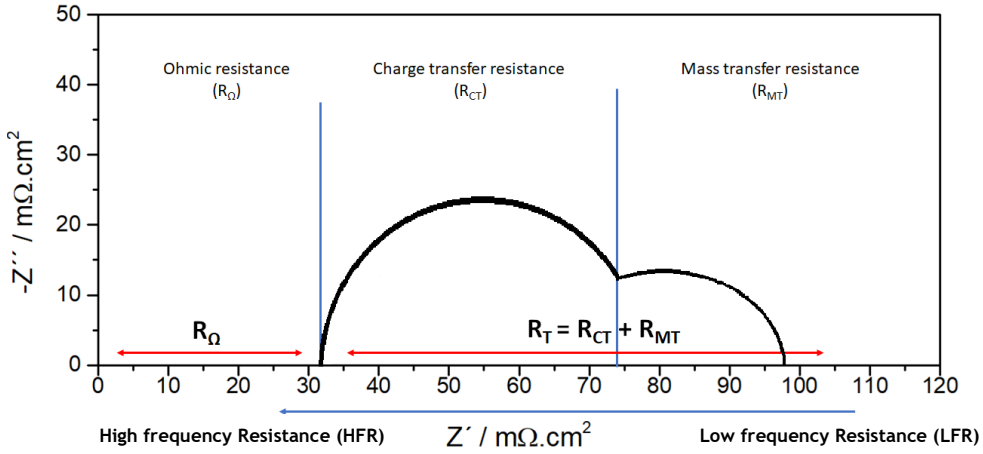

***Figure 3.5** – Schematic of a typical Nyquist impedance spectra of a PEMFC. R_{Ω} , R_{CT}, and R_{MT}, correspond to the ohmic, charge transfer and mass transfer resistance, respectively. R_T is the total resistance (summation of R_{CT} and R_{MT}).*

3.4 Physical Characterization (*ex-situ*)

3.4.1 Scanning Electron Microscopy (SEM)

SEM allows to visualize a sample surface, and it uses a focused beam of electrons to produce complex, high magnification images of a sample's surface topography. It allows to identify changes in microstructure of the electrode's catalytic layers. Cross-sections for SEM analysis were prepared by two different methods, which consisted of ion beam cutting and epoxy resin impregnation, which were conducted at Esslingen university and DLR, respectively. In the first method, ion cutting system JEOL IB-19520/CCP was used, with argon gas. Samples were fixed on sample holder by conductive carbon tape. For the second method, firstly the sample was vacuum-impregnated with epoxy resin. Then, a polished sample was obtained by series of griding and polishing steps, that resulted in a gradually smoother surface [52]. Samples were analysed with SEM from Zeiss (Gemini ultra plus), and EDX from Bruker (with X flash 5010 detector), at DLR. In Esslingen university, samples were analysed with JEOL field emission microscope JSM-7200F with Schottky-Emitter. Secondary electron images were taken by Everhard-Thornley-SE-detector and element distribution of lower and higher elements was done using a quadrupole backscatter detector. Analysis conditions for both samples preparation methods are given in data zone within SEM images.

3.4.2 X-ray photoelectron spectroscopy (XPS)

XPS allows to analyse the surface chemistry of a material. XPS spectra is obtained by irradiating a solid surface with a beam of X-rays while simultaneously measuring the kinetic energy of electrons that are emitted from the sample being analysed. For XPS, photoemission spectra were recorded using a hemispherical electron energy analyser, Thermo Scientific ESCALAB250, of a base pressure of 2×10^{-10} mbar. A monochromated Al Kα X-ray source (ScientaOmicron XM-1000) and Al Kα X-ray source (ThermoScientific XR4) were used for high-resolution spectra and non-high-resolution spectra, respectively.

4 Results and Discussion

4.1 Driving cycle test

The aim of the driving cycle is to simulate fuel cell (FC) operation in automotive conditions. In this section, driving cycle tests results regarding potential degradation and electrochemical characterization, performed with two commercial CCMs, will be analysed.

4.1.1 Potential Degradation and fuel cell performance

Two driving cycle experiments were conducted for 400 cycles, for cathode middle condition, with CCM_1 and CCM_2, according to Table 3.2. The active area of the cell is the same, in both tests, equalling 12 cm^2. The GDL size used was of 3×4 cm^2 (see Figure A.3.1 of Appendix A.3). The first was performed with 17.7 % oxygen concentration, due to test bench limitations, while the second was with 15 % oxygen concentration, as defined in Table 3.2 for the driving cycle middle condition. Potential evolution with operation time, for both driving cycles, can be seen in in Figures A.4.1 and A.4.2 of appendix A.4. Regarding 15 % oxygen concentration driving cycle, for around 37 h (from 90 h till 127 h of operation), the FC heating system was turned off due to unscheduled water refill. Figures 4.1 and Figure 4.2, show the potential degradation for individual current steps applied during the driving cycle, performed with CCM_1 and CCM_2, respectively.

In Figure 4.1, the potential decay during the first 200 cycles was found to be faster and more detrimental than during subsequent 200 cycles. For the last 200 cycles of 17.7 % O_2 concentration driving cycle, there is negative potential decay rates for most current densities, which means the cell improved its performance during this period. This behaviour can be due to reversible degradation recovery due to the LS of 12 h. Possible reversible degradation can be associated with formation of platinum oxides on CCL surface, which can be reduced in the CCL due to low cathode potential during the LS [53]. Figures A.4.3 and A.4.4 of Appendix A.4 show potential degradation with time, for specific current densities, for 17.7 % and 15 % oxygen feed concentration, respectively.

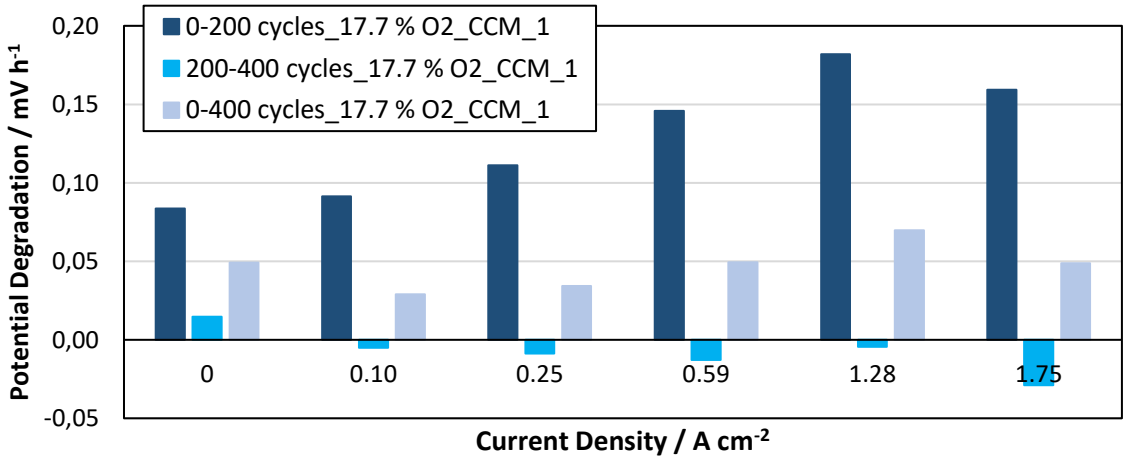

***Figure 4.1** - Potential degradation for different current steps, from ID-FAST driving cycle test performed for 17.7 % O_2 feed concentration, with CCM_1.*

In Figure 4.2, potential degradation from driving cycle, performed at 15 % oxygen concentration with CCM_2, was superior in the last 200 cycles, when comparing with first 200 cycles, for high current densities of 0.59, 1.28 and 1.75 A cm^{-2}. Potential degradation rate, for 1.75 A cm^{-2}, suffered a big increase, of 7.5 folds, from the first 200 cycles (0.016 mV h^{-1}) to the last 200 cycles (0.118 mV h^{-1}). OCP, on the other hand, had more degradation in the first 200 cycles (0.136 mV·h^{-1}), when comparing with the last 200 cycles (0.041 mV h^{-1}). OCP degradation rate suffered a decrease of 3.3 folds during the 2nd period of operation. There is a big increase in potential degradation rate, in the last 75 hours of operation, for high current densities, which can be observed in Figure A.4.4 from Appendix A.4. During that period, for 1.28 A·cm^2 and 1.75 A cm^2, the potential degradation rated equal 0.56 mV h^{-1} and 0.57 mV h^{-1}, respectively, being more than 30 times higher compared with degradation rates observed in first operation period. It is speculated that, if the driving cycle test had been continued for more 200 cycles, critical degradation of fuel cell would have been observed.

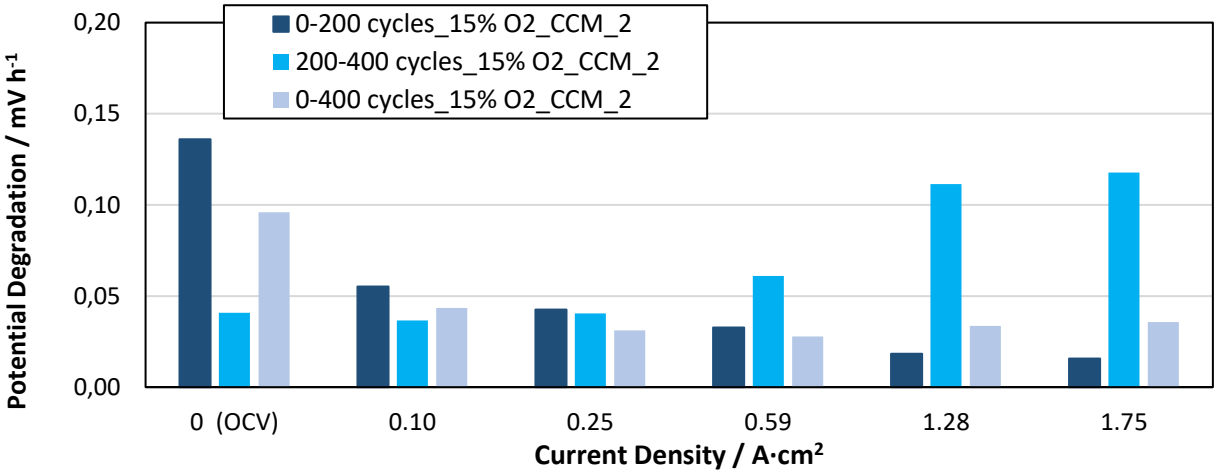

***Figure 4.2** – Potential degradation for different current steps from ID-FAST driving cycle test performed for 15 % O_2 feed concentration, with CCM_2.*

Potential degradation for different operating conditions was determined, according to subsection 3.2.1. It was intended to investigate the effect of pressure and temperature on MEA performance and potential decay rates. Figures A.4.5 and A.4.6 of Appendix A.4, show the potential evolution with operation time, for the specific operating conditions identified in Figure 3.2, for CCM_1 and CCM_2 driving cycle, respectively. Potential degradation rates, present in Figures 4.3, 4.4, 4.5, and 4.6, were calculated using equation (31) from subsection 4.2.2. The data present in Figures of Appendix A.4 was used for this determination.

In Figures 4.3 and 4.4, is represented potential degradation rates for the driving cycle performed with 17.7 % oxygen feed concentration, for specific temperature and pressure (defined in subsection 3.2.1), respectively. From both Figures, it can be observed that higher current densities accounts for higher potential degradation. In Figure 4.3, the highest degradation rate, which was approximately 0.2 mV h^{-1}, occurred at HT, at 17.7 % oxygen concentration, during the first 200 cycles. Regarding the effect of pressure, in Figure 4.4, it can be concluded that it does not have a significant impact on potential degradation.

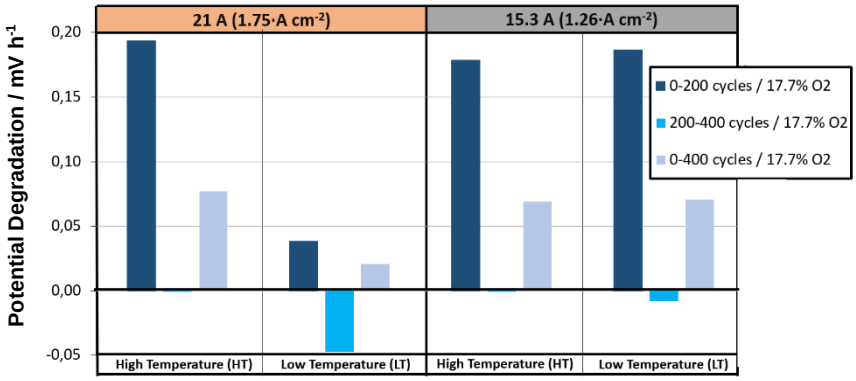

***Figure 4.3** – Temperature effect on potential degradation for high current densities, for 17.7 % oxygen concentration driving cycle test, performed with CCM_1.*

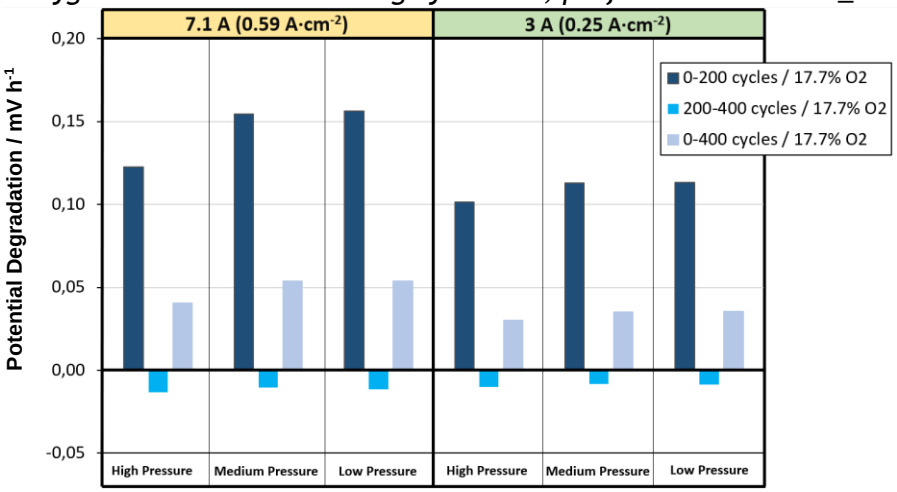

***Figure 4.4** – Pressure effect on potential degradation for high current densities, for 17.7 % oxygen concentration driving cycle test, performed with CCM_1.*

Figures 4.5 and 4.6, show potential degradation rate with pressure and temperature variation (defined in subsection 3.2), for the driving cycle performed with 15 % oxygen feed concentration. Similar to driving cycles performed with 17.7 % oxygen feed concentration, pressure variation does not seem to have a big impact on potential degradation. Regarding first 200 cycles, HT seems to be more detrimental for MEA, while LT presents almost no potential degradation, or even a potential improvement, represented by a negative value, during that period. However, analysing the last 200 cycles, potential degraded slightly more under LT operating condition, comparing with HT. Overall, considering the total 400 cycles, for 1.75 A cm^{-2} current, potential degradation was superior for HT.

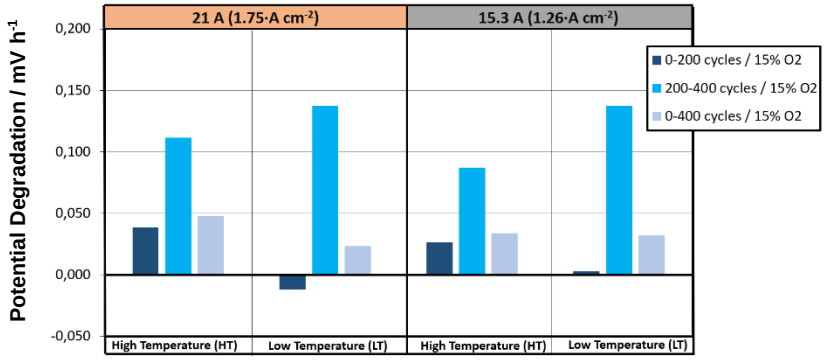

***Figure 4.5** – Temperature effect on potential degradation for high current densities, for 15 % oxygen concentration driving cycle test, performed with CCM_2.*

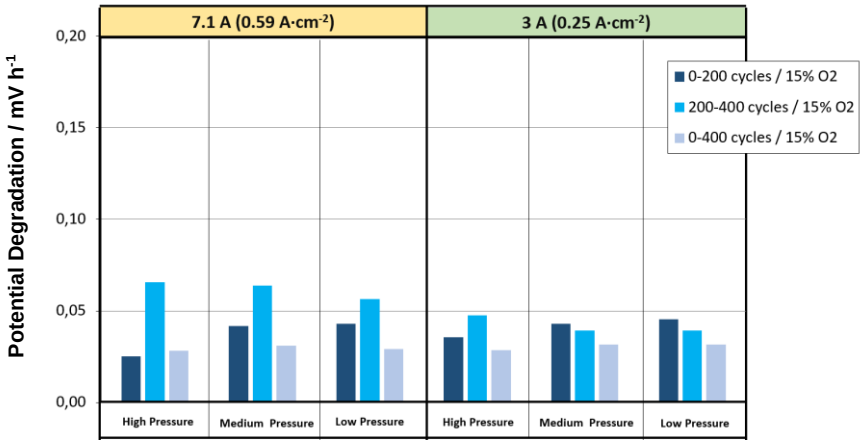

***Figure 4.6** – Pressure effect on potential degradation for high current densities, for 15 % oxygen concentration driving cycle test, performed with CCM_2.*

Comparing with 17.7 % oxygen concentration driving cycle performed with CCM_1, CCM_2 presents a tendency to degrade more in the last 200 cycles, while CCM_1 degrades more in the beginning of operation, stabilizing and even improving its performance after the LS. CCM_1 and CCM_2 have shown different behaviours in potential degradation, clearly showing that the impact of the driving cycle strongly depends on the used materials.

4.1.2 Electrochemical Characterization

In Figure 4.7 is visible that CCM_1 presents higher performance than CCM_2, at the BoL, particularly at high current densities. Polarisation curves in Figure 4.8 show there is a big decrease in performance with CCM_1, in first 200 cycles, which then stabilizes for the last 200 cycles. This sudden potential drop, as result of activation, ohmic and mass transfer resistance increase, is in accordance with ECSA reduction values (Table 4.1). CCM_2 has also an increase in mass transfer resistance after 400 cycles, however it is not such a steep increase as seen with CCM_1.

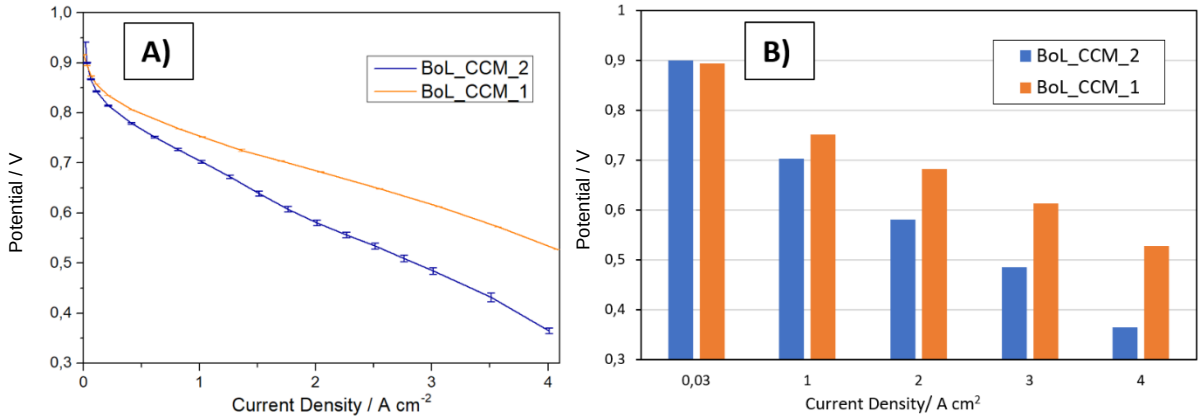

***Figure 4.7** – A) Polarisation curves and B) bar chart graph comparing performances at BoL, between CCM_1 and CCM_2.*

At the EoL of CCM_2 driving cycle test (15 % oxygen concentration), the cell is not operating stably, as can be seen in Figure 4.9. In fact, four polarisation curves were performed one after the other, in which the cell potential fluctuated considerably (Figure 4.9). In Figure 4.8 B) only the first polarisation curve was considered for the EoL representation. Throughout all tests performed during cell lifetime, it was observed that CCM_2 exhibited potential fluctuation which indicates it is prone

to flooding, having more potential oscillation at high current densities, comparing with CCM_1. In Figure 4.10, it is observed a large potential degradation increase with current density, during the 1st period, for CCM_1, reaching around 0.8 mV h^{-1} at 4 A cm^{-2}. CCM_2 had reduced potential degradation rate, of around 0.3 mV·h^{-1} at 4 A cm^{-2}, comparing with CCM_1. Potential degradation rates were determined from polarisation curves, after a refresh period.

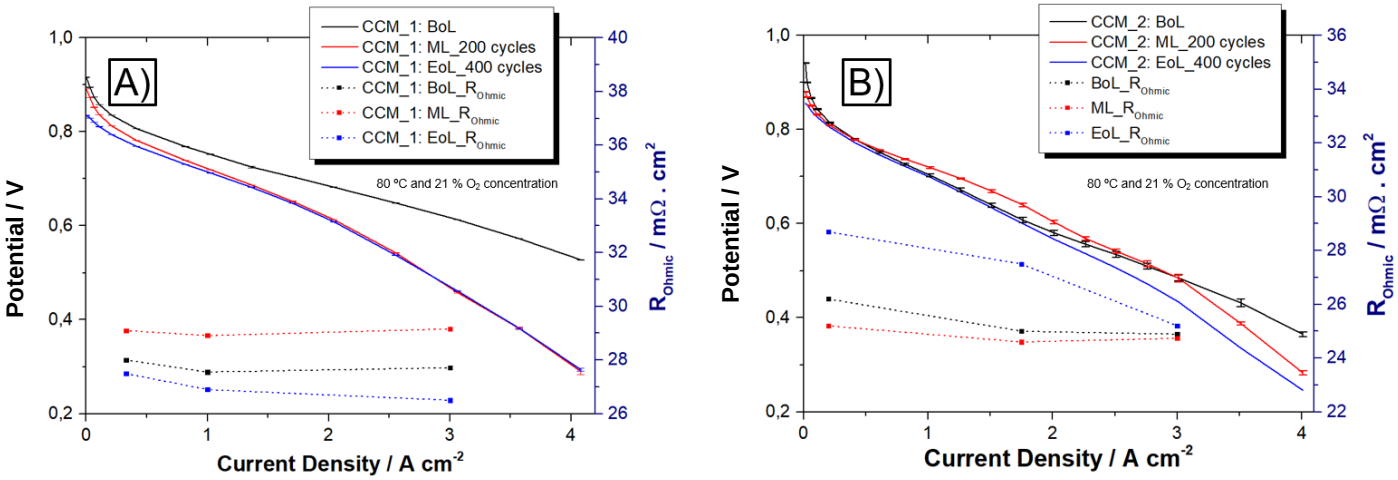

***Figure 4.8** – Polarisation curves and ohmic resistance representation for driving cycles performed with A) 17.7 % O_2 feed and CCM_1; B) 15 % O_2 feed and CCM_2, for BoL, ML1 and EoL characterization. Polarisation curves were all performed with 21 % O_2 feed and at 80 ºC.*

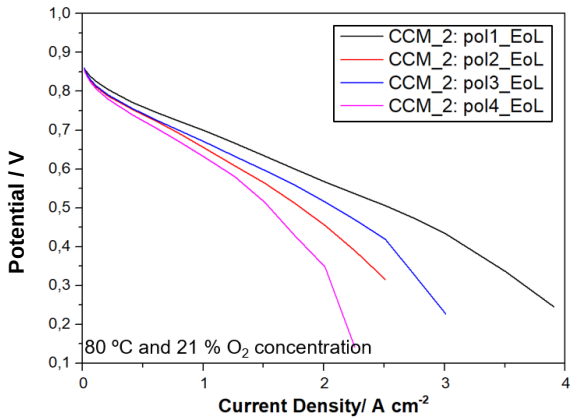

***Figure 4.9** – Polarisation curves at EoL from driving cycle with 15 % O_2 feed and CCM_2.*

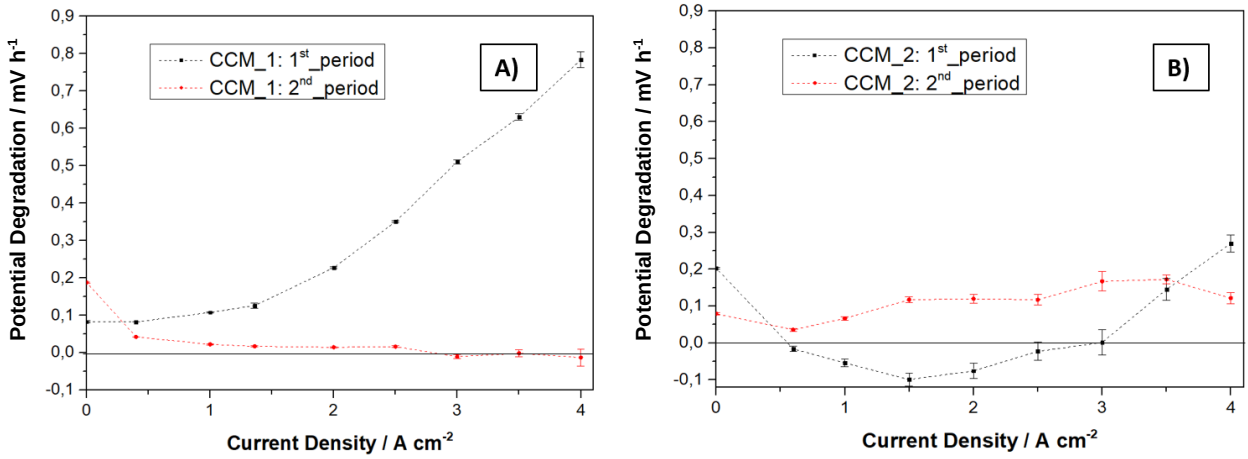

***Figure 4.10** – Potential degradation from polarisation curves, for driving cycle test performed: A) 17.7 % O_2 feed and CCM_1, B) 15 % O_2 feed and CCM_2, for BoL, ML, and EoL characterization.*

In Figure 4.8 it is observed that CCM_2 has lower ohmic resistance (R_Ω) than CCM_1. In Figure 4.8 B), R_Ω for CCM_2 exhibits a decrease in the first 200 cycles, at a current density of 1.75 A cm^{-2}, from 25.0 mΩ cm^2 down to 24.6 mΩ cm^2, which then increases at the EoL up to 27.5 mΩ cm^2, being 10 % higher than at the BoL. In Figure 4.8 A), CCM_1 shows in the first 200 cycles an increase in R_Ω, at a current density of 3 A cm^{-2}, from 27.7 mΩ·cm^2 up to 29.2 mΩ cm^2, which then decreases at the EoL down to 26.5 mΩ·cm^2. This behaviour is consistent with ICR measurements shown in Table 4.2.

Appendix A.5 shows electrochemical characterization measurements results for both driving cycles, using CV, EIS and IC, and LSV. EIS spectra were performed at 0.2 A cm^{-2} and 3 A cm^{-2}, and are represented in Figure 4.11 and 4.12, respectively, for 17.7 % and 15 % of oxygen feed concentration. EIS performed at 1.75 A cm^{-2}, is shown in Figure A.5.2 of Appendix A.5. Regarding activation losses, in Figure 4.11 A), CCM_1 shows an increase in R_T of 34 mΩ cm^2, between BoL and ML (after 200 cycles); a subsequent decrease in R_T of 26 mΩ cm^2 is observed, from 165 mΩ cm^2 to 139 mΩ cm^2, between ML and EoL, respectively. At high current densities of 3 A cm^{-2} (Figure 4.12 A)), where mass transport losses are dominant, R_T increased up by 167 mΩ cm^2, from 93 mΩ·cm^2 at the BoL to 260 mΩ cm^2 at ML, decreasing slightly at the EoL to 222 mΩ cm^2. It is possible that after 400 cycles the MEA suffered microstructural changes leading to an increment in pores formation, providing better reactant access. This behaviour is in accordance with polarisation curves and potential degradation for 17.7 % of oxygen feed concentration, analysed before. For CCM_2, it is suspected that the decrease in R_T from BoL till ML, visible in Figure 4.12 B), was due to flooding, which is thought to have led to an increased mass transfer resistance; water accumulated in the electrodes can partially-block the mass-transport of reactants to the catalyst active sites. As seen in Figure 4.9, CCM_2 is quite prone to flooding. For CCM_2, there is a considerable increase in charge transfer and mass transfer resistance in the last 200 cycles of FC operation, as can be seen in Figure 4.12 B) and Figure A.5.2 of Appendix A.5. However, it must be taken in account that, during the 4th polarisation curve performed at the EoL, the cell reached very low potential values as result of unstable operation (see Figure 4.9).

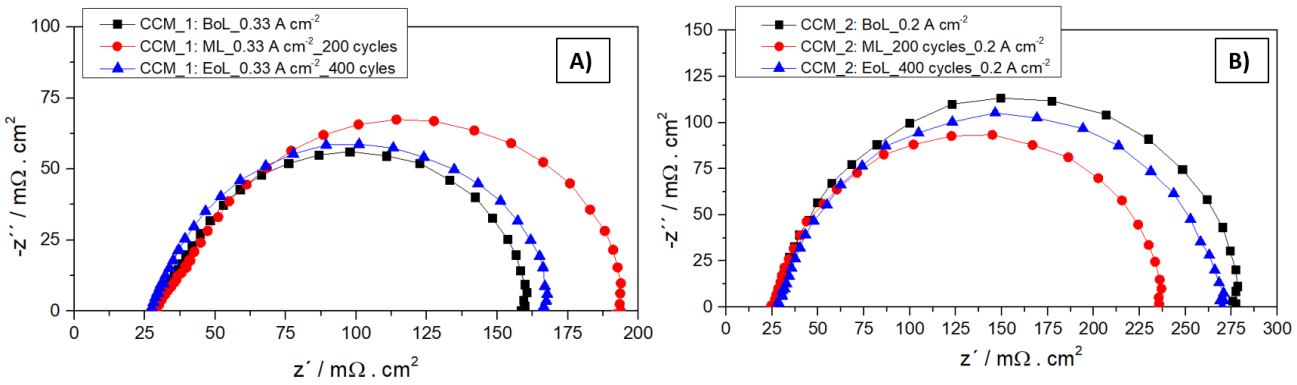

***Figure 4.11** – EIS performed for driving cycle test with A) 17.7 % O_2 feed (CCM_1); B) 15 % O_2 feed (CCM_2), for BoL, ML, and EoL characterization, for 200 mA amplitude and 0.33 A cm^{-2}, and 100 mA amplitude and 0.2 A cm^{-2}, respectively.*

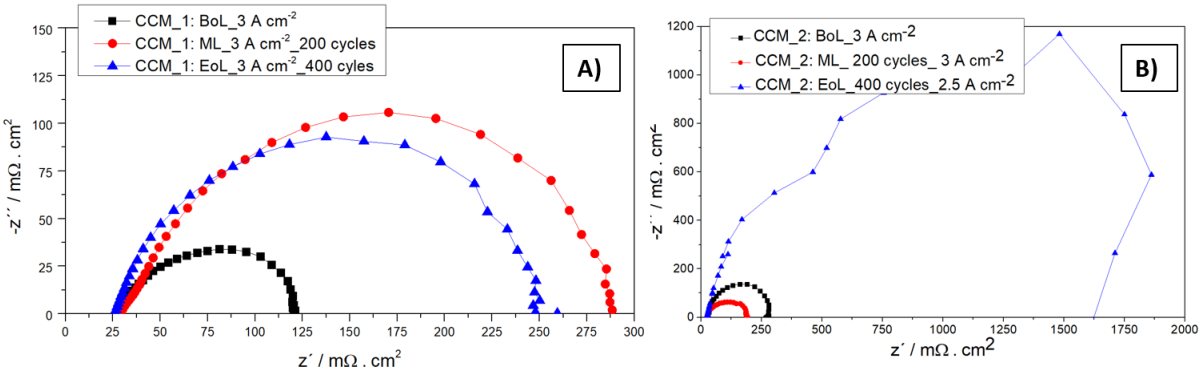

***Figure 4.12** – EIS performed for driving cycle test with A) 17.7 % O_2 feed (CCM_1); B) 15 % O_2 feed (CCM_2), for BoL, ML, and EoL characterization, for 1 A amplitude and 3 A cm^{-2}.*

The CVs, after 400 cycles of operation, became very tilted, as can be seen in Figure A.5.3 of Appendix A.5, for both experiments performed with 17.7 % and 15 % of oxygen feed concentration. This behaviour can be associated with the oxygen feed concentration reduction, as ID-FAST driving cycle performed with 21 % oxygen concentration, did not present this behaviour (see derivable D4.3 from ID-FAST project) [26]. According to Table 4.1, the ECSA (determined by equation (25)) decreased considerably for the first 200 cycles with CCM_1, by about 34.4 %, being consistent with potential degradation behaviour analysed before. In the last 200 cycles, the ECSA of CCM_1 only decreased 9.3 %; it is observed a gradual stabilisation of ECSA after prolonged driving cycle operation. Regarding CCM_2, ECSA suffered a reduction of 17.6 %, during the first 200 cycles, which is less than CCM_1. However, during the last 200 cycle, ECSA of CCM_2 decreased more than CCM_1, being around 14.7 %; The ECSA total decrease (for the 400 cycles performed) was 40.6 % and 29.7 %, for CCM_1 and CCM_2, respectively. Since the driving cycle causes a frequent change of potential during each cycle, it is speculated that there may be repetitive dissolution/reprecipitation mechanisms of Pt catalyst. Loss of Pt into the ionomer and particle growth arising from Ostwald ripening are also phenomena that can originate ECSA reduction during driving cycle. It should be highlighted that CCM_2 has higher Pt loading (0.5 mg cm^{-2}) than CCM_1 (0.4 mg cm^{-2}) and is common for CCM with lower loading to have stronger ECSA decay. This behaviour is observed since, at low Pt to carbon ration, catalyst nanoparticles are better distributed, leading to a lower degree of agglomeration and consequently, having a lower average size. Ostwald ripening phenomena is more frequent with small Pt particles (due to their lower stability) which can explain the faster ECSA decay with CCM_1, that has lower loading [40]. It is suspected for CCM_1 to have suffered from carbon corrosion, originating Pt particle detachment, as it was verified severe localized cathode CL thinning, for an aged CCM_1 cross section with 400 cycles, analysed with SEM (see subsection 4.3.1, Table 4.8). The oxygen feed concentration reduction, on the other hand, does not seem to have a big influence on ECSA reduction, as it was also verified a big decrease in ECSA for the driving cycle with 21 % OC (public derivable D4.3 from ID-FAST) [26]. This way, the main difference in ECSA values for the driving cycle tests performed with 15 % and 17.7 % of oxygen feed concentration can be attributed to the different CCM used, that have different loadings, and not to different oxygen concentration. Another assumption presumed is that load cycling induces bigger ECSA reduction, as

stressor tests performed with CCM_1 at a constant load, do not have such a big decrease (see Table 4.5). This can be due to holding time at higher potentials that causes Pt dissolution and allowing for sufficient time for its diffusion towards cathode/membrane interface. High potentials and possibly start-up/shut-down can lead to carbon corrosion from catalyst support and consequent Pt detachment resulting in the 34.4 % ECSA reduction, in Table 4.1. SEM analysis results, with 17.7 % of oxygen feed concentration driving cycle, show there is membrane degradation as fluoride percentage decreased close to cathode/membrane interface, in an aged MEA (see SEM Fluoride mapping – Figure 4.21 D1)). This degradation can possibly be due to chemical PFSA degradation at side chain level by radical attack. It is possible the membrane also suffered mechanical degradation as result of repetitive swelling/shrinkage triggered by temperature changes during driving cycle. It was also found a strong Pt concentration in the anode/membrane interface (Figure 4.21 D2)), in the driving cycle performed with 17.7 % of oxygen feed concentration.

***Table 4.1** – ECSA determination from CV, for driving cycle with 17.7 % O_2 feed (CCM_1) and 15 % O_2 feed (CCM_2), for BoL, ML and EoL characterization.*

Driving Cycle	**17.7 % OC (CCM_1)** ECSA (m^2/g_{Pt})	**15 % OC (CCM_2)** ECSA (m^2/g_{Pt})
BoL	47.1	50.5 ± 0.2
ML	30.9	41.6 ± 1.4
EoL	28.0	35.5 ± 1.7

Regarding ICR, it did not suffer great changes for CCM_2, which can be seen in Table 4.2. Ionomer distribution influences proton conduction in the CL. Therefore, it is speculated that ionomer is better distributed in CCM_2 rather than CCM_1. In fact CCM_1 presents a big increase in ICR of around 2 folds, of 3.3 mΩ to 6.8 mΩ from BoL till ML, which then decreases in the last 200 cycles. ICR was determined recurring to equation (28).

***Table 4.2** – ICR determination for driving cycle with 17.7 % O_2 feed (CCM_1) and 15 % O_2 feed (CCM_2), for BoL, ML and EoL characterization.*

Driving Cycle	**17.7 % OC (CCM_1)** ICR (mOhm)	**15 % OC (CCM_2)** ICR (mOhm)
BoL	3.3	1.51 ± 0.14
ML	6.8	1.30 ± 0.24
EoL	3.7	1.38 ± 0.27

LSV measurements, in Table 4.3, were only performed for CCM_2. The short circuit resistance, R_{SC}, which is explained in subsection 3.3.3, was calculated through equation (27), by performing a linear regression of LSV data results. The ordinate of the origin gives the hydrogen crossover current, I_{H_2}, while the inverse of the slope gives R_{SC}. R_{SC} decreases considerably, after 400 cycles performed with CCM_2, which can be seen by the steepening of slope in Figure A.5.5, from Appendix A.5. The R_{SC} decrease may originate local hot spots on MEA at high potentials, accelerating PEM aging. Regarding I_{H_2}, it increases slightly. It may be due to membrane thinning, which can result in electrical conductivity between the two catalytic layers from anode and cathode side but avoiding high hydrogen crossover current. For 21 % of oxygen feed concentration driving cycle, no such behaviour

was found in the CVs performed, allowing to take conclusions that reduction in oxygen concentration could be related to increase in R_{SC}, most probably attributed to electrolyte thinning, originating electrical shorts (public derivable D4.3 from ID-FAST) [26][35]. The effective transport of electrons in the FC is related to continuity of the carbon particle network [54]. Therefore, the decrease in R_{SC} may be due to carbon corrosion of the catalyst support from load cycling, and also by O_2 concentration reduction.

Table 4.3 *– Hydrogen crossover current (I_{H_2}) and short-circuit resistance (R_{sc}) determination from LSV, for driving cycle with 17.7 % O_2 feed (CCM_1) and 15 % O_2 feed (CCM_2), for BoL, ML and EoL.*

Driving Cycle	17.7 % O_2 feed (CCM_1)	
	I_{H_2} (mA cm^{-2})	R_{sc} (Ohm cm^{-2})
BoL	4.6 ± 0.4	444 ± 230
ML	1.2 ± 1.0	19 ± 1
EoL	5.3 ± 2.3	11 ± 1

4.2 Stressor Tests

In section 4.1.1, by evaluating potential decay rates at various current levels, for specific temperature and pressure, from the driving cycle performed with CCM_1, conditions being particularly stressing for the cell were identified. Different operando stressors, derived from the automotive driving cycle with 17.7 % oxygen concentration were identified, allowing to establish an AST protocol, including four stressor tests designated as Stressor 1, Stressor 2, Stressor 3, and Stressor 4. Main results regarding potential degradation rate and electrochemical characterization of the stressor tests will be presented in this section.

4.2.1 Determination of main stressors

From the driving cycle experiment performed with CCM_1, particularly stressing and detrimental conditions for the MEA were identified, which allowed the development of an AST protocol (see subsection 4.1.1). According to ID-FAST public derivable D4.3, reduced oxygen concentration can be considered as a stressor, leading to increased potential degradation rates, especially at high current densities [26]. The stressing conditions to adopt in AST protocol must involve high current density (1.75 A cm^{-2}), low oxygen feed concentration (15 %), and HT (defined as 95 ºC). Four tests were planned in total, at a constant load of 21 A (1.75 A cm^{-2}). Firstly, a reference condition (Stressor 2) was established, which consisted of the least stressing conditions (low temperature of 71 ºC and 21 % O_2 concentration). From this condition, three more tests were established, which were designated as Stressor 1, Stressor 3 and Stressor 4. Stressor 1 would allow to study temperature effect on PEMFC being performed at HT of 95 ºC and 21 % of oxygen feed concentration. Stressor 3, on the other hand, focus on oxygen feed concentration reduction effect and therefore, it was performed at 71 ºC and 15 % of oxygen feed concentration. Finally, Stressor 4 was a summation of both effects, HT of 95 ºC and low O_2 concentration (15 %), being expected to be the most detrimental stressor. In order to achieve 15 % oxygen concentration for stressor 3 and stressor 4, additional 2.4 L min^{-1} of N_2 gas were fed to FC cathode side. The main stressors that were identified, along with the operating

conditions (see subsection 3.2.2), are specified in Figure 4.13. The GDL size varied in the tests carried out, having its size increased in Stressor 3 and Stressor 4 (see appendix A.3, Figure A.3.1); in case of larger GDL, the GDL overlaps with the gasket, stabilizing the edge area of the membrane and improving mechanical stability. In both cases, the active area of the cell is the same, equalling 12 cm^2. Later, it is demonstrated that larger GDL overlapping with the gasket (see the scheme in Figure A.3.1 from appendix A.3) allows mitigation of mechanical stress on the membrane.

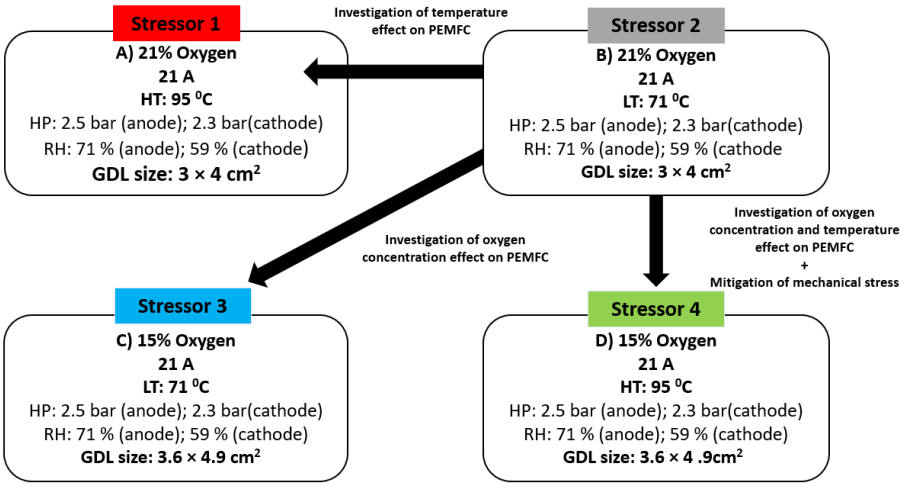

Figure 4.13 *- Stressors derived from load cycling tests and used in frame of this thesis.*

4.2.2 Potential degradation and fuel cell performance

All stressor durability tests were conducted successfully, according to the protocol defined in subsection 3.2. Potential degradation from these tests will be presented as follows. Figure 4.14 shows the potential evolution with operation time, for A) Stressor 1 (HT), B) Stressor 2 (reference condition), C) Stressor 3 (low O_2 feed), and D) Stressor 4 (HT and low O_2 feed), respectively.

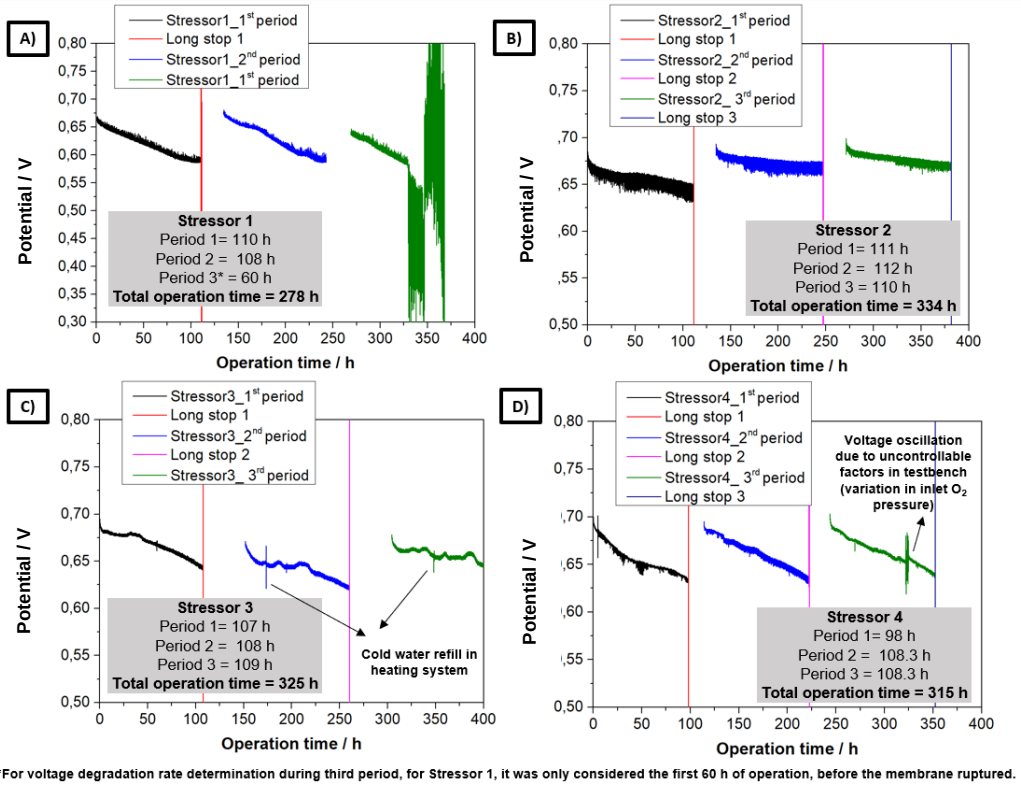

*For voltage degradation rate determination during third period, for Stressor 1, it was only considered the first 60 h of operation, before the membrane ruptured.

Figure 4.14 *-Potential evolution with operation time, for stressor tests (CCM_1).*

Stressor 1, performed at HT (95 ºC), can be considered as a significant stressor for MEA degradation. This becomes particularly evident when comparing the degradation rates summarized in Table 4.4. In fact, the membrane ruptured (see Figure A.6.1 A from appendix A.6), and it is assumed the formation of cracks after 330 h, which led to a sudden potential drop in the last period of operation, observed in Figure 4.14 A). These cracks occurred at the edges of the active area. The potential is increased, however, at around 347 h, since the electronic load was turned off due to severe potential drop, leading to prolonged operation at OCP for 50 h. Reference condition, as expected, was the least detrimental for the MEA as it caused less potential degradation, when comparing with the other stressors. It was expected for Stressor 4 to be the most critical stressor for the PEMFC since it combines Stressor 1 and Stressor 3. However, it was not the case. The explanation is that in Stressor 4, a larger GDL was used which overlaps with the gasket, leading to a stabilisation of the edge region of the membrane within the active area of the cell. Hence, the effect of the mechanical stress was mitigated in Stressor 4 test by adopting a 3.6×4.9 cm^2 GDL size, avoiding membrane rupture and improving membrane mechanical stability. Moreover, part of the potential loss that occurred during steady state operation stressor tests was recovered upon cell shutdown and consecutive restart after 24 hours. Generally, potential degradation consists of reversible and irreversible contributions. Reversible potential loss is calculated by the potential difference between the beginning of one durability period, $U_{\mathrm{Begin},n=i+1}$, and the end of the previous one, $U_{\mathrm{Final},n=i}$, according to equation (29), where i refers to operation period. Irreversible potential loss corresponds to the non-recoverable part of potential loss and is determined by the potential difference between the beginning of two consecutive periods, according to equation (30). Appendix A.7 shows a scheme on how to determine reversible and irreversible losses. For the determination of cell potentials at the beginning and end of an operation period, i, was considered an average of the first and last 30 min of operation, after cell was brought to nominal conditions, respectively. Potential degradation rate $\left.\frac{dU}{dt}\right|_{n=i}$, for each period i, is calculated through a linear regression of potential values versus operation time, as seen in equation (31). Appendix A.7 shows an example of potential degradation rate determination (Figure A.7.2).

$$\Delta U_{\mathrm{rev},n=i} = U_{\mathrm{Begin},n=i+1} - U_{\mathrm{Final},n=i} \quad (29)$$

$$\Delta U_{\mathrm{irrev},n=i} = U_{\mathrm{Begin},n=i} - U_{\mathrm{Begin},n=i+1} \quad (30)$$

$$U_{n=i} = \left.\frac{dU}{dt}\right|_{n=i} \times t_{n=i} + U_{\mathrm{Begin},n=i} \quad (31)$$

In Table 4.4, potential degradation rates and reversible and irreversible losses are provided, for each stressor test. Stressor 1 had the highest potential degradation rate of 0.93 mV h^{-1}, during last period. Potential degradation for Stressor 1 increased from period 1 to period 3. For Stressor 3, on the other hand, potential degradation is more predominant during first period, being 0.37 mV h^{-1}. Regarding Stressor 4, potential degradation was higher compared with Stressor 3, as it had an additional HT stressing condition besides the low oxygen feed concentration, being around 0.47 mV h^{-1} in all

periods. Reference condition potential degradation shows less variation among the operation periods, compared with other stressors.

***Table 4.4** –Stressor potential degradation and reversible and irreversible potential losses.*

	Stressor 1		Reference condition		Stressor 3		Stressor 4	
	ΔU reversible (mV)	ΔU Irreversible (mV)	ΔU reversible (mV)	ΔU Irreversible (mV)	ΔU reversible (mV)	ΔU Irreversible (mV)	ΔU reversible (mV)	ΔU Irreversible (mV)
After 1st Long stop	84	-11	40	-2	24	25	56	9
After 2nd Long stop	51	34	20	-4	56	-11	66	-12
	Potential Degradation (mV/h)		**Potential Degradation (mV/h)**		**Potential Degradation (mV/h)**		**Potential Degradation (mV/h)**	
1st period	0.68		0.20		0.37		0.49	
2nd period	0.82		0.11		0.28		0.47	
3rd period	0.93		0.14		0.20		0.47	

Regarding irreversible losses, Stressor 1 has the highest value of 34 mV, after the second LS, ascribed to mechanical stress on the membrane, leading to its degradation (as seen in SEM analysis, in Figure 4.21 A)). Reference condition, on the other hand, does not exhibit any significant irreversible potential loss. Irreversible losses can be attributed to catalyst structure change, such as Pt agglomeration during FC operation that decreases ECSA and reduces electrochemical performance. Pt agglomeration was observed with SEM for Stressor 1 and Stressor 3 aged MEA cross sections, as seen in Figures A.13.1-B) and A.13.3-B) of Appendix A.13. Stressor 2, on the other hand, showed less tendency to form Pt agglomerates [55]. Also PTFE decomposition from the GDL, as result of HT, can alter water balance in the MEA, being a possible irreversible loss in the case of Stressor 1. Indeed, Figure A.13.1-A) of Stressor 1 aged MEA, shows some degradation in PTFE fibers. In stressor tests, reversible losses are recovered mainly due to the LS. Stressor 1 had the greatest reversible potential recuperation of 84 mV, after the first LS. Membrane mechanical stress can be enlarged under high gas flow, HP, and high current densities operation. The LS, decreases the mechanical stress applied in the cell, allowing for potential recovery, which was quite significant in Stressor 1. From potential degradation analysis and SEM data (see subsection 4.3) can be concluded that HT is a stressing condition, that led, in case of Stressor 1, to membrane failure after 278 h of operation. Reduction in oxygen concentration is also stressing for FC. Nonetheless, a comparison between the effect of these two different operating conditions on fuel cell performance (HT and low oxygen concentration), is hard to assess, as GDL size differs from stressor 1 to Stressor 4.

4.2.3 Electrochemical characterization

Polarisation curves recorded during Stressor tests 1, 2, 3, and 4 are depicted in figure 4.15. Data of additional electrochemical characterization (CV, ICR, LSV and EIS at 1.75 A cm^{-2}), is shown in Appendix A.8. In Figure 4.15 is represented the polarisation curves along with ohmic resistance, for all stressor tests, for BoL, ML1, ML2 and EoL characterization. It can be observed that Stressor 1 had significant potential drop from ML1 till ML2, which is a strong indication of increased hydrogen crossover currents, which was observed through LSV measurements (see Table 4.7).

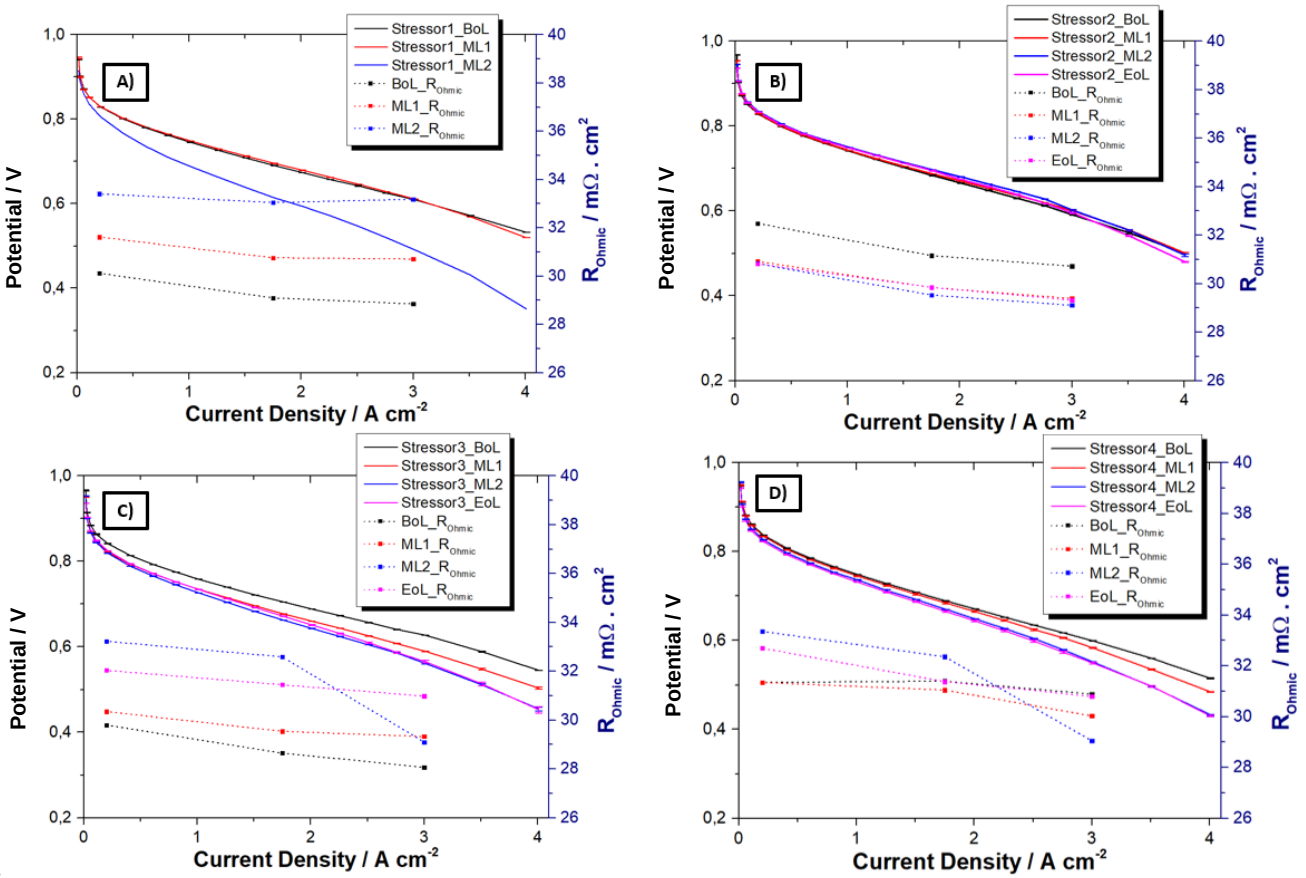

Figure 4.15 *– Polarisation curves and ohmic resistance representation for all stressor tests performed: A) Stressor1; B) Stressor 2; C) Stressor 3; D) Stressor 4, for BoL, ML1, ML2 and EoL characterization. Polarisation curves were all performed with 21 % O_2 feed and at 80 ºC.*

In the case of reference condition, there is not a big variation in cell performance after 334 h of operation as all polarisation curves are almost coincident. In Stressor 3 there is an increase in activation losses probably due to LT FC operation, together with oxygen concentration reduction. HT FC operation is usually associated with faster kinetics. Mass transfer resistance increase is visible for Stressor 3 and 4, mainly due to the decrease in oxygen concentration, as can be seen in polarisation curves of Figure 4.15 C) and D). By performing an equivalent circuit (subsection 4.2.4), for a current density of 3 A cm^{-2}, it was possible to quantify mass transfer resistance. Figure 4.23 shows a mass transfer increase with the decrease of the oxygen feed concentration. For Stressor 1 and 3, is observed an increase in ohmic resistance (R_Ω) after 330 h of operation time; at a current density of 3 A cm^{-2}, R_Ω increased 15 % (from 28.9 mΩ cm^2 to 33.2 mΩ cm^2) and 10 % (from 28.1 till 31.0 mΩ cm^2), respectively. This increase in Stressor 1 could be explained by loss of structural integrity of the membrane, which can be seen in Figure A.13.1-A) of Appendix A.13. Also, PTFE degradation from GDL, and its consequent deposit in the membrane, may increase ohmic resistance. It was expected for Stressor 4 to have higher R_Ω instead of Stressor 3, but GDL size alteration is a parameter that may affect ion conduction (due to changes in contact resistance and compression). In Figure 4.15, changes in R_Ω are less than 6 % for Stressor 2 and 4, so they can be neglected.

In Figure 4.16 is represented potential degradation rates as a function of current density, determined from polarisation curves that were performed after a refresh period. Stressor 1 leads to highest

potential degradation rate, during the second period, which was around 1.6 mV h^{-1} for high current density of 3 A cm^{-2}. Stressor 2 resulted in lowest potential decrease, when compared to other stressors, clearly underlaying low oxygen concentration and HT as severe stressors strongly affecting durability. Stressor 3 and Stressor 4 lead to similar potential degradation behaviour, presenting higher degradation rate during the 1st and 2nd period, and very low or negative degradation rate during the last period. This degradation behaviour is accordance with ECSA losses, that are significant in the first period, in all stressors (Table 4.5). It is speculated that main degradation occurs during this period, for Stressor 2, 3 and 4. Nonetheless, for Stressor 1 the main degradation was observed in the last period, due to possibly stronger mechanical degradation in this period, that generated high irreversible losses, which can be seen in Table 4.4.

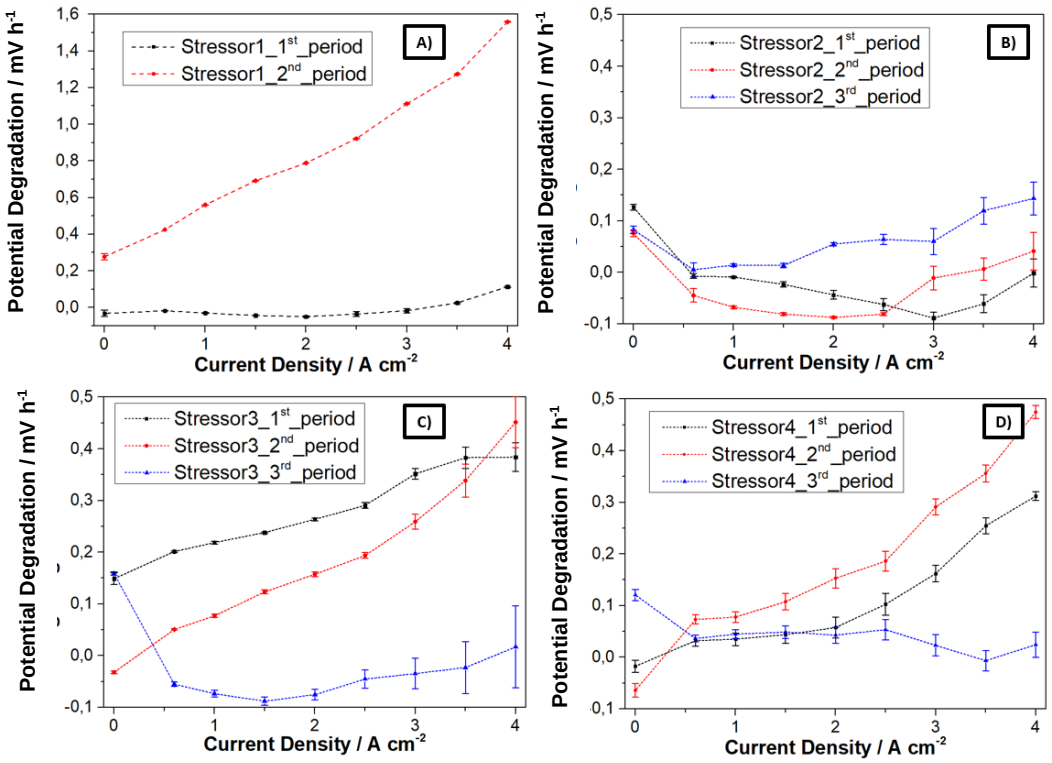

Figure 4.16 *- Potential degradation from polarisation curves, for all stressor tests performed: A) Stressor1; B) Stressor 2; C) Stressor 3; D) Stressor 4, for BoL, ML1, ML2 and EoL characterization.*

Figures 4.17 and 4.18 show the EIS performed for stressor tests, at a current density of 0.2 A cm^{-2} and 3 A cm^{-2}, respectively. Figure 4.17 is a good representation of the activation losses (charge transfer reaction), while Figure 4.18 is representative of mass transport resistance in GDL, membrane and CL (diffusion region). In Figure A.8.2 from Apppendix A.8, it is represented R_T and R_Ω (see subsection 3.3.5). In Figure 4.17 it is observed that Stressor 1 had lower charge transfer resistance, due to enhanced kinetics associated with HT. Stressor 2 presents a minor decrease in activation losses that may have have been due to electrode microstructural changes, improving its kinetics from BoL till EoL. In Figure 4.18, representative of diffusion region, it is observed a mass transfer resistance increase in Stressor 3 and 4, as oxygen diffusion through porous electrode to the reaction sites is hindered by the decrease of the oxygen feed concentration. R_T increased by

50 mΩ cm^2 and 117 mΩ cm^2, from BoL till EoL, for Stressor 3 and Stressor 4, respectively, being the increase more predominant in Stressor 4 as it had both effects of HT and low oxygen concentration. It is suspeted that HT degrades the PTFE from te GDL and the membrane, hindering reactant transport to the active sites and consequently, increasing mass transfer resistance. The loss of hydrophobicity associated with PTFE degradation, alters water management in the fuel cell, and it can lead to flooding. Regarding Stressor 1 in Figure 4.18 A), according to polarisation curve in Figure 4.15 A), it was expected a big increase in R_{MT} (from ML1 till ML2). However, this was not observed. It can been due to the fact that the *in-situ* characterization test protocol order was altered for Stressor 1. In fact, EIS was always performed after 4 hours of polarisation and, for Stressor 1 ML2 characterization, EIS was performed immediately after a 24 h LS. Therefore, it is speculated that the cell might have been not well activated and have less water content, originating less mass transfer resistance while measuring EIS. In Figure 4.18 B), in Stressor 2, there is a clear increase in R_T from BoL till ML1, which then remains constant till the EoL. This unexpectedly increasead resistance, remains to be explained, but it can be due to certain morphological changes in CL, resulting in a redistribution of the ionic and electronic pathways within the CL [56]. This increase even though not visible in Figure 4.15 B), was observed with the EIS at 3 A·cm^{-2}. Figure A.8.1 from Appendix A.8 shows the EIS performed for 1.75 A cm^{-2}.

Table 4.5, 4.6 and 4.7, show main results obtained with CV, ICR and LSV. It is important to highlight that for Stressor 1 BoL results, present in the tables mentioned before, it was considered and average of the BoL results from Stressor 2, Stressor 3 and Stressor 4.

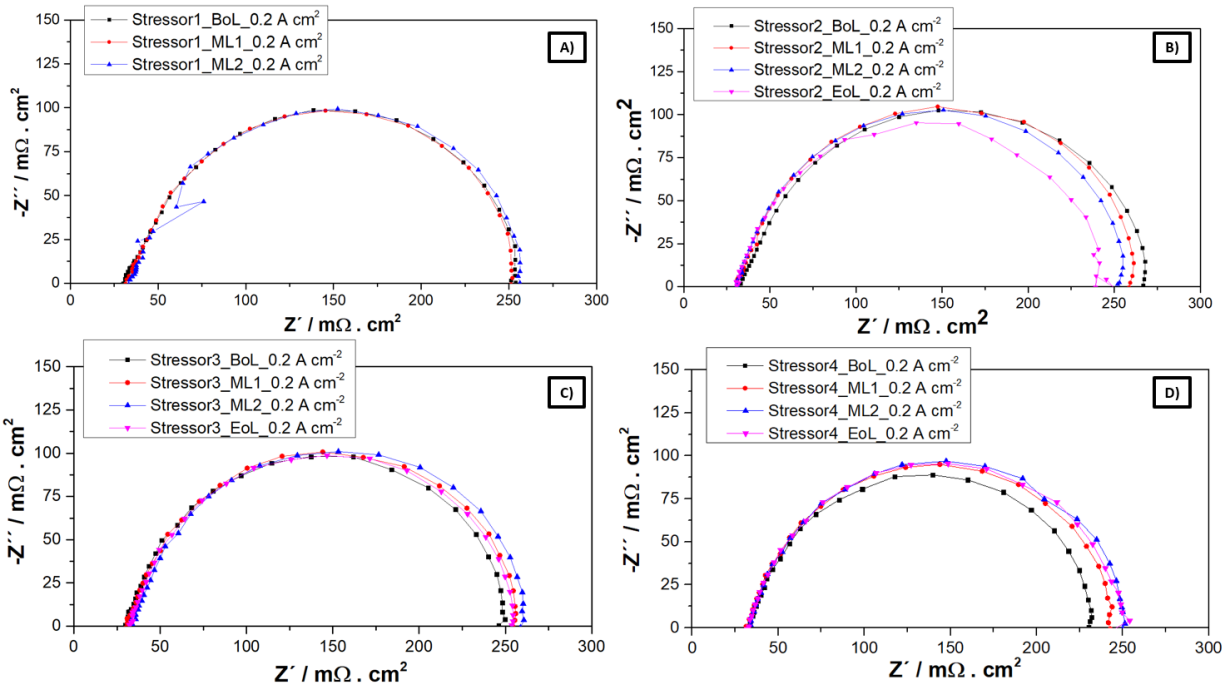

***Figure 4.17** – EIS performed for A) Stressor1; B) Stressor 2; C) Stressor 3; D) Stressor 4, for BoL, ML1, ML2 and EoL characterization, for 100 mA amplitude and 0.2 A cm^{-2}.*

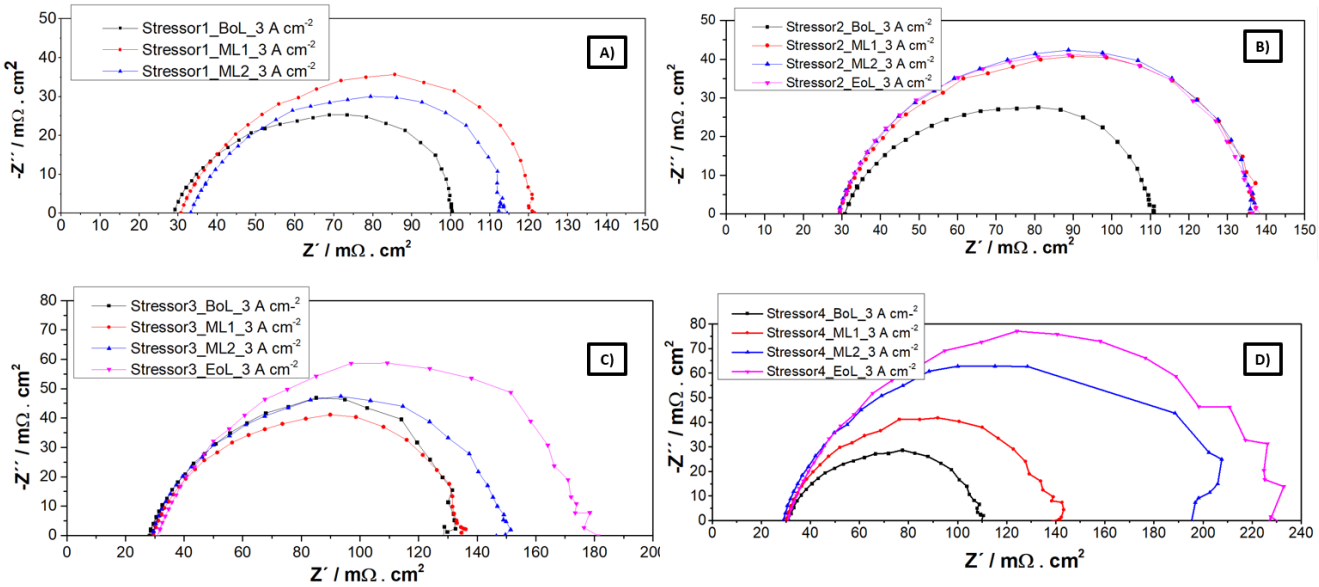

***Figure 4.18** – EIS performed for A) Stressor1; B) Stressor 2; C) Stressor 3; D) Stressor 4, for BoL, ML1, ML2 and EoL characterization, for 1 A amplitude and 3 A cm^{-2}.*

ECSA loss is used to measure the degradation of electrocatalyst caused usually by catalyst dissolution or ripening and/or carbon support corrosion [12]. From Table 4.5, is observed a significant decrease in ECSA , in all stressors, during the 1st period of FC operation. After the 1st period of operation, ECSA stabilizes, remaining almost constant throughout the two remaining periods. ECSA reduction is stronger in the begining possibly due strong Pt dissolution, which eventually stabilizes. ECSA reduction in the first period was around 25 %, 19 %, 20 %, and 10 %, for Stressor 1, 2, 3 and 4, respectively. Stressor 1 had the highest ECSA reduction, while Stressor 4 had the lowest. However, ECSA for BoL of stressor 4 has a large error and hence the assessement of ECSA loss in Stressor 4 test is uncertain. By conducting SEM analysis, in Figures A.13.1, A.13.2 and A.13.3 of Appendix A.13, it was found that Stressor 3 and Stressor 1 have Pt agglomeration, contrarily to Stressor 2. Therefore, HT and low oxygen concentration may induce Pt agglomeration in the CCL.

***Table 4.5** – ECSA determination from CV, for all stressor tests performed, for BoL, ML1, ML2 and EoL characterization.*

	Stressor 1	**Reference Condition**	**Stressor 3**	**Stressor 4**
	ECSA (m^2/g_{Pt})	ECSA (m^2/g_{Pt})	ECSA (m^2/g_{Pt})	ECSA (m^2/g_{Pt})
BoL	51.2*	51.8	54.0 ± 0.5	47.7 ± 5.8
ML1	38.4	41.9	43.2 ± 0.4	42.8 ± 1.1
ML2	37.4	39.9	41.2 ± 0.8	40.7 ± 1.2
EoL	-----	43.0	41.5 ± 0.8	40.2 ± 1.0

ICR allows to assess proton conduction resistance across the electrolyte towards reaction sites on CCL, which depends on the ionomer distribution across catalyst particles [57]. Table 4.6 shows ICR values for the four stressor tests performed. Stressor 1 has higher ionic conductivity resistance, which increases from BoL till ML2. For reference condition, ICR decreases slightly at the EoL. Stressor 4 presents the lowest ICR, which remains constant during 315 h of operation. Stressor 3, contrarily to Stressor 4, presents an increase in ICR. It was expected, for HT condition of Stressor 4, to have

induced higher ICR, as resemblance to Stressor 1. However, the GDL size was changed from one test to the other, which can have induced different behaviour (Appendix A.3).

***Table 4.6** – ICR determination for all stressor tests performed, for BoL, ML1, ML2 and EoL characterization.*

	Stressor 1	Reference Condition	Stressor 3	Stressor 4
	ICR (mOhm)	ICR (mOhm)	ICR (mOhm)	ICR (mOhm)
BoL	2.6	3.6	2.3 ± 0.3	1.8 ± 0.2
ML1	3.7	2.5	2.8 ± 0.9	2.2 ± 0.8
ML2	4.7	2.2	3.5 ± 0.2	2.0 ± 0.2
EoL	-----	2.2	4.2 ± 0.2	1.8 ± 0.1

The data in Table 4.7 shows that crossover current is similar for Stressor 2, 3 and 4. On the other hand, Stressor 1 has the highest hydrogen crossover current, of 8.57 mA·cm^2 at ML2, as well as the lowest short circuit resistance, which represents the electrical insulation of the MEA [49], being determined through equation (27) (subsection 3.3.3) . This result is in accordance with membrane rupture, which occurs in Stressor 1, at the EoL, as seen in Appendix A.6. For Stressor 1, the hydrogen crossover current increased 1.7 folds, from BoL to ML2. It is possible that this increase may have accelerated membrane degradation; crossover current might have led to membrane chemical degradation, in the case of Stressor 1, which is visible in SEM analysis results of aged cross section of the MEA (Appendix A.13). In fact, there is less fluoride content in the membrane of Stressor 1, shown in Figure A.13.1-B) of Appendix A.13, which can be due to radical attack on the ionomer.

***Table 4.7** – Hydrogen crossover current (I_{H_2}) and short-circuit resistance (R_{sc}) determination from LSV, for all stressor tests peformed, for BoL, ML1, ML2 and EoL characterization.*

	Stressor 1		Reference Condition		Stressor 3		Stressor 4	
	I_{H_2} (mA · cm^{-2})	R_{sc} (Ohm · cm^2)	I_{H_2} (mA · cm^2)	R_{sc} (Ohm · cm^2)	I_{H_2} (mA · cm^{-2})	R_{sc} (Ohm · cm^2)	I_{H_2} (mA · cm^{-2})	R_{sc} (Ohm · cm^2)
BoL	4.99*	290*	5.34	366	5.49 ± 0.32	2178 ± 2219	4.63 ± 0.25	213 ± 27
ML1	6.84	128	5.10	287	5.26 ± 0.18	1893 ± 1228	4.21 ± 0.30	464 ± 61
ML2	8.57	119	5.88	213	5.38 ± 0.30	2294 ± 2674	4.65 ± 0.39	1216 ± 854
EoL	-	-	4.44	146	4.96 ± 0.04	9550 ± 6633	4.92 ± 0.60	888 ± 265

4.2.4 Equivalent Circuit

By building an equivalent circuit (EC) model of the fuel cell, present in Figure 4.19, contributions of kinetic, charge transfer and mass transport of CCL can be separated [23]. Since anode activation losses have a very small contribution, compared with ORR, it was opted not to include it in the EC. The following EC model in Figure 4.19 was adopted for the stressor tests. The EC consists of four components in series, i) inductance (L) that accounts for possible interferences due to wires or other sources of disturbances; ii) a resistor (R_Ω) that describes MEA ohmic resistance and contact resistance of fuel cell components; iii) charge transfer circuit formed by CPE_1 in parallel with $R_{CT,c}$; and iv) mass transfer resistance circuit formed by CPE_2 in parallel with $R_{MT,c}$ [53]. Table A.9.1 from appendix A.9 presents all elements from the EC, with the respective errors, which were obtained with Zview

software. The fitting error was at relatively low level (in general lower than 6 %). It was intended to understand better electrode behaviour at high current densities (3·A cm^{-2}), in which oxygen diffusion is a limiting performance factor for the fuel cell [57]. Instead of using a capacitance for the double layer, it was used a constant phase element (CPE) since it has in account the porosity of the electrode [58]. The exponent of the CPE was defined as 0.9 (for an exponent of 1 CPE is equal with the capacitance) [55].

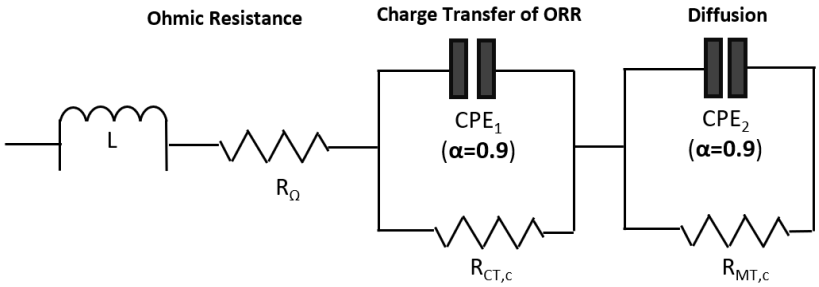

Figure 4.19 *– Equivalent circuit (EC) with ohmic resistance, charge transfer resistance of ORR and mass transfer resistance elements.*

Figure 4.20 presents a bar graph that allows to see the contributions of A) mass transfer and B) charge transfer resistance. Contributions of ohmic resistance are shown in Apendix A.9. Charge transfer resistance, R_{CT}, does not suffer big variations, when comparing with mass transfer resistance. It can be observed that Stressor 3 and Stressor 4 have the greatest mass transfer resistance at the EoL for 3 A cm^{-2}, of around 11.5 mΩ and 15 mΩ, respectively. This way, oxygen transport to the catalyst is hindered by a decrease in oxygen concentration. Moreover, by comparing stressor 3 with stressor 4, it can be inferred that temperature increase also contibutes to mass transport losses, possibly attributed to PTFE degradation. Stressor 3 and 4 had a total increase in R_{MT} of 4 mΩ and 10 mΩ, respectively. Stressor 2 has an increase in R_{MT} from BoL till ML1 of 2.6 mΩ, remaing constant till the EoL, as seen in Figure 4.20 A). Ohmic resistances are shown in Figure A.9.1, of Appendix A.9. Appendix A.6, shows aged CCMs from stressor, Stressor 1 severe degradation can be observed in Figure A.6.1 A). In appendix A.10 is given the cell efficiency for the four stressors, for a current density of 1.75 A·cm^{-2}. Stressor 1 has the lowest efficiency, at the EoL, of 40 %.

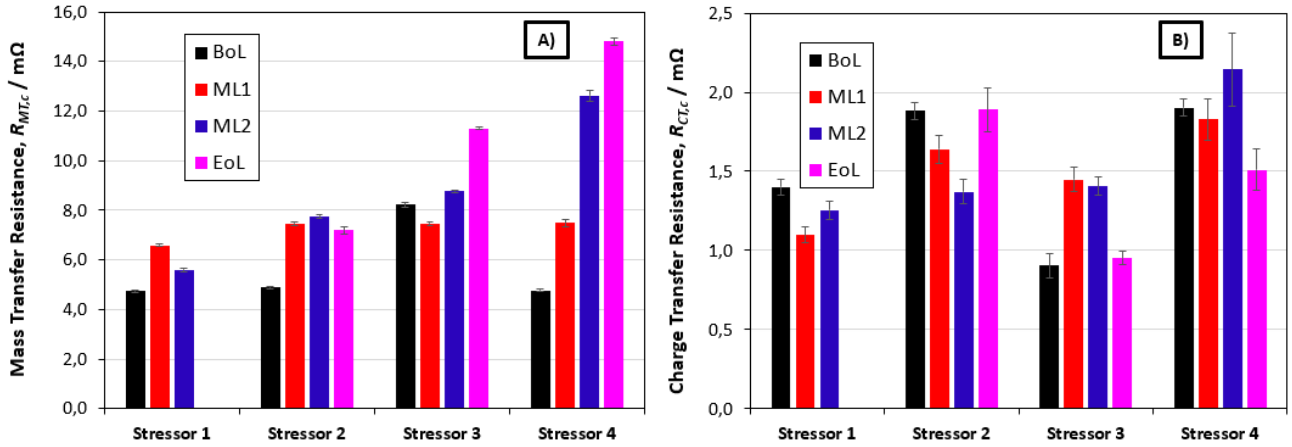

Figure 4.20 *– A) Mass transfer resistance and B) charge transfer resistance, from equivalent circuit, for stressor tests at BoL, ML1, ML2 and EoL characterization, for 3 A cm^{-2}.*

4.3 *Ex-situ* characterization

4.3.1 SEM analysis – stressor and driving cycle tests

The thickness of pristine (BoL) as well as aged CCMs (EoL) were determined from cross-sections images, obtained by SEM, with epoxy resin sample method preparation, which can be seen in Figure A.11.1 and Figure A.12.1 of Appendix. In Table 4.8 and Table 4.9 it is present the anode CL, cathode CL, and membrane thickness for aged MEAs from stressor and driving cycle tests, performed with CCM_1 and CCM_2, respectively. It can be seen changes in anode and cathode CL that denote slight thinning, in most of the samples. However, the driving cycle with 17.7 % of oxygen feed concentration presents a more pronounced decrease in cathode CL. This severe localized cathode CL thinning of 69 % can be due to carbon support corrosion and consequent Pt detachment. CCM_1 also suffers some membrane thinning in the tests performed with less oxygen concentration (Stressor 3 and driving cycle test with 17.7 % of oxygen feed concentration). This is in accordance with the speculated electrolyte thinning caused by reduced oxygen concentration, as was verified with CV and LSV performed for driving cycle tests. Regarding CCM_2, it seems to be more robust than CCM_1. Anode and cathode CL do not present big modifications for this CCM. However, membrane seems to have some localized thinning (Figure A.12.1 from Appendix A.12), which can also be due to compression on the flow field channels.

***Table 4.8** – Thickness of MEA components before and after aging, with CCM_1, for stressor and driving cycle tests.*

		Thickness, µm		
		Anode CL	**Cathode CL**	**Membrane**
BoL	Pristine CCM_1	8.8 ± 0.1	10.7 ± 0.2	17.8 ± 0.1
Driving Cycle EoL	400 cycles (17.7 % O_2 concentration)	6.5 ± 0.4	3.3 ± 0.4	16.7 ± 1.1
Stressor test EoL	Stressor 1 (High Temperature)	7.4 ± 0.1	9.8 ± 0.2	17.3 ± 0.3
	Stressor 2 (Reference condition)	7.2 ± 0.1	7.4 ± 0.3	17.5 ± 0.6
	Stressor 3 (15 % O_2 feed concentration)	7.0 ± 0.04	9.1 ± 0.01	16.5 ± 0.3

***Table 4.9** – Thickness of MEA components before and after aging, with CCM_2, for stressor and driving cycle tests.*

		Thickness, µm		
		Anode CL	**Cathode CL**	**Membrane**
BoL	Pristine CCM_2	3.1 ± 0.3	12.4 ± 0.9	20.1 ± 0.5
Driving Cycle EoL	400 cycles (15 % O_2 feed concentration)	3.1 ± 0.7	11.8 ± 1.8	18.5 ± 2.6

Figure 4.21 shows cross section SEM images from middle regions of CCMs from Stressor 1, Stressor 2, Stressor 3, and driving cycle test with 17.7 % of oxygen feed concentration. Other SEM images of cross sections also analysed by resin epoxy impregnation and ion cut method, are present in Appendix A.13. In Figure 4.21 A) it is visible the physical-chemical degradation of the membrane from Stressor 1 from both epoxy resin impregnation and ion cut samples preparation. The chemical degradation is most possibly due to peroxide and hydroperoxide radicals attack on the membrane, as result of direct reaction between oxygen and hydrogen. Stressor 2, presented on figure 4.21 B) does not seem

to have visible degradation. Figure 4.21 C1) and C2), representing Stressor 3, allows to visualize a Pt band formation close to the cathode side possibly as result of reduced oxygen feed concentration. Regarding driving cycle, in Figure 4.21 D1), it is observed a decrease in fluoride content close to cathode CL, attributed to membrane degradation. It was also found an interesting phenomenon, which consists of increased Pt concentration on the anode side, in the interface with the membrane, which remains to explain. In Figure A.14.2 from appendix A.14 it can be seen mass percentage of anode CL components, in 3 specific areas, obtained with EDX analysis. In the areas close to membrane/anode interface (referred as Mw4 and Mw3) there is more Pt % but less C %, which means some Pt may have migrated into the interface, losing its activity. In Figure 4.22 it can be seen the CCL components mass percentage from the tests performed, obtained by EDX. It is seen that Stressor 1 and Stressor 3 have less Pt % than Stressor 2. According to SEM images in Appendix A.13 (Figures A.13.1 B), A.13.2 B) and A.13.3 B), it was seen more Pt agglomeration in Stressor 1 and Stressor 3, possibly as result of HT and low oxygen feed concentration.

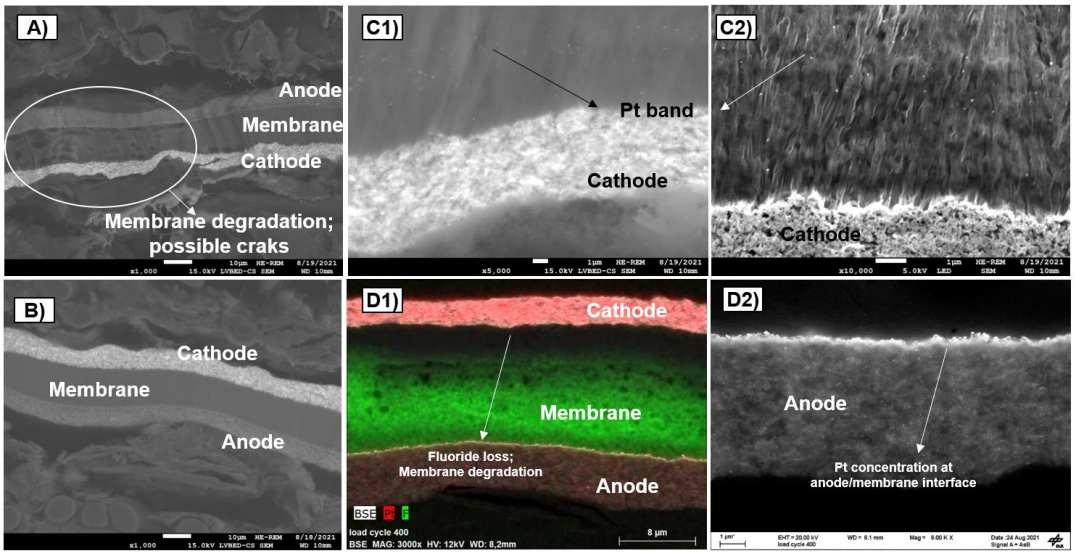

Figure 4.21 *– SEM images of cross sections of middle area aged CCM_1: A) Stressor 1; B) Stressor 2; C) Stressor 2; D) 17.7 % O_2 feed driving cycle. Samples corresponding to A), B) and C) were prepared with epoxy resin, and D) with ion cut method.*

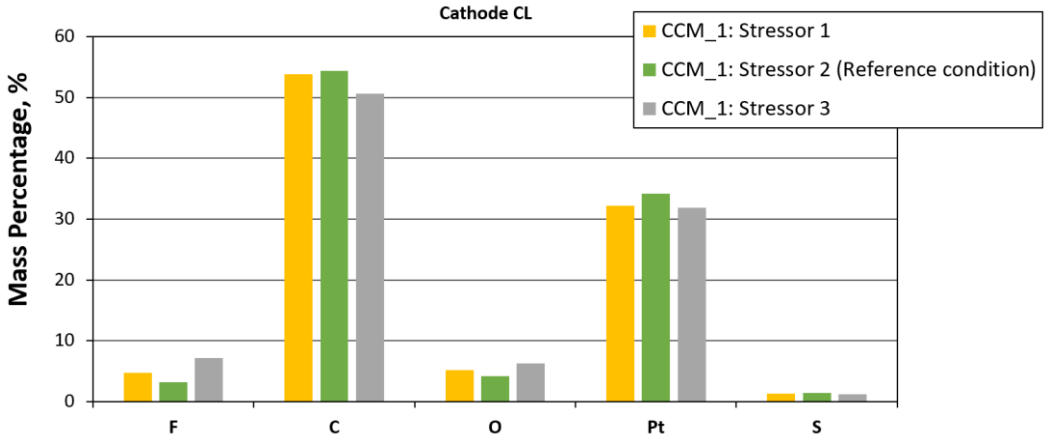

Figure 4.22 *– CCL components mass percentage, determined by EDX, by cross sections from middle CCM prepared by epoxy resin impregnation method.*

4.3.2 XPS analysis - stressor and driving cycle tests

To perform XPS analysis, the aged CCMs had to be detached from the GDL, which may have caused some irregularities in the measurements obtained. Some graphitic carbon from MPL may have passed for the CCM, causing an increase in the value detected in aged samples, when comparing with pristine CCM. From Figure 4.23, the driving cycle with 17.7 % O_2 feed concentration has less Pt %, comparing with stressor tests. However, XPS only detects elements on the surface of the CCM, and therefore, it can be speculated that the Pt was covered by ionomer, as there is a big increase in fluoride content, which can be due to a change in the electrode structure. It is also observed that Stressor 1, which was quite stressing for the fuel cell, presents less Pt % than Stressor 2 or Stressor 3. This is in accordance with the biggest ECSA reduction among stressor tests verified for Stressor 1, of 25 % (*cf*. Table 4.5). Stressor 1 might have had more Pt dissolution, comparing with other stressors. Regarding oxygen element, its oxidation state is unknown. It can be from the sulfonic groups, which explains the higher concentration of O_2 detected for pristine CCM. For CCM_2, Pt percentage did not change after 400 cycles, which allows to conclude CCM_2 presents more stable CCL comparing with CCM_1, under operating conditions imposed by driving cycle. However, CCM_2 Pt catalyst suffered oxidation after 400 cycles, as evidenced in Figure 4.24. Appendix A.15 shows XPS spectra corresponding to the data in Figure 4.23 and 4.24.

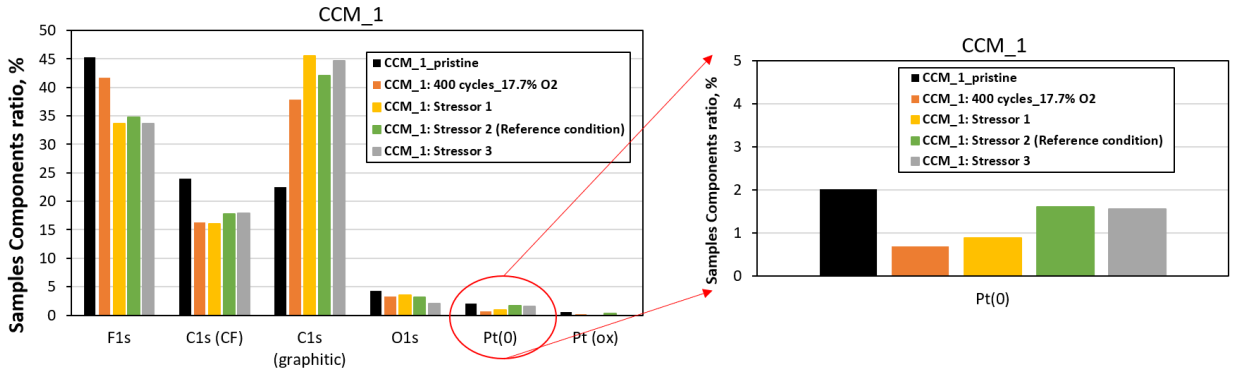

Figure 4.23 *- Bar chart of XPS analysis for CCM_1 pristine and aged samples from driving cycle and stressor tests.*

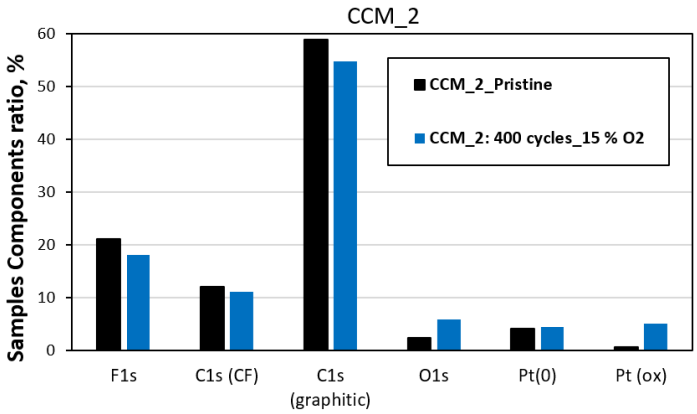

Figure 4.24 *- Bar chart of XPS analysis for CCM_2 pristine and aged sample from driving cycle.*

From the tests performed with CCM_1, both driving cycle and stressor tests, it was observed that the membrane and the CCL were the most affected components, degrading more. CCM_2, has proven to be more robust having more stable CCL.

5 Conclusion

Within this thesis, different operando stressors, derived from an automotive driving cycle, were performed using a differential cell with 12 cm^2 of active area. It was studied the effects of a lower oxygen feed concentration and a higher operating temperature on MEA degradation. A protocol was established, which included four stressor tests in total, that were labelled as Stressor 1, Stressor 2, Stressor 3, and Stressor 4, and are explained in the following.

Stressor 1, performed at higher temperature – 95 °C – and 21 % O_2 feed concentration, had the largest effect on MEA degradation. During the test, the membrane structure was compromised, as observed by SEM. The defect occurred mostly at the edge regions of the CCM, close to the gasket. Stressor 1 had the highest hydrogen crossover current (I_{H_2}) and the highest potential degradation rate, compared with the other stressors, which were 8.6 mA cm^{-2} and 0.93 mV h^{-1}, respectively. It was observed that operating at 95 °C was very critical to the CCM boundary with the gasket. To mitigate mechanical stress on CCM edge regions, a GDL size larger than the active area was selected, to overlap with the gasket. **Stressor 2**, consisting of lower operating temperature – 71 °C – and higher oxygen feed concentration –21 %, reference conditions, originated moderate degradation. **Stressor 3** and **Stressor 4** operated at low oxygen feed concentration, differed in the temperature: **Stressor 3** was operated at 71 °C and **Stressor 4** at 95 °C. It was clearly observed the increase in mass transport resistance, R_{MT}, for both tests, due to oxygen starvation. However, **Stressor 4** as it was operated at higher temperature, had the most significant increase in total impedance at 3 A cm^{-2}, being 117 mΩ cm^2. Through SEM analysis of Stressor 3, it was found a Pt band formation closer to the cathode side, that can possibly be attributed to reduced oxygen concentration. Furthermore, **Stressor 1** and **Stressor 3** presented Pt agglomeration in the cathode side, which was not so visible in reference condition. It was expected for **Stressor 4** to be the most critical for the MEA, among all stressors, leading to more degradation. However, increased GDL size led to a better performance of **Stressor 4**, comparing with **Stressor 1**.

Concerning the **driving cycle** tests performed with 17.7 % and 15 % of oxygen feed concentration, it was found that CCM_1 has reduced CCL stability, compared with CCM_2; CCM_2, on the other hand, is more prone of flooding. It was speculated that, for CCM_1, most of the degradation that was observed with SEM (localized CCL thinning due to possible carbon corrosion and Pt dissolution) occurred during the first 200 cycles of operation, which is consist with the big decrease in ECSA of 34 %, in the first 200 cycles of operation. It was also speculated that reduction in oxygen feed concentration in the driving cycle performed with CCM_1 can cause electrolyte thinning, originating electrical shorts between the electrodes. Another assumption presumed is that load cycling induces bigger ECSA reduction, as stressor tests performed with CCM_1 at a constant load do not have such a large decrease. This can be due to holding time at higher potentials that causes Pt dissolution and allowing for sufficient time for its diffusion towards cathode/membrane interface, or due to carbon corrosion that can cause Pt detachment.

6 Assessment of the work done

6.1 Objectives achieved

The main objectives of this work were achieved successfully. Main stressors from ID-FAST driving cycle were identified, and an AST protocol was defined to further analyse PEMFC degradation under specific operating conditions. *In-situ* and *ex-situ* characterization was performed, allowing to conclude that Stressor 1, with smaller GDL size, present very stressing conditions for the fuel cell. The study of two different commercial CCM under the same driving cycle was also carried out, which allowed to identify different potential degradation behaviours and different performances.

6.2 Future Work

Due to time limitation, Stressor 1 was only performed with GDL size of 3×4 cm^2. It was observed in this thesis that GDL size is a crucial parameter that influences PEMFC performance and that HT is critical for the CCM, in its boundary with the subgasket. Therefore, conducting Stressor 1 with GDL size of 3.6×4.9 cm^2 would allow to further study this effect and, at the same time, better assess and compare the isolated effects of the oxygen feed concentration reduction and temperature increase, on MEA degradation. Perform electrochemical characterization before and after the long stop will allow to study further reversible and irreversible potential losses. Regarding driving cycle tests, it was seen different potential degradation behaviours with CCM_1 and CCM_2. As the commercial CCMs are very different and not much information was provided, apart the loading and thickness of electrodes, studies regarding pore structure, Pt particle size distribution and ionomer distribution can be performed in the future, to better understand this behaviour. N_2 physisorption and mercury intrusion porosimetry measurements will allow to investigate pore structures of carbon support and pore size distribution; ionomer distribution can be investigated by TEM. Moreover, performing the driving cycle with CCM_1 at 15 % O_2 will allow to compare the results obtained with CCM_2, as the only changing variable will be the CCM used. At the same time, will allow to understand better oxygen concentration reduction effect on degradation.

6.3 Final assessment

Working in a DLR was a great opportunity, that allowed me to gain valuable knowledge in electrochemistry area, particularly fuel cells. Durability is a major problem hindering PEMFC commercialization and, by understanding the main degradation mechanisms, it may be improved. AST facilitate rapid degradation and failure of specific MEA components, such as membrane, electrocatalyst and catalyst support. This seven months at DLR provided the author an excellent insight on some AST and characterization techniques (*ex-situ* and *in-situ*) used to assess PEMFC performance and degradation, under stressing operating conditions.

7 References

[1] A. El-kharouf, "Understanding GDL properties and performance in polymer electrolyte fuel cells - PhD Thesis," University of Birmingham, 2014.

[2] "European Comission." [Online]. Available: https://ec.europa.eu/info/strategy/priorities-2019-2024/european-green-deal/transport-and-green-deal_en. [Accessed: 13-Sep-2021].

[3] P. Gazdzick, J. Mitzel, D. Garcia Sanchez, M. Schulze, and K. A. Friedrich, "Evaluation of reversible and irreversible degradation rates of polymer electrolyte membrane fuel cells tested in automotive conditions," *J. Power Sources*, vol. 327, pp. 86–95, 2016.

[4] A. Jayakumar, S. P. Sethu, M. Ramos, J. Robertson, and A. Al-Jumaily, "A technical review on gas diffusion, mechanism and medium of PEM fuel cell," *Ionics (Kiel).*, vol. 21, no. 1, pp. 1–18, 2015.

[5] K. Talukdar, "Development and Characterization of Low Pt-Loaded Membrane Electrode Assemblies with Focus on Performance and Durability - PhD Thesis," Universität Stuttgart Institut, 2020.

[6] R. Balzarotti, S. Latorrata, M. Mariani, P. G. Stampino, and G. Dotelli, "Optimization of perfluoropolyether-based gas diffusion media preparation for PEM fuel cells," *Energies*, vol. 13, no. 7, 2020.

[7] M. Pan, C. Pan, C. Li, and J. Zhao, "A review of membranes in proton exchange membrane fuel cells: Transport phenomena, performance and durability," *Renew. Sustain. Energy Rev.*, vol. 141, no. January, p. 110771, 2021.

[8] E. Zakrisson, "The Effect of Start / Stop Strategy on PEM Fuel Cell Degradation Characteristics-Master Thesis," Chalmers University of Technology, 2011.

[9] Z. Hou, R. Wang, K. Wang, W. Shi, D. Xing, and H. Jiang, "Failure mode investigation of fuel cell for vehicle application," *Front. Energy*, vol. 11, no. 3, pp. 318–325, 2017.

[10] J. Wu *et al.*, "A review of PEM fuel cell durability: Degradation mechanisms and mitigation strategies," *J. Power Sources*, vol. 184, no. 1, pp. 104–119, 2008.

[11] J. N. Schwämmlein, P. J. Rheinländer, Y. Chen, K. T. Freyer, and H. A. Gasteiger, " Anode Aging during PEMFC Start-Up and Shut-Down: H 2 -Air Fronts vs Voltage Cycles ," *J. Electrochem. Soc.*, vol. 165, no. 16, pp. F1312–F1322, 2018.

[12] Y. Wang, B. Seo, B. Wang, N. Zamel, K. Jiao, and X. C. Adroher, "Fundamentals, materials, and machine learning of polymer electrolyte membrane fuel cell technology," *Energy AI*, vol. 1, p. 100014, 2020.

[13] G. S. Harzer, "Boosting High Current Density Performance of Durable, Low Pt-Loaded PEM Fuel Cells - PhD Thesis," Technischen Universität München, 2018.

[14] R. L. Borup *et al.*, "Recent developments in catalyst-related PEM fuel cell durability," *Curr. Opin. Electrochem.*, vol. 21, pp. 192–200, 2020.

[15] A. Kongkanand, W. Gu, and M. F. Mathias, "Proton-Exchange Membrane Fuel cells with low-Pt content," *Fuel Cells Hydrog. Prod.*, 2019.

[16] Y. Park, H. Tokiwa, K. Kakinuma, M. Watanabe, and M. Uchida, "Effects of carbon supports on Pt distribution , ionomer coverage and cathode performance for polymer electrolyte fuel cells," *J. Power Sources*, vol. 315, pp. 179–191, 2016.

[17] D. A. Cullen, K. C. Neyerlin, R. K. Ahluwalia, B. Rangachary, and A. Kusoglu, "New roads and challemges for fuel cells in heavy-duty transportation," *Nat. energy*, vol. 6, pp. 462–474, 2021.

[18] S. Helmly, M. J. Eslamibidgoli, K. A. Friedrich, and M. H. Eikerling, "Local Impact of Pt Nanodeposits on Ionomer Decomposition in Polymer Electrolyte Membranes," *Electrocatalysis*, vol. 8, no. 6, pp. 501–508, 2017.

[19] P. Gazdzicki, J. Mitzel, A. M. Dreizler, M. Schulze, and K. A. Friedrich, "Impact of Platinum Loading on Performance and Degradation of Polymer Electrolyte Fuel Cell Electrodes Studied in a Rainbow Stack," *Fuel Cells*, vol. 18, no. 3, pp. 270–278, 2018.

[20] "FCH-JU Durability targets." [Online]. Available: https://www.fch.europa.eu/soa-and-targets. [Accessed: 15-Sep-2021].

[21] F. Ettingshausen, J. Kleemann, A. Marcu, G. Toth, H. Fuess, and C. Roth, "Dissolution and migration of platinum in PEMFCs investigated for start/stop cycling and high potential degradation," *Fuel Cells*, vol. 11, no. 2, pp. 238–245, 2011.

[22] W. Bi, Q. Sun, Y. Deng, and T. F. Fuller, "The effect of humidity and oxygen partial pressure

on degradation of Pt/C catalyst in PEM fuel cell," *Electrochim. Acta*, vol. 54, no. 6, pp. 1826–1833, 2009.
[23] Z. H. Wan *et al.*, "Determination of oxygen transport resistance in gas diffusion layer for polymer electrolyte fuel cells," *Int. J. Energy Res.*, vol. 42, no. 6, pp. 2225–2233, 2018.
[24] R. Lin, X. Cui, J. Shan, L. Técher, F. Xiong, and Q. Zhang, "Investigating the effect of start-up and shut-down cycles on the performance of the proton exchange membrane fuel cell by segmented cell technology," *Int. J. Hydrogen Energy*, vol. 40, no. 43, pp. 14952–14962, 2015.
[25] "ID-FAST." [Online]. Available: http://id-fast.eu/index.php?id=22. [Accessed: 04-May-2021].
[26] F. Wilhelm *et al.*, "ID-FAST - Investigations on degradation mechanisms and Definition of protocols for PEM Fuel cells Accelerated Stress Testing; Grant agreement no : 779565; Call : H2020-JTI-FCH-2017-1; D4 . 3 – Analysis of coupling between mechanisms and definition of comb," 2021.
[27] "DLR." [Online]. Available: https://www.dlr.de/DE/Home/home_node.html. [Accessed: 04-May-2021].
[28] L. Kim, C. G. Chung, Y. W. Sung, and J. S. Chung, "Dissolution and migration of platinum after long-term operation of a polymer electrolyte fuel cell under various conditions," *J. Power Sources*, vol. 183, no. 2, pp. 524–532, 2008.
[29] L. Carrette, K. A. Friedrich, and U. Stimming, "Fuel Cells - Fundamentals and Applications," *Fuel Cells*, vol. 1, no. 1, pp. 5–39, 2001.
[30] N. A. Hanna Rosli *et al.*, "Review of chitosan-based polymers as proton exchange membranes and roles of chitosan- supported ionic liquids," *Int. J. Mol. Sci.*, vol. 21, no. 2, pp. 1–53, 2020.
[31] T. B. Caston, "Design of a gas diffusion layer for a polymer electrolyte membrane fuel cell with a graduated resistance to flow - Master thesis," Georgia Institute of Technology, 2010.
[32] "Fumatech." [Online]. Available: https://www.fumatech.com/EN/Membranes/Fuel-cells/index.html.
[33] T. Mashio, A. Ohma, S. Yamamoto, and K. Shinohara, "Analysis of reactant gas transport phenomena en catalyst layer," *ECS Trans.*, vol. 11, no. 1, pp. 529–540, 2007.
[34] M. Schoemaker, U. Misz, P. Beckhaus, and A. Heinzel, "Evaluation of hydrogen crossover through fuel cell membranes," *Fuel Cells*, vol. 14, no. 3, pp. 412–415, 2014.
[35] Kevin .R. Cooper, "In Situ PEMFC Fuel Crossover & Electrical Short Circuit Measurement," *Fuel Cell Mag.*, pp. 1–2, 2008.
[36] M. Prokop *et al.*, "Degradation kinetics of Pt during high-temperature PEM fuel cell operation Part III: Voltage-dependent Pt degradation rate in single-cell experiments," *Electrochim. Acta*, vol. 363, p. 137165, 2020.
[37] K. More, R. Borup, and K. Reeves, "Identifying Contributing Degradation Phenomena in PEM Fuel Cell Membrane Electride Assemblies Via Electron Microscopy," *ECS Trans.*, vol. 3, no. 1, pp. 717–733, 2019.
[38] J. Sousa, "Investigation of in-situ test protocols for accelerated aging of gas diffusion media of PEM fuel cells- Master thesis," Faculty of engineering of porto university, 2019.
[39] A. Kneer, "The Effect of Voltage Cycling on Catalyst Degradation in Automotive PEM Fuel Cells - PhD Thesis," Fakultät für Naturwissenschaften der Universität Ulm, 2018.
[40] G. S. Harzer, J. N. Schwämmlein, A. M. Damjanović, S. Ghosh, and H. A. Gasteiger, "Cathode Loading Impact on Voltage Cycling Induced PEMFC Degradation: A Voltage Loss Analysis," *J. Electrochem. Soc.*, vol. 165, no. 6, pp. F3118–F3131, 2018.
[41] F. B. Spingler, A. Phillips, T. Schuler, M. C. Tucker, and A. Z. Weber, "Investigating fuel-cell transport limitations using hydrogen limiting current," *Int. J. Hydrogen Energy*, vol. 42, no. 19, pp. 13960–13969, 2017.
[42] A. Sorrentino, K. Sundmacher, and T. Vidakovic-Koch, "Polymer electrolyte fuel cell degradation mechanisms and their diagnosis by frequency response analysis methods: A review," *Energies*, vol. 13, no. 21, 2020.
[43] N. Dyantyi, A. Parsons, C. Sita, and S. Pasupathi, "PEMFC for aeronautic applications: A review on the durability aspects," *Open Eng.*, vol. 7, no. 1, pp. 287–302, 2017.
[44] Y. C. Park, K. Kakinuma, M. Uchida, H. Uchida, and M. Watanabe, "Deleterious effects of interim cyclic voltammetry on Pt/carbon black catalyst degradation during start-up/shutdown cycling evaluation," *Electrochim. Acta*, vol. 123, pp. 84–92, 2014.
[45] Y. Kakizawa, C. L. Schreiber, S. Takamuku, M. Uchida, A. Iiyama, and J. Inukai, "Visualization of the oxygen partial pressure in a proton exchange membrane fuel cell during cell operation

with low oxygen concentrations," *J. Power Sources*, vol. 483, no. October 2020, p. 229193, 2021.

[46] N. Linse, G. G. Scherer, A. Wokaun, and L. Gubler, "Quantitative analysis of carbon corrosion during fuel cell start-up and shut-down by anode purging," *J. Power Sources*, vol. 219, pp. 240–248, 2012.

[47] U. Groos, Z. Mario, and A. Casalegno, "ID-FAST - Investigations on degradation mechanisms and Definition of protocols for PEM Fuel cells Accelerated Stress Testing; Grant agreement no : 779565; Call : H2020-JTI-FCH-2017-1; D4.1: Definition of new reference single cell hardware (M8)," 2019.

[48] G. Tsotridis, A. Pilenga, G. De Marco, and T. Malkow, *EU Harmonised Test Protocols for PEMFC MEA Testing in Single Cell Configuration for Automotive Applications; JRC Science for Policy report*. 2015.

[49] P. Pei, Z. Wu, Y. Li, X. Jia, D. Chen, and S. Huang, "Improved methods to measure hydrogen crossover current in proton exchange membrane fuel cell," *Appl. Energy*, vol. 215, no. August 2017, pp. 338–347, 2018.

[50] K. R. Cooper, "in Situ Pem Fuel Cell Electrochemical Surface Area and Catalyst Utilization Measurement," *Fuel Cell Mag.*, pp. 1–3, 2009.

[51] S. Touhami, J. Mainka, J. Dillet, S. A. H. Taleb, and O. Lottin, "Transmission Line Impedance Models Considering Oxygen Transport Limitations in Polymer Electrolyte Membrane Fuel Cells," *J. Electrochem. Soc.*, vol. 166, no. 15, pp. F1209–F1217, 2019.

[52] K. O. Kjellsen, A. Monsøy, K. Isachsen, and R. J. Detwiler, "Preparation of flat-polished specimens for SEM-backscattered electron imaging and X-ray microanalysis—importance of epoxy impregnation," *Cem. Concr. Res.*, vol. 33, pp. 611–616, 2003.

[53] Q. Zhang, M. Schulze, P. Gazdzicki, and K. A. Friedrich, "Comparison of different performance recovery procedures for polymer electrolyte membrane fuel cells," *Appl. Energy*, vol. 302, no. July, p. 117490, 2021.

[54] M. Uchida *et al.*, "Effect of the state of distribution of supported Pt nanoparticles on effective Pt utilization in polymer electrolyte fuel cells," *Phys. Chem. Chem. Phys.*, vol. 15, no. 27, pp. 11236–11247, 2013.

[55] N. Wagner, *Electrochemical impedance spectroscopy*, no. 49572. 2011.

[56] I. Pivac, G. Radica, F. Barbir, D. Benouioua, F. Harel, and D. Candusso, "Giantleap Deliverable D1.4: Diagnostic methods for automotive fuel cell systems," 2017.

[57] S. Delgado, "Drying Techniques for Polymer Electrolyte Membrane Fuel Cell Electrodes - Master ' s dissertation," FEUP, 2018.

[58] C. Lim, "IV . Transport Phenomena Lecture 20 : Warburg Impedance," *MIT OpenCourseWare*, pp. 1–7, 1899.

Annex

A.i Ionic conductivity resistance determination

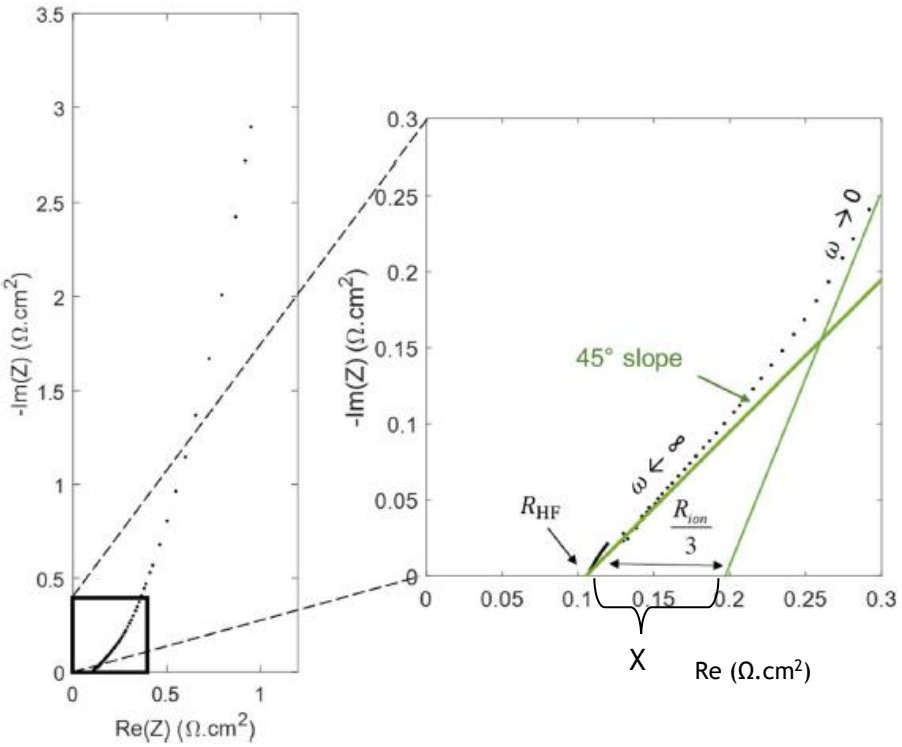

Figure A.i – Example of experimental impedance spectra in Nyquist diagram for ionic resistance determination, extracted from [51].

Appendix

A.1 DLR testbench and software interface control

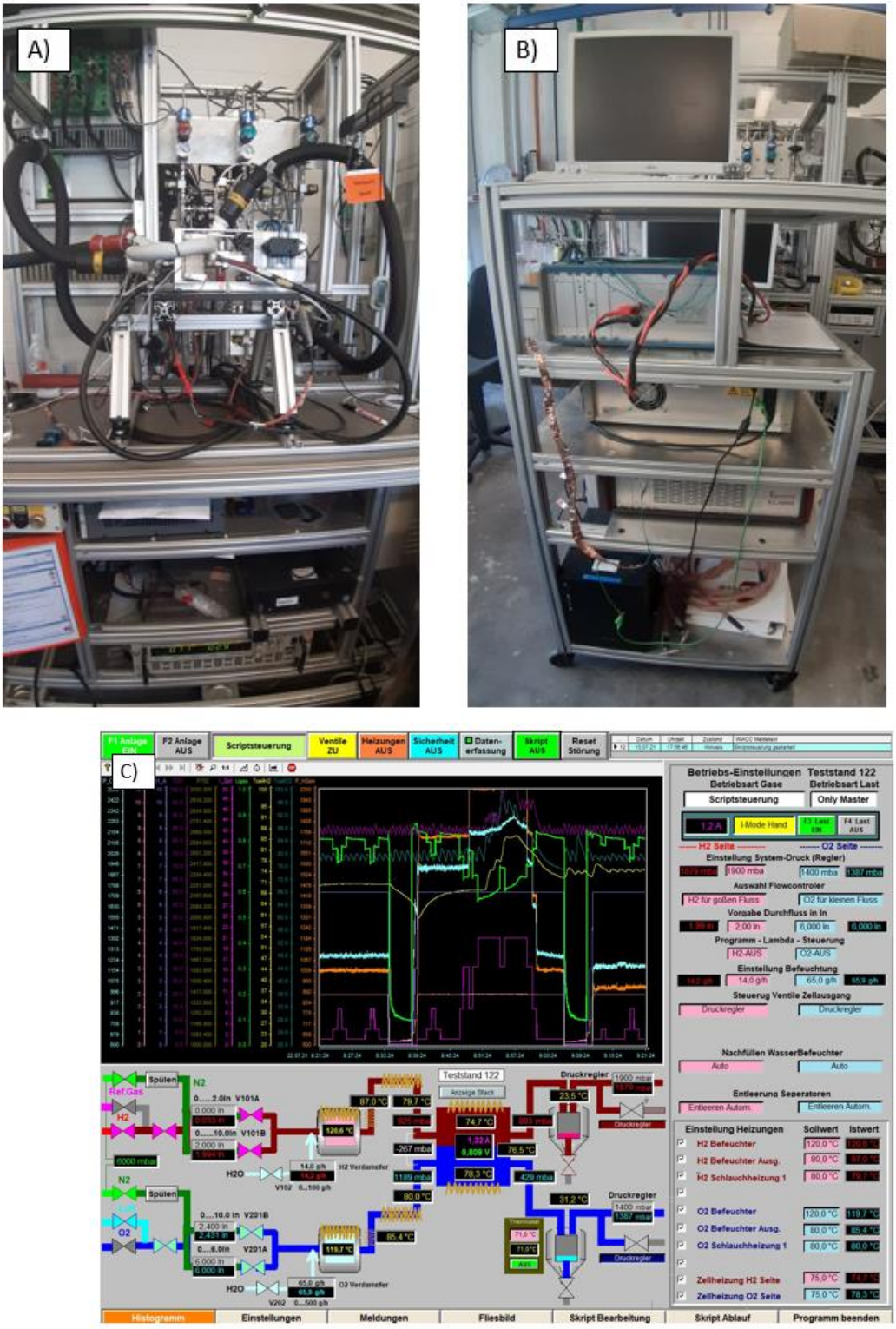

Figure A.1.1 – A) Test bench, B) potentiostat, and C) control interface (SIMATIC WinCC software) used for the experiments performed for this thesis.

A.2 Driving cycle operating conditions for 15 % O_2 concentration

Table A.2.1 – Load steps and operating conditions specifications for 15 % oxygen concentration, for ID-FAST driving cycle. Step 1 and step 27, coloured with yellow, correspond to short stop (SS). RH was always kept as 59 % (cathode) and 7 1% (anode).

Step	Dwell Time (s)	Current (A)	H_2 flow ($L \cdot min^{-1}$)	O_2 flow ($L \cdot min^{-1}$)	N_2 flow ($L \cdot min^{-1}$)	Anode pressure (mbar)	Cathode pressure (mbar)	Cell Temp. (° C)	Water anode ($g \cdot h^{-1}$)	Water cathode ($g \cdot h^{-1}$)
1	240	0	0.2	0	0	1000	1000	73	0	0
2	30	0	0.5	1	0.5	1900	1400	71	5	10
3	30	0	1	3	0.5	1900	1400	71	10	20
4	90	1.2	2	6	2.4	1900	1400	71	14	65
5	50	3	2	6	2.4	1900	1400	71	14	65
6	200	1.2	2	6	2.4	1900	1400	71	14	65
7	55	3	2	6	2.4	1900	1400	71	14	65
8	40	7.1	2	6	2.4	1900	1400	71	14	65
9	50	3	2	6	2.4	1900	1400	71	14	65
10	200	1.2	2	6	2.4	1900	1400	71	14	65
11	50	3	2	6	2.4	1900	1400	71	14	65
12	40	7.1	2	6	2.4	1900	1400	71	14	65
13	55	3	2	6	2.4	1900	1400	71	14	65
14	200	1.2	2	6	2.4	2000	1520	71	13	59
15	50	3	2	6	2.4	2000	1520	71	13	59
16	40	7.1	2	6	2.4	2000	1520	71	13	59
17	50	3	2	6	2.4	2000	1520	71	13	59
18	205	1.2	2	6	2.4	2000	1520	71	13	59
19	50	3	2	6	2.4	2000	1520	71	13	59
20	40	7.1	2	6	2.4	2000	1520	71	13	59
21	50	3	2	6	2.4	2000	1520	71	13	59
22	200	1.2	2	6	2.4	2000	1520	71	13	59
23	55	3	2	6	2.4	2000	1520	71	13	59
24	40	7.1	2	6	2.4	2000	1520	71	13	59
25	50	3	2	6	2.4	2000	1520	71	13	59
26	100	1.2	2	6	2.4	2000	1520	71	13	59
27	240	0	0.2	0	0	1000	1000	71	0	0
28	30	0	0.5	1	0.5	2500	2100	71	5	10
29	30	0	1	3	0.5	2750	2480	71	9	20
30	100	1.2	2	6	2.4	2750	2480	71	9	34
31	50	3	2	6	2.4	2750	2480	71	9	34
32	40	7.1	2	6	2.4	2750	2480	71	9	34
33	55	3	2	6	2.4	2750	2480	71	9	34
34	200	1.2	2	6	2.4	2750	2480	71	9	34
35	40	7.1	2	6	2.4	2750	2480	71	9	34
36	55	15.3	2	6	2.4	2750	2480	71	9	34
37	40	7.1	2	6	2.4	3000	2800	71	8	30
38	55	15.3	2	6	2.4	3000	2800	71	8	30
39	70	21	2	6	2.4	3000	2800	75	8	30
40	80	21	2	6	2.4	3000	2800	79	12	43
41	80	21	2	6	2.4	3000	2800	83	12	43
42	55	15.3	2	6	2.4	3000	2800	86	16	60
43	100	21	2	6	2.4	3000	2800	90	20	72
44	100	21	2	6	2.4	3000	2800	80	12	45
45	30	21	2	6	2.4	3000	2800	77	12	45
46	60	15.3	2	6	2.4	2750	2480	76	11	43
47	40	7.1	2	6	2.4	2400	2100	75	11	43
48	290	1.2	2	6	2.4	2000	1520	71	13	59

A.3 Baltic fuel cell: flow field and GDL size representation

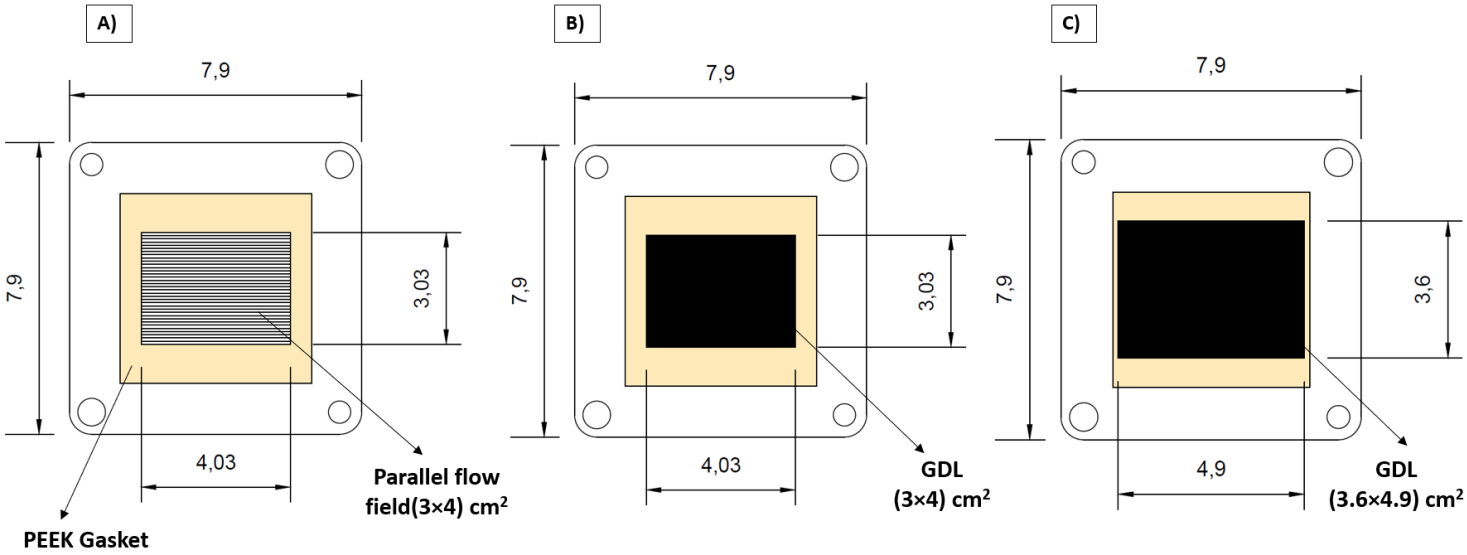

Figure A.3.1 – Representation of A) fuel cell active area, used in stressor and driving cycle tests, with parallel flow field design; B) GDL size (3×4 cm²) used in Stressor 1, Stressor 2 and driving cycle tests with 15 % and 17.7 % O_2 feed concentration; C) GDL size (3.6×4.9 cm²) used in Stressor 3 and Stressor 4 tests.

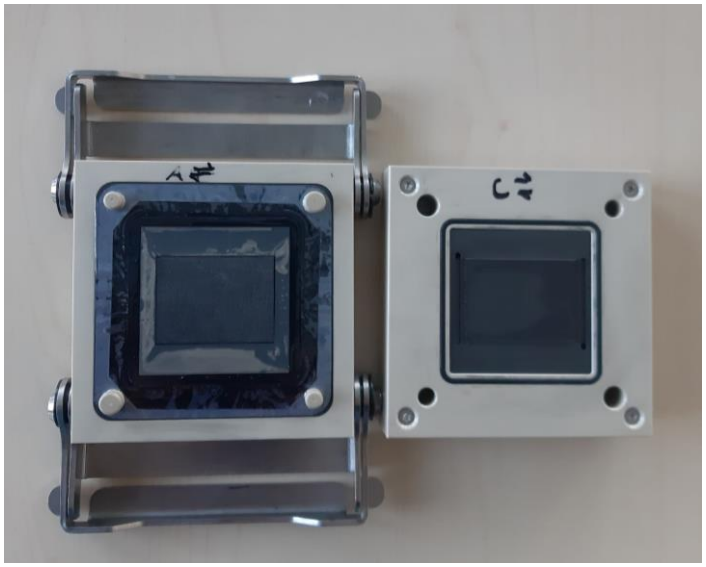

Figure A.3.2 – Zero gradient Baltic fuel cell used in stressor and driving cycle tests, (with MEA).

A.4 Driving cycle potential evolution with operation time

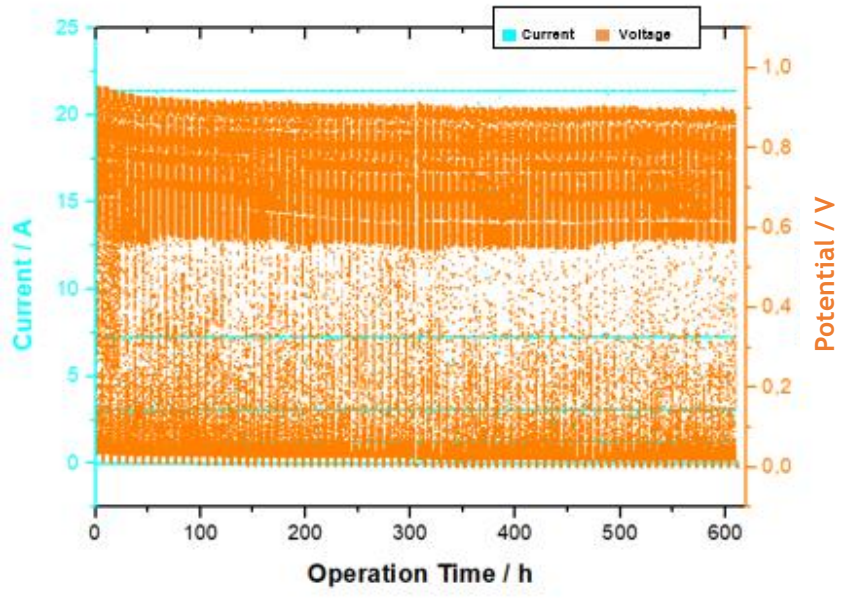

Figure A.4.1 – Potential evolution with operation time for 17.7 % O_2 feed concentration driving cycle, with CCM_1 (400 cycles).

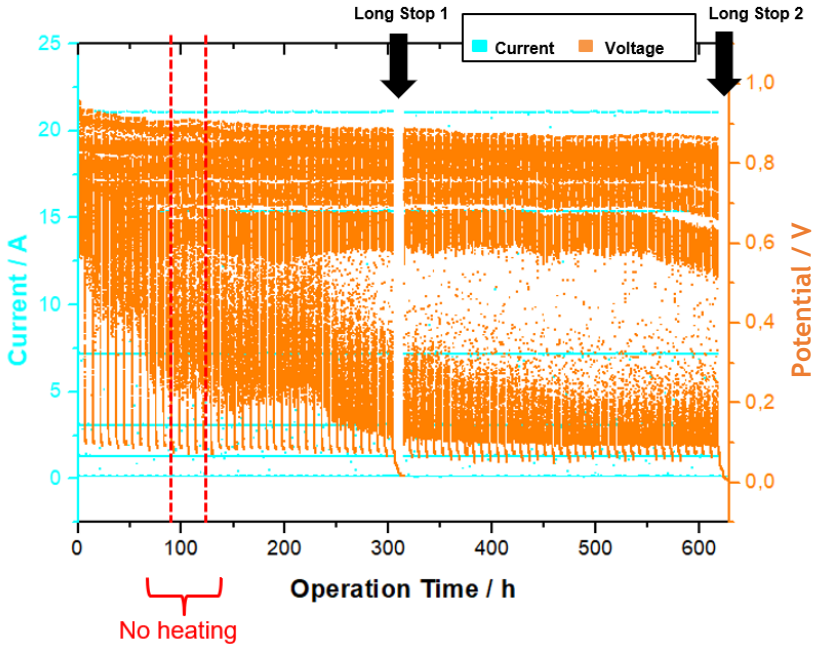

Figure A.4.2 – Potential evolution with operation time for 15 % O_2 feed concentration driving cycle, with CCM_ 2 (400 cycles). There was no heating from 90 till 127 h of operation.

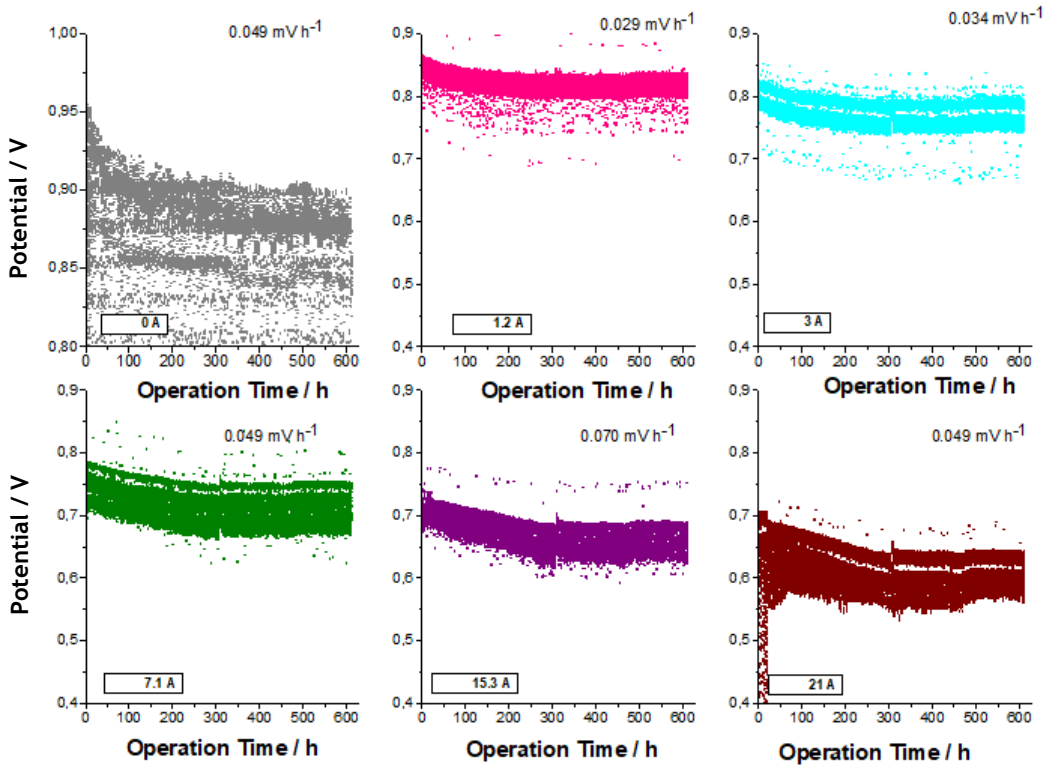

Figure A.4.3 - Potential evolution with operation time, for specific currents, for 17.7 % O2 feed concentration driving cycle, with CCM_1 (400 cycles).

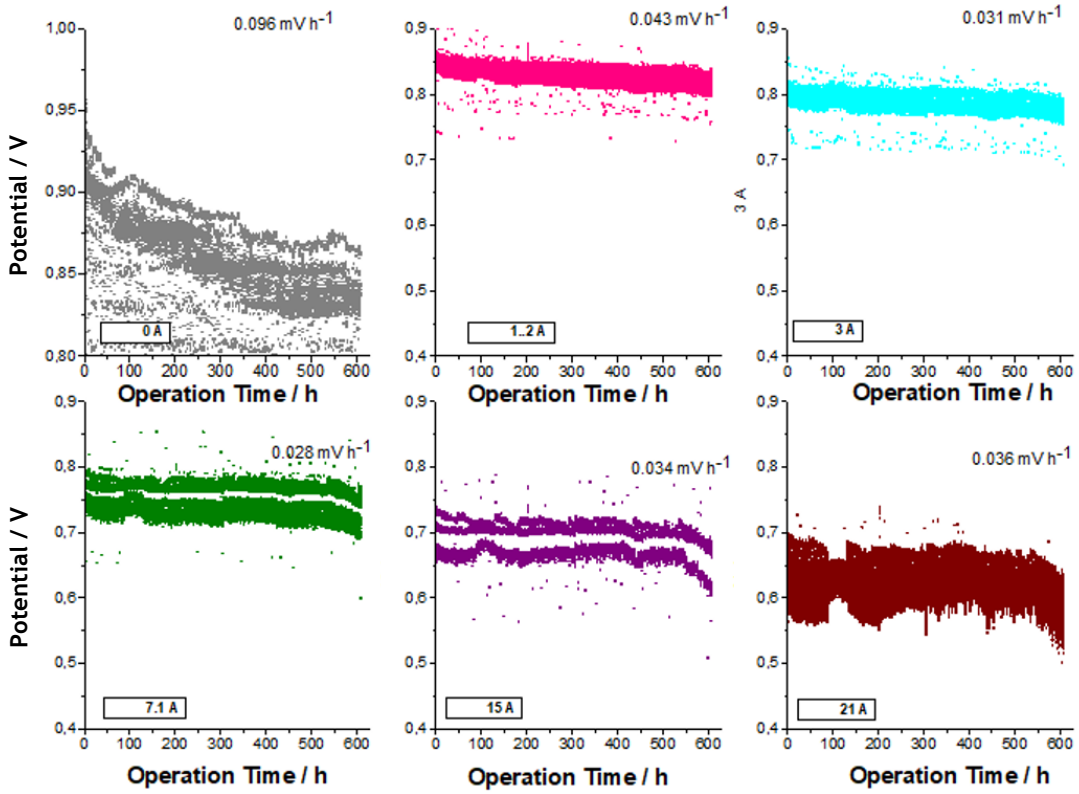

Figure A.4.4 - Potential evolution with operation time, for specific current densities, for 15 % O_2 feed concentration driving cycle, with CCM_2 (400 cycles). There was no heating from 90 till 127 h of operation, which led to potential oscillation.

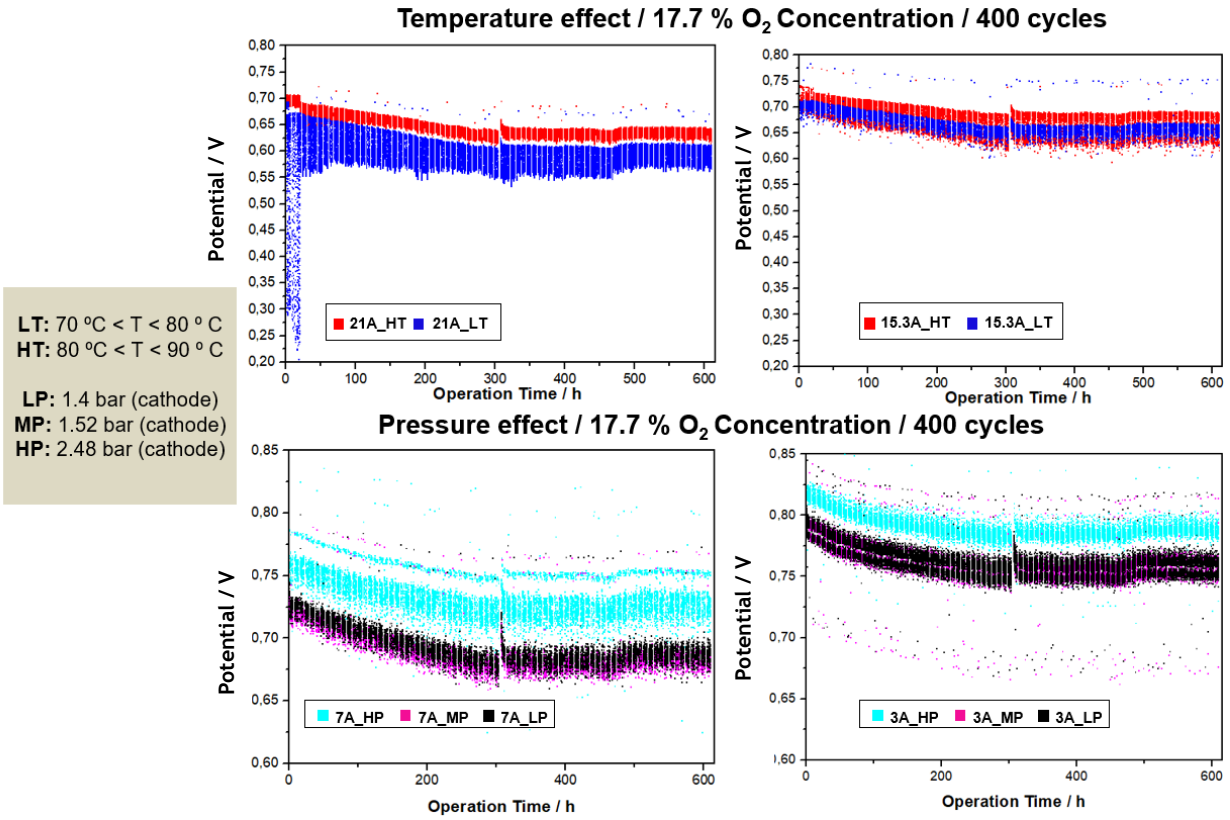

Figure A.4.5 – Potential evolution with operation time, for specific operation conditions (temperature and pressure) for 17.7 % O_2 feed concentration driving cycle, with CCM_1 (400 cycles).

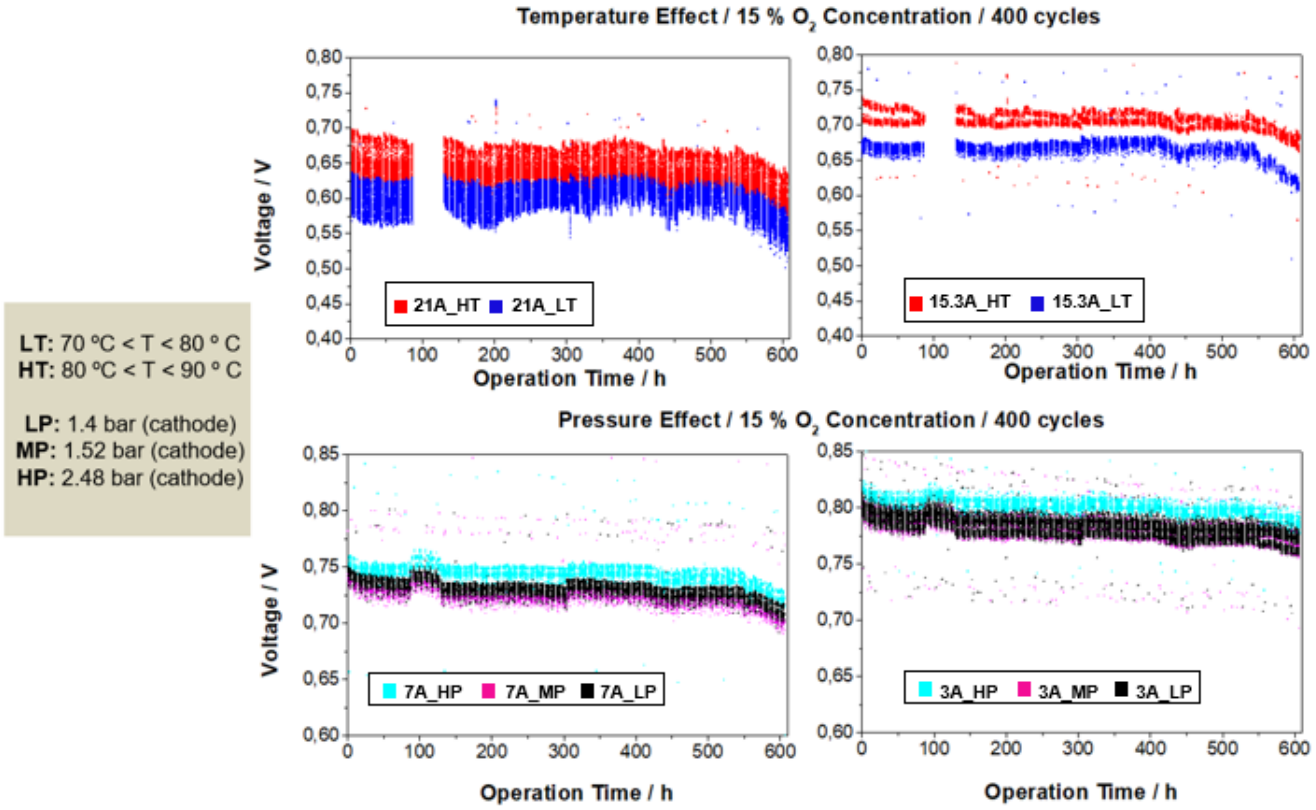

Figure A.4.6 – Potential evolution with operation time, for specific operation conditions (temperature and pressure) for 15 % O_2 feed concentration driving cycle, with CCM_2 (400 cycles). There was no heating from 90 till 127 h of operation, in which can be seen potential oscillation.

A.5 Electrochemical characterization for driving cycle tests

Electrochemical Impedance Spectroscopy (EIS)

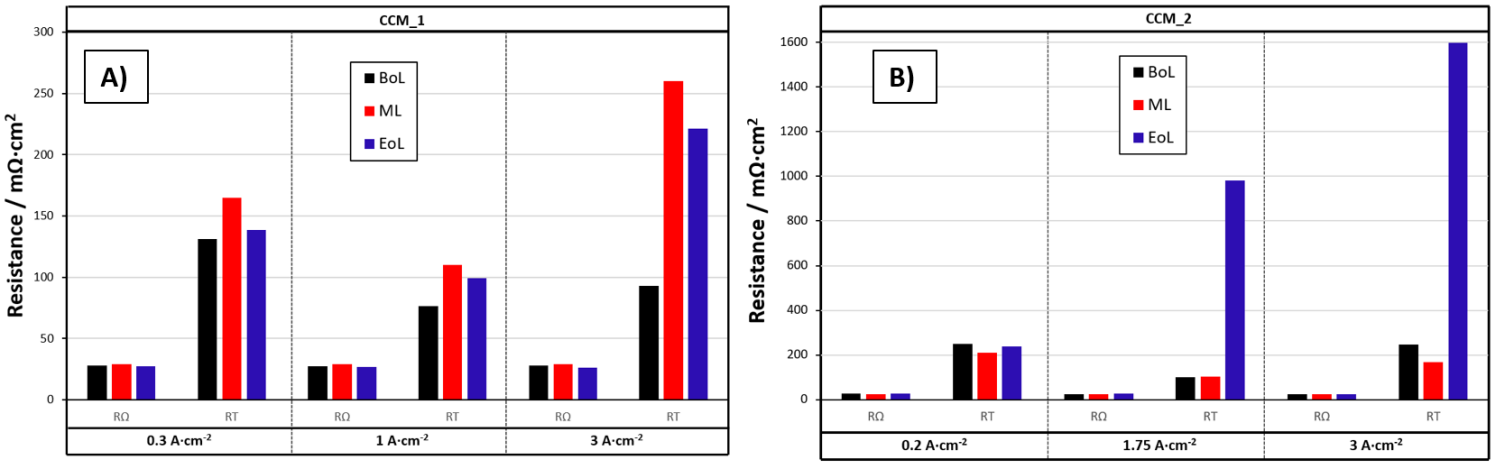

Figure A.5.1 - Ohmic Resistance ($R_Ω$) and total resistance (R_T) representation, for A) 17.7 % O_2 feed concentration with CCM_1 and B)15 % O_2 feed concentration with CCM_2, for BoL, ML, and EoL characterization.

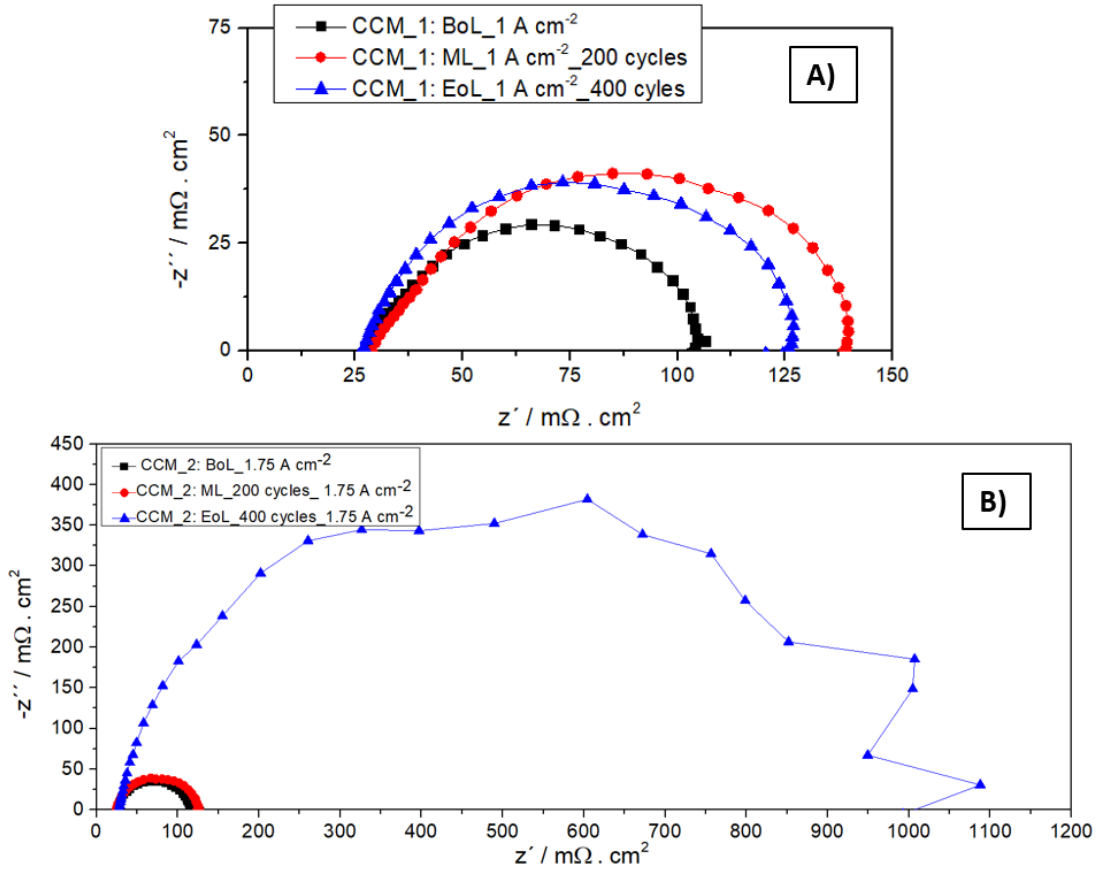

Figure A.5.2 - EIS performed for driving cycle test with A) 17.7 % O_2 feed concentration (CCM_1); B) 15 % O_2 feed concentration (CCM_2), for BoL, ML, and EoL characterization, for 500 mA amplitude and 1 A·cm^{-2} and 1.75 A·cm^{-2}, respectively.

Cyclic Voltammetry (CV)

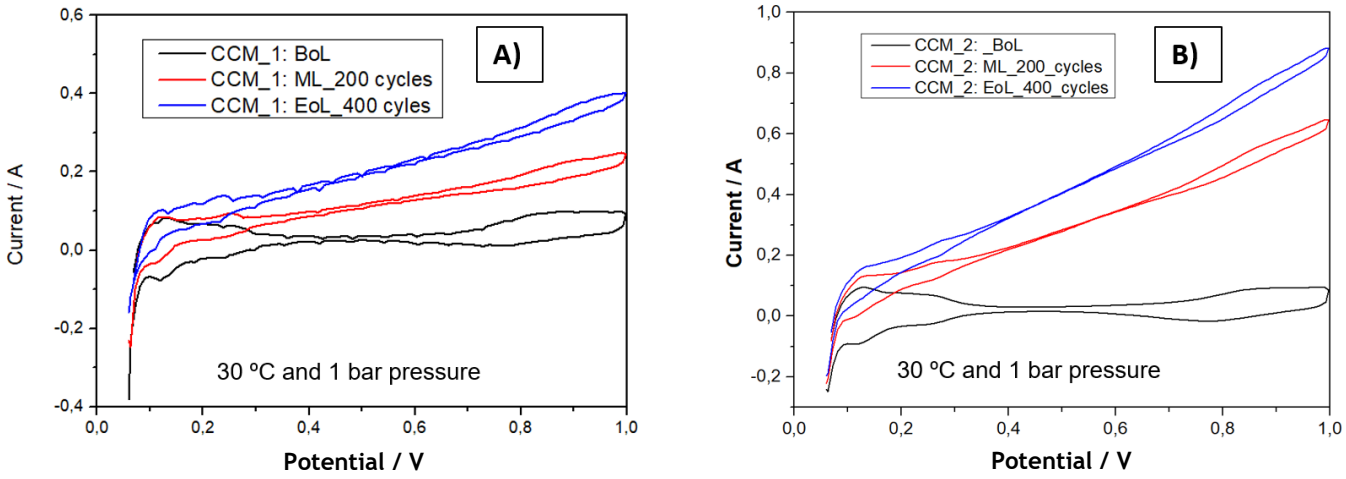

Figure A.5.3 – CV performed for for A) 17.7 % O_2 feed concentration (CCM_1) and B)15 % O_2 feed concentration (CCM_2), for BoL, ML, and EoL characterization, at ambient temperature and pressure.

Ionic Conductivity Resistance (ICR)

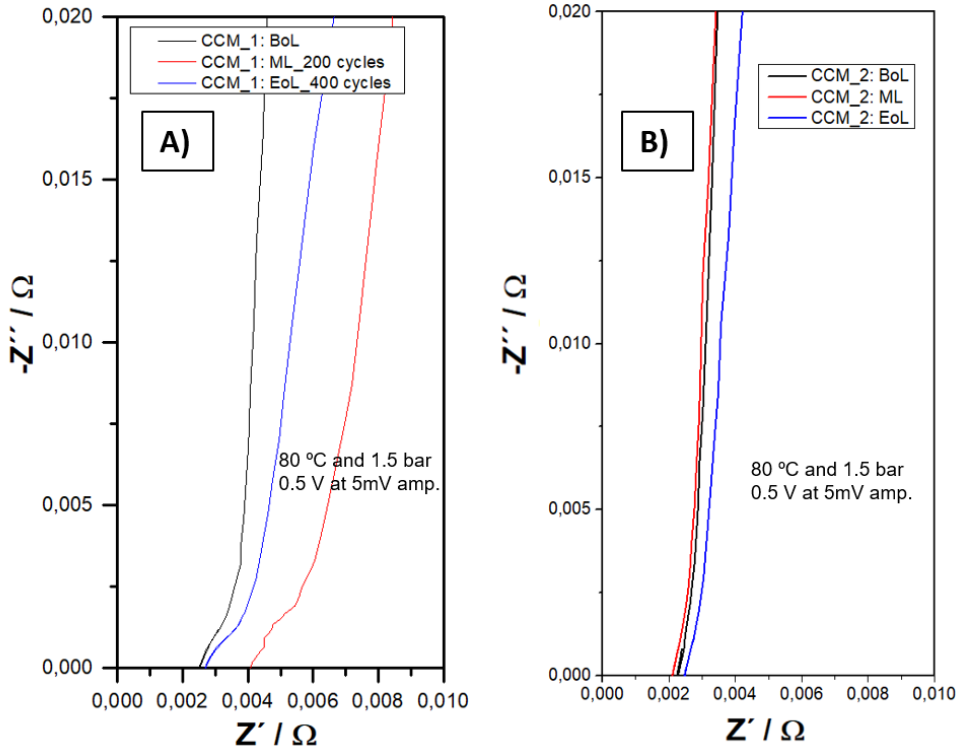

Figure A.5.4 – ICR test performed for: A) 17.7 % O_2 feed concentration, with CCM_1; B)15 % O_2 feed concentration, with CCM_2, at 80 ºC and 1.5 bar outlet pressure (cathode and anode), at 5 mV amplitude and 0.5 V, for BoL, ML, and EoL characterization.

Linear Sweep Voltammetry (LSV)

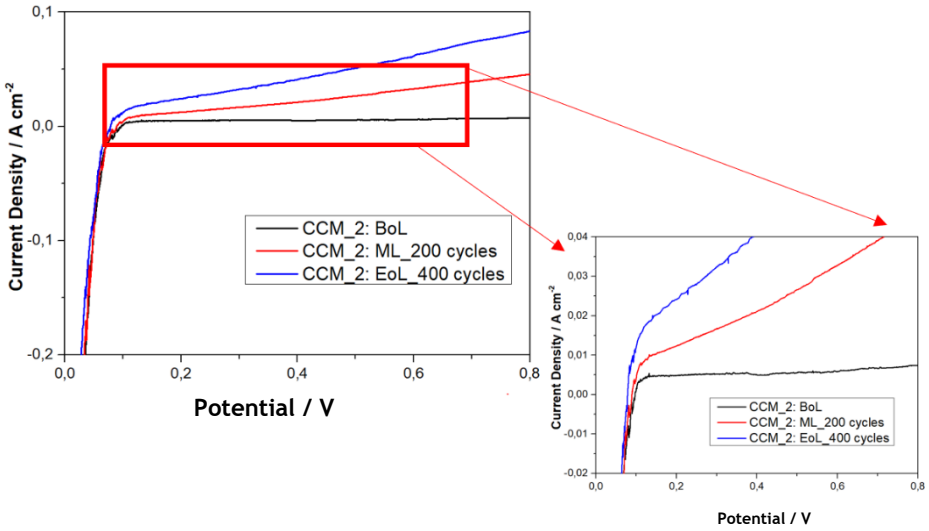

Figure A.5.5 – LSV test performed for 15 % O_2 feed concentration, with CCM_2, at 80 ºC and 1.5 bar (outlet pressure), for BoL, ML, and EoL characterization.

A.6 *Aged MEAs from stressor tests*

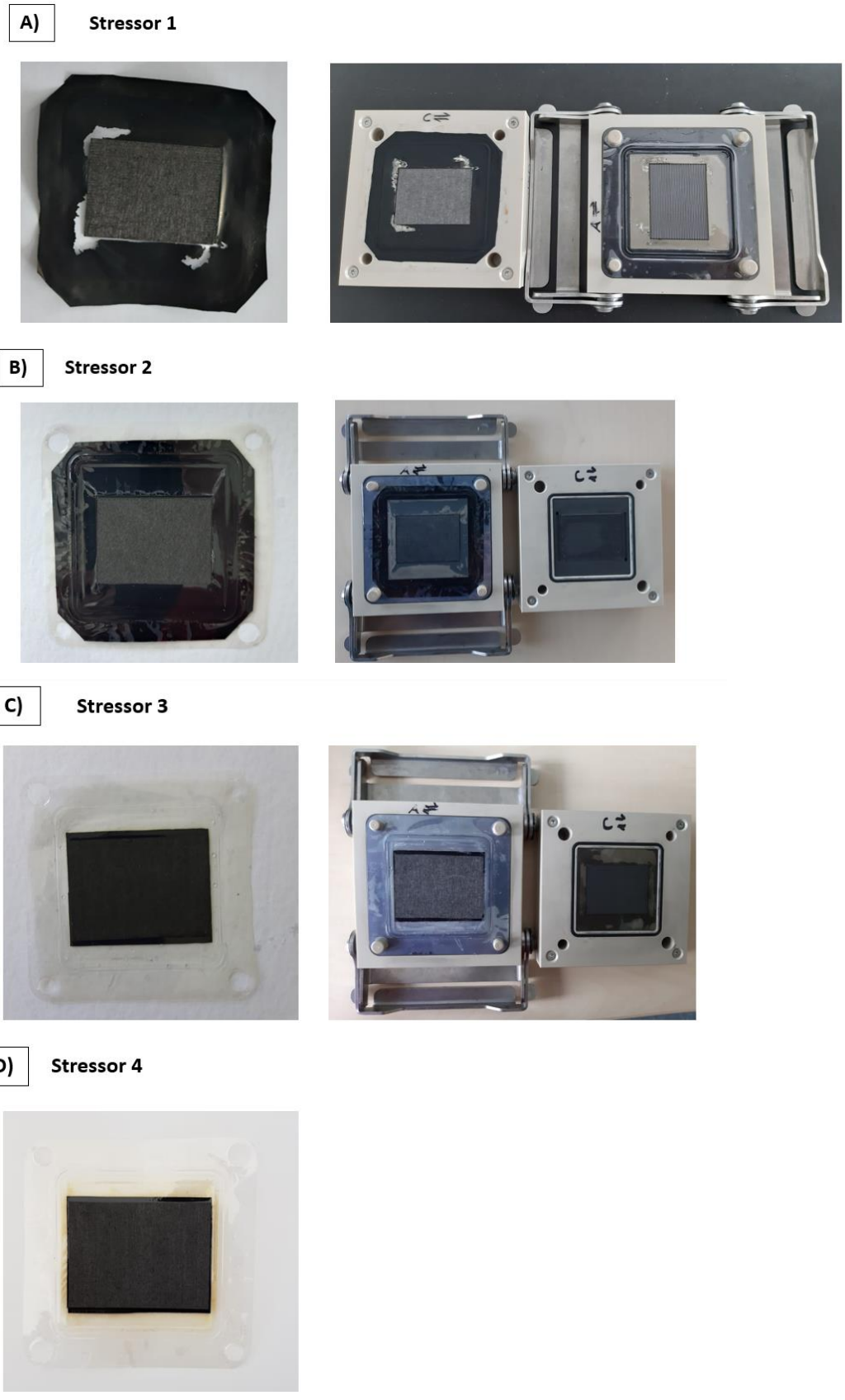

Figure A.6.1 – Aged MEAs at the EoL, for A) Stressor 1, B) Stressor 2, C) Stressor 3, and D) Stressor 4.

A.7 Reversible and irreversible potential loss calculations

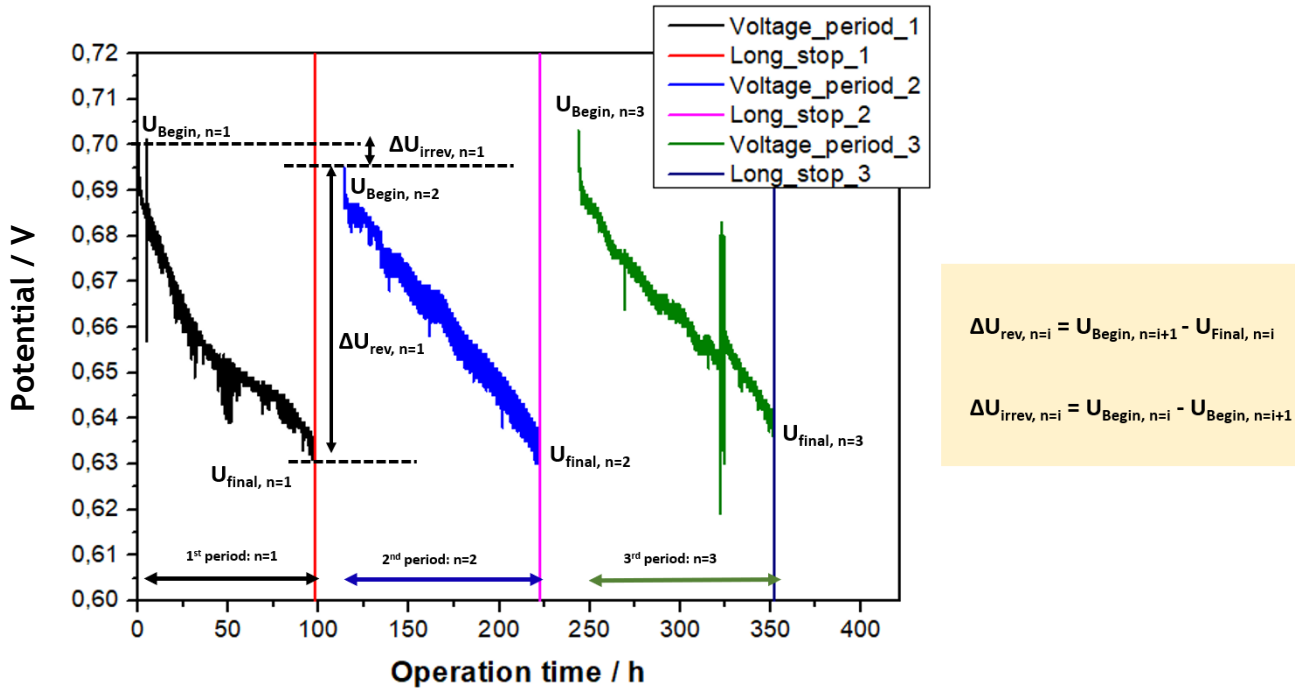

Figure A.7.1 - Reversible, $\Delta U_{rev,i}$, and irreversible potential, $\Delta U_{irrev,i}$, loss calculation exemplification [48]; *Stressor 4 potential evolution over time, for 15 % O_2 feed concentration and HT.*

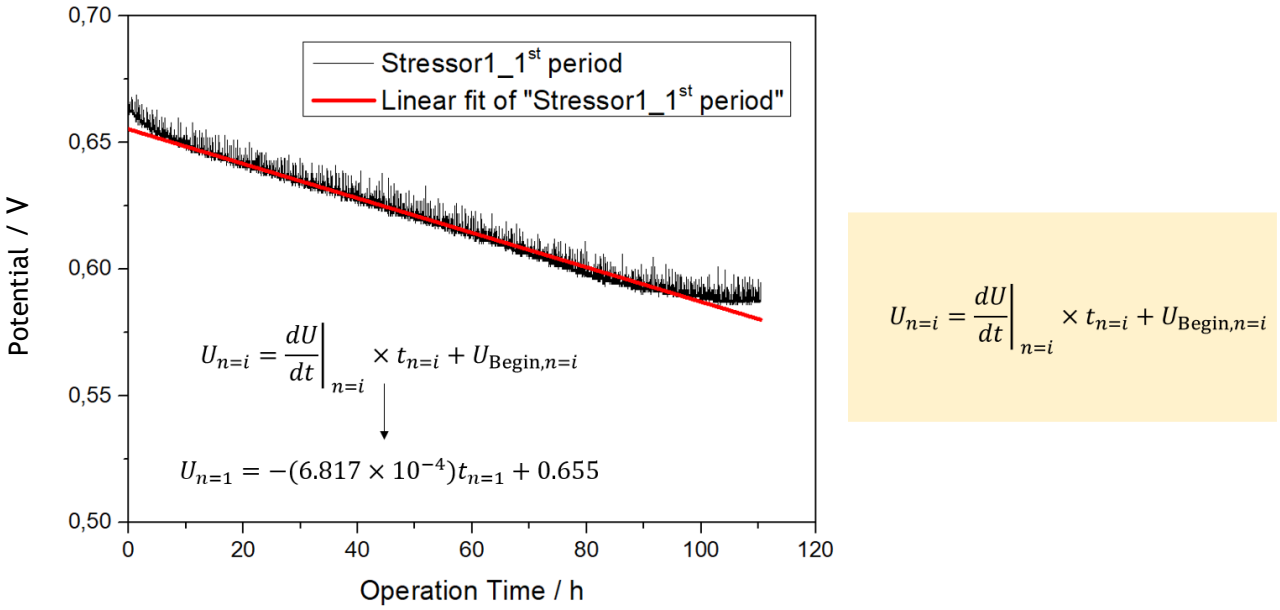

Figure A.7.2 - Potential degradation rate calculation exemplification, from the first period of operation of Stressor 1.

A.8 *In-situ* characterization for stressor tests

Electrochemical Impedance Spectroscopy (EIS)

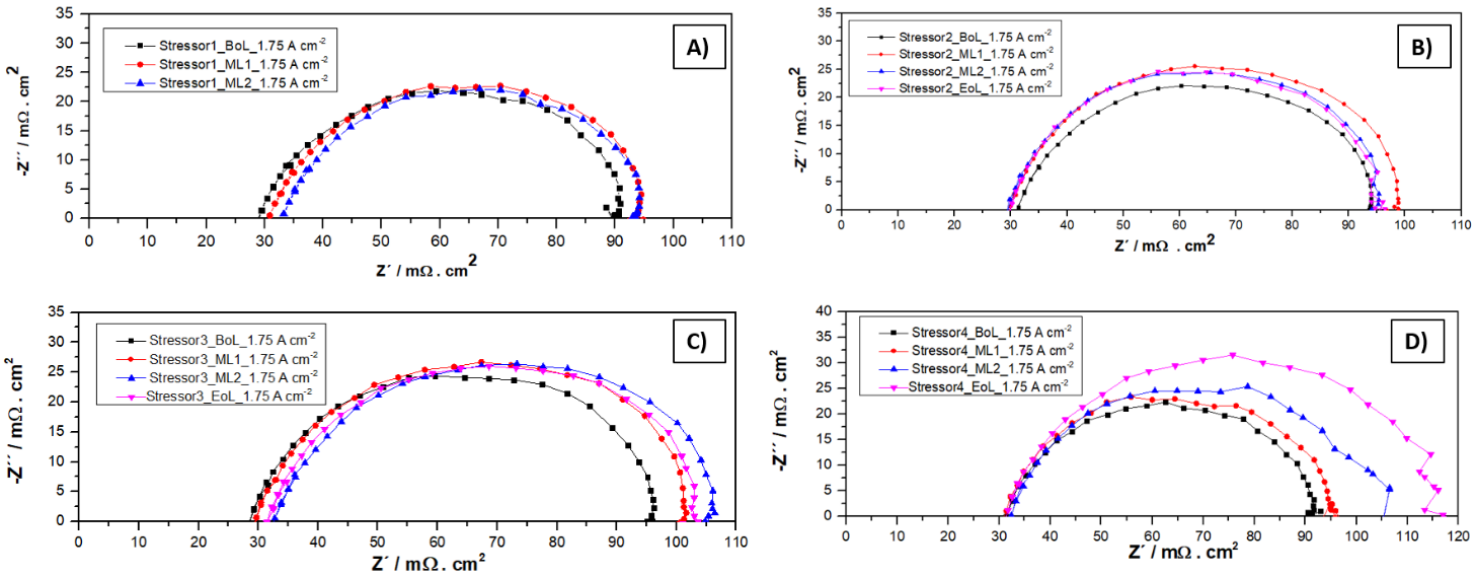

Figure A.8.1 – EIS performed for A) Stressor1; B) Stressor 2; C) Stressor 3; D) Stressor 4, for BoL, ML1, ML2 and EoL characterization, for 500 mA amplitude and 1.75 A·cm^{-2}.

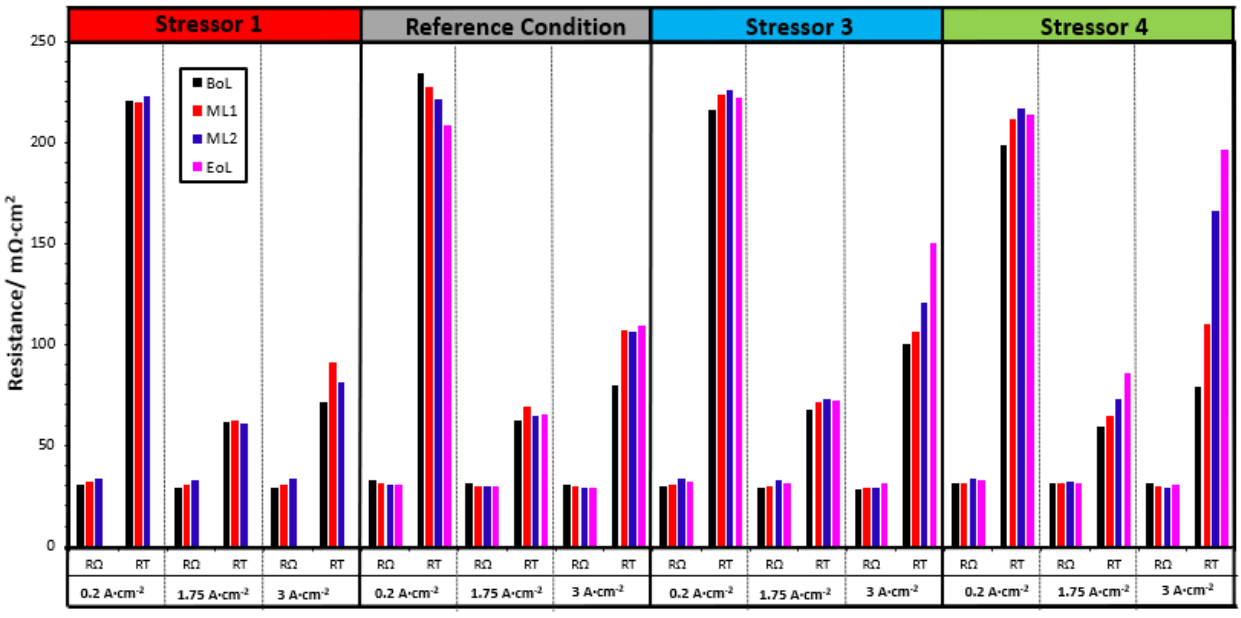

Figure A.8.2 – Ohmic Resistance - R_Ω - and total resistance - R_T - representation, for Stressor 1, 2 , 3 and 4, for BoL, ML1, ML2 and EoL characterization.

Cyclic Voltammetry (CV)

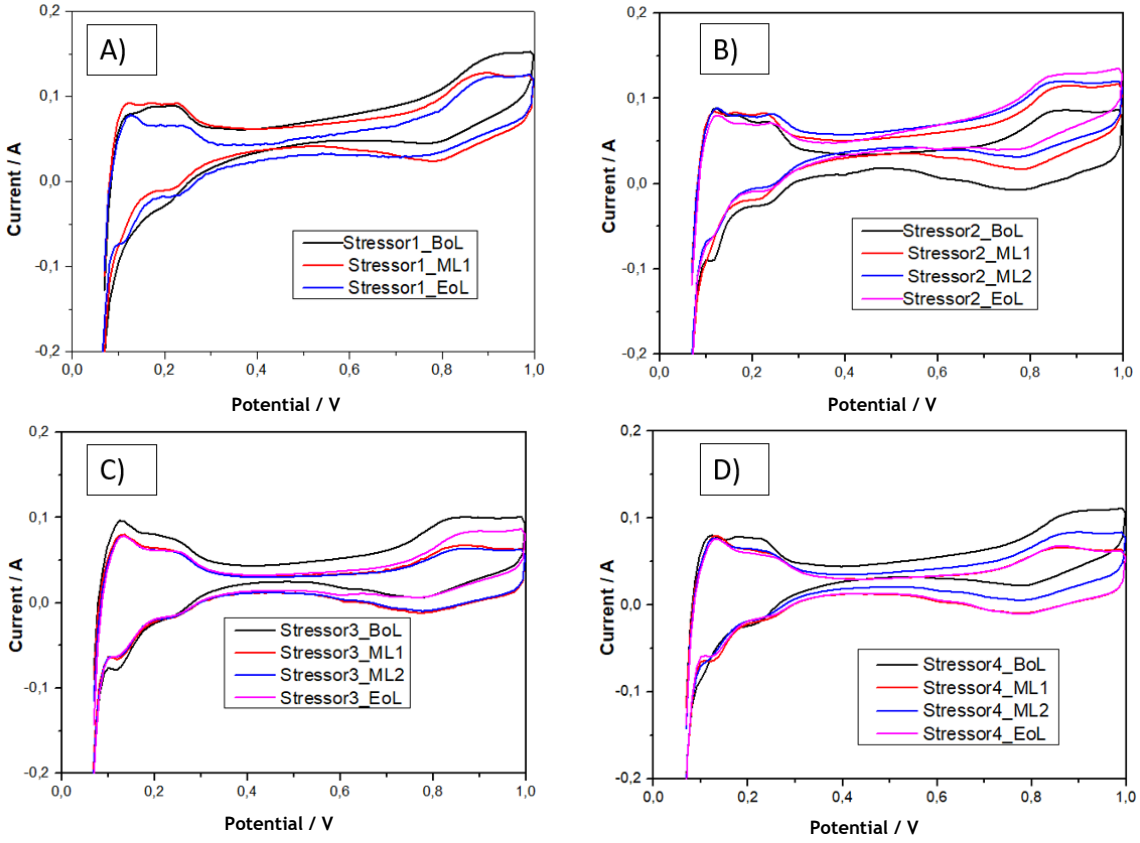

Figure A.8.3 – CV performed for: A) Stressor1; B) Stressor 2; C) Stressor3; D) Stressor4, at ambient pressure and temperature, for BoL, ML1, ML2 and EoL characterization.

Ionic Conductivity Resistance (ICR)

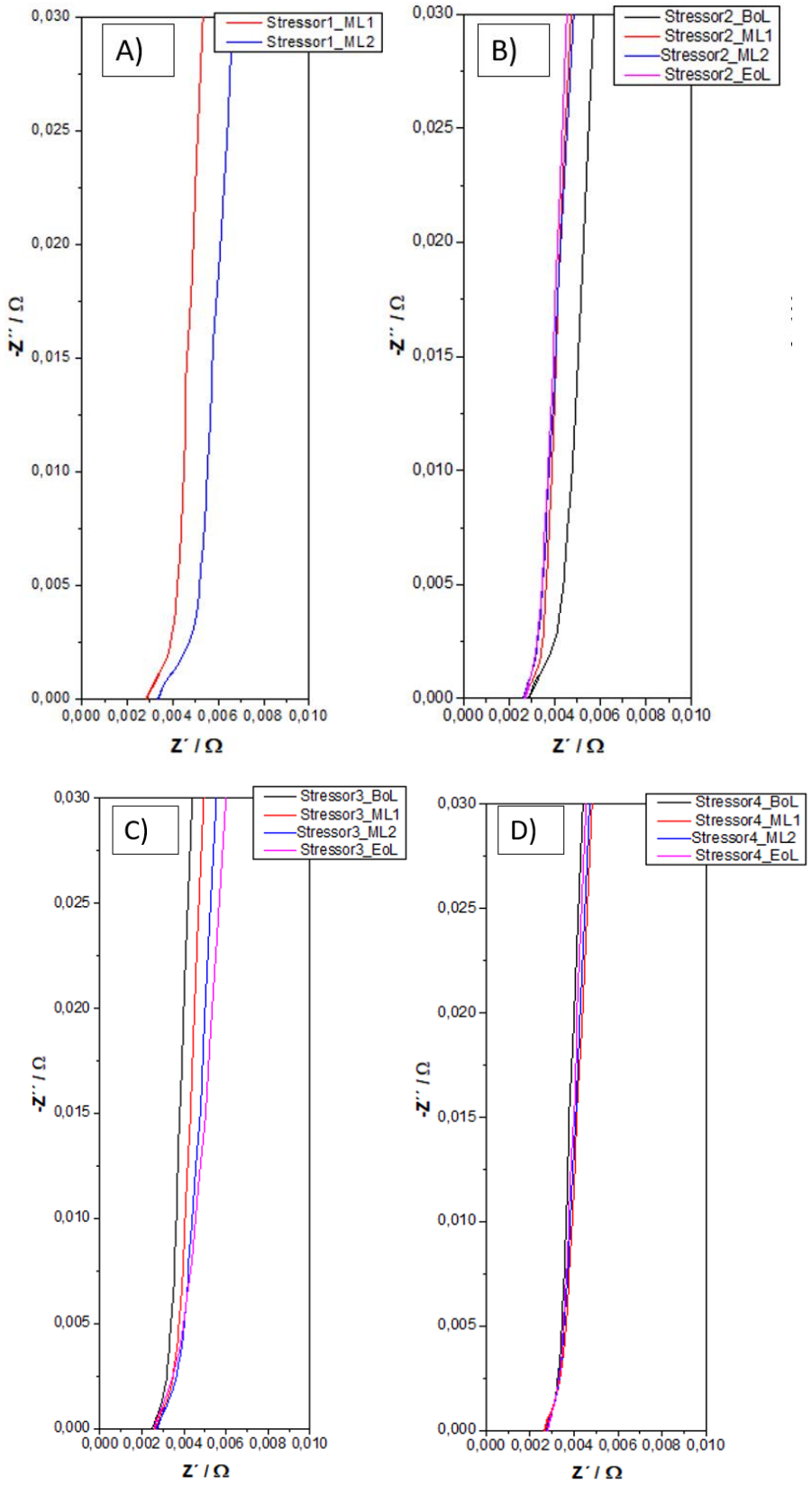

Figure A.8.4 – ICR test performed for: A) Stressor1; B) Stressor2; C) Stressor3; D) Stressor4, at 80 ºC and 1.5 bar outlet pressure (cathode and anode), at 5 mV amplitude and 0.5 V, for BoL, ML1, ML2 and EoL characterization.

Linear Sweep Voltammetry (LSV)

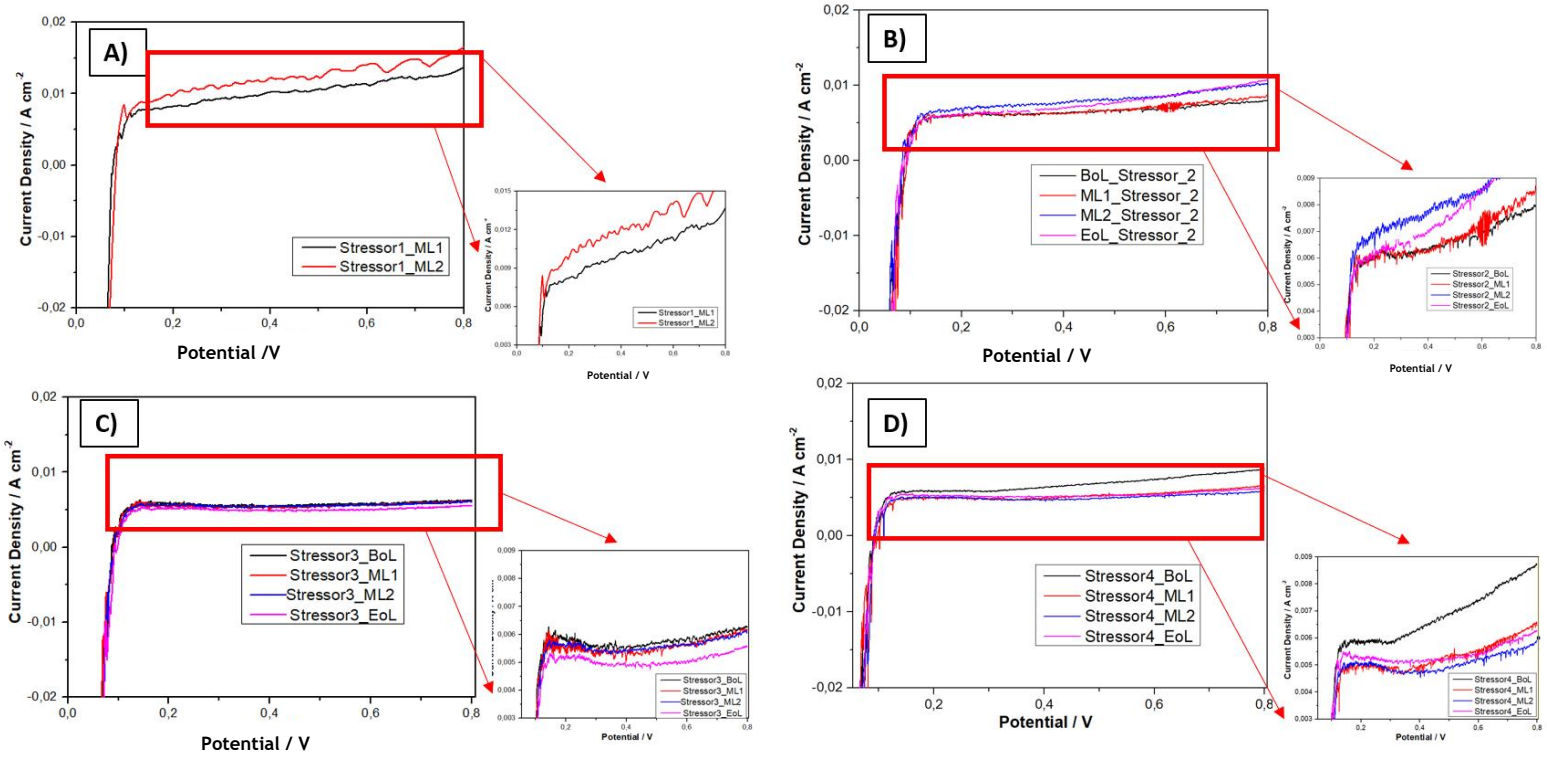

Figure A.8.5 – LSV test performed for: A) Stressor1; B) Stressor2; C) Stressor3; D) Stressor4 at 80 ºC and 1.5 bar outlet pressure (cathode and anode), for BoL, ML1, ML2 and EoL characterization.

A.9 *Equivalent Circuit – Stressor tests*

Table A.9.1 – Contribution of each equivalent circuit element at 3 A cm^{-2} (stressor tests).

		Current density of 3 A cm^{-2}											
		Inductance		Ohmic Resistance		Charge transfer of ORR				Mass transport Resistance			
		I (nH)	Error, %	R_{Ω} (mΩ)	Error, %	$R_{CT,c}$(mΩ)	Error, %	C_1 (mF)	Error, %	$R_{MT,c}$(mΩ)	Error, %	C_2 (mF)	Error, %
Stressor 1	**BoL**	26	1.1	2.2	0.4	1.4	3.4	398	2.5	4.8	1.1	1004	2.7
	ML1	24	3.8	2.5	0.6	1.1	4.5	657	4.3	6.6	0.8	867	2.1
	ML2	25	4.0	2.7	0.6	1.3	4.7	594	3.8	5.6	1.1	935	2.7
Reference condition	**BoL**	37	2.6	2.5	0.4	1.9	2.8	523	1.9	4.9	1.1	1289	2.7
	ML1	32	2.8	2.4	0.4	1.6	5.3	717	2.4	7.5	1.2	915	2.7
	ML2	38	2.8	2.3	0.5	1.4	5.7	909	2.6	7.8	1.0	862	2.3
	EoL	40	2.7	2.4	0.4	1.9	7.2	882	2.8	7.2	1.9	981	3.8
Stressor 3	**BoL**	38	5.6	2.2	1.3	0.9	8.5	790	9.9	8.2	1.1	789	3.0
	ML1	34	3.1	2.4	0.5	1.4	5.2	718	2.9	7.5	1.0	859	2.5
	ML2	43	2.4	2.3	0.5	1.4	4.2	803	2.4	8.8	0.7	795	1.7
	EoL	40	3.1	2.5	0.7	1.0	4.6	812	5.6	11.3	0.5	700	1.3
Stressor 4	**BoL**	58	2.3	2.4	0.5	1.9	2.8	546	1.9	4.8	1.2	1212	2.6
	ML1	50	3.6	2.4	0.7	1.8	7.1	698	3.3	7.5	1.8	930	4.0
	ML2	54	5.8	2.3	1.0	2.1	10.8	816	4.5	12.6	1.8	816	4.6
	EoL	47	3.6	2.5	0.8	1.5	8.7	848	4.7	14.8	1.0	646	2.5

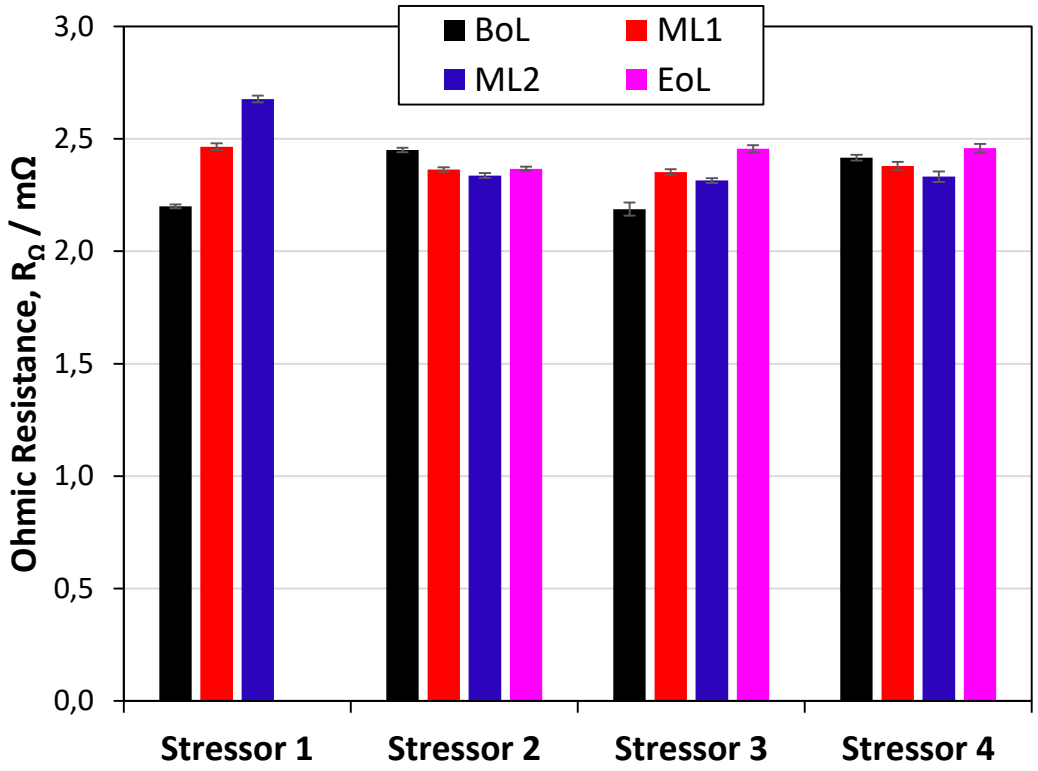

Figure A.9.1 – Bar chart with Ohmic resistance (R_Ω), from EC model, for BoL, ML1, ML2 and EoL stressor tests.

A.10 *Cell efficiency Determination*

Table A.10.1 - Determination of cell efficiency for stressor tests, at 21 A, from polarisation curves.

	Stressor 1				Stressor 2				Stressor 3				Stressor 4			
	BoL	ML1	ML2	EoL	BoL	ML1	ML2	EoL	BoL	ML1	ML2	EoL	BoL	ML1	ML2	EoL
Potential at 1.75 A/cm² (V)	0.691	0.696	0.614	-----	0.684	0.687	0.663	0.695	0.705	0.677	0.663	0.671	0.689	0.684	0.670	0.665
Potential efficiency $\eta_{Potential}$ (%)	57.3	57.8	51.0	-----	56.8	57.1	57.9	57.7	58.5	56.2	55.1	55.7	57.2	56.8	55.6	55.2
Energy efficiency η_{cell} (%)	45.0	45.3	40.0	-----	44.5	44.7	45.4	45.3	45.9	44.1	43.2	43.7	44.9	44.6	43.6	43.3

For cell efficiency determination, η_{cell}, the following equations were used:

$$\eta_{\text{cell}} = \eta_{\text{Coulombic}} \times \eta_{\text{Thermo}} \times \eta_{\text{Potential}}, \quad \eta_{\text{Coulombic}} \approx 100\ \% \tag{32}$$

$$\eta_{\text{Thermo}} = \frac{-\Delta G_{353\ \text{K}}}{-\Delta H_{353\ \text{K}}} = 78.4\ \% \tag{33}$$

$$\eta_{\text{Potential}} = \frac{E_{\text{cell}(1.75\ \text{A.cm}^{-2})}}{E_{\text{Thermo}(353\ \text{k})}} \tag{34}$$

$$E_{\text{Thermo}(353\ \text{k})} = E_{\text{rev}} - \frac{RT}{nF} \ln\left[\frac{P_{H_2O}}{P_{H_2} P_{O_2}^{0.5}}\right] \tag{35}$$

A.11 CCM_1 thickness determination with SEM analysis (epoxy resin impregnation)

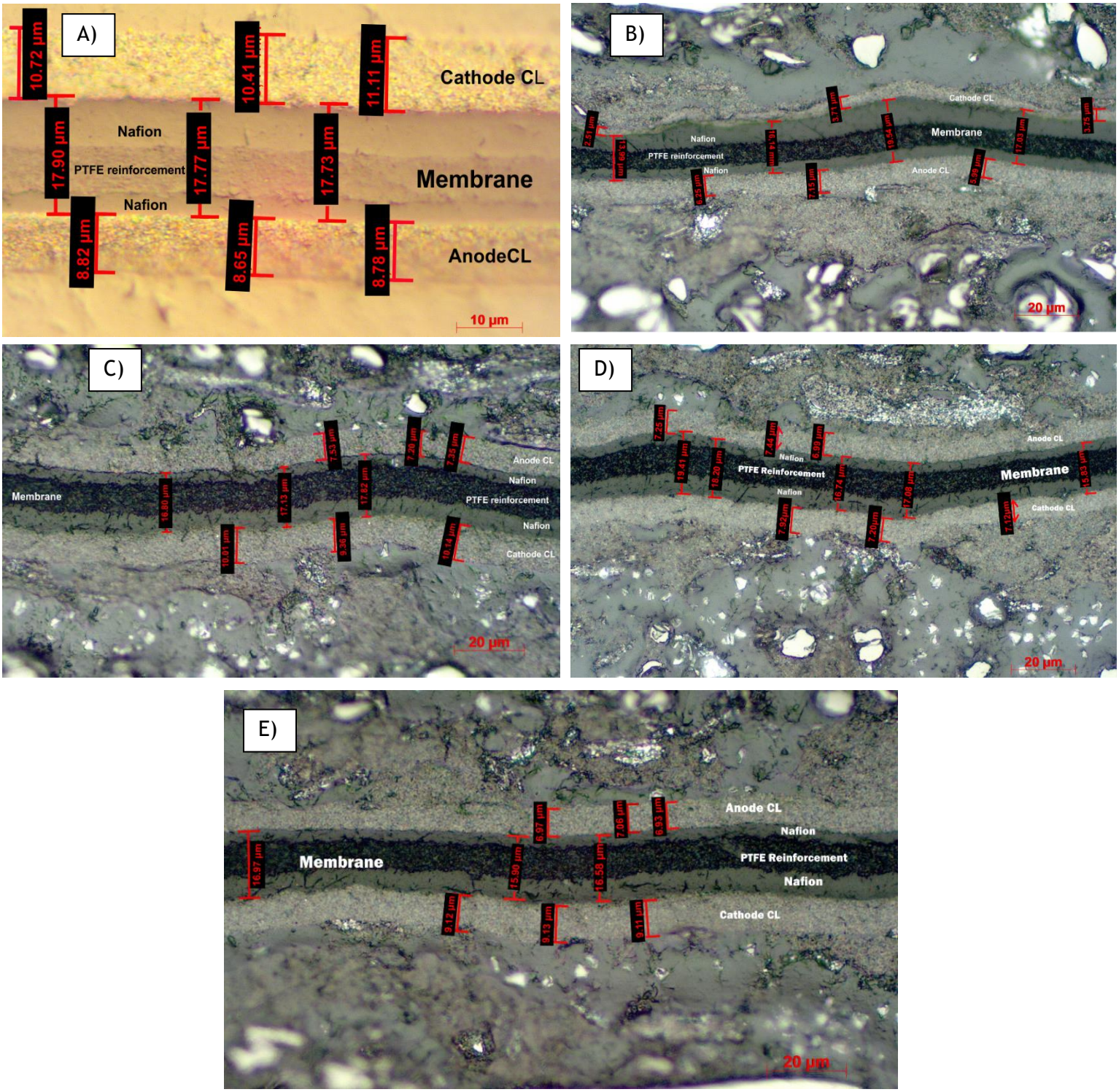

Figure A.11.1 – SEM images of cross sections of middle area CCM_1 prepared with epoxy resin impregnation: A) pristine CCM_1; B) Aged CCM_1 with 400 cycles with 17.7 % O2 feed concentration; C) Aged CCM_1 with Stressor 1; D) Aged CCM_1 with Stressor 2; E) Aged CCM_1 with Stressor 3.

A.12 CCM_2 thickness determination with SEM analysis (epoxy resin impregnation)

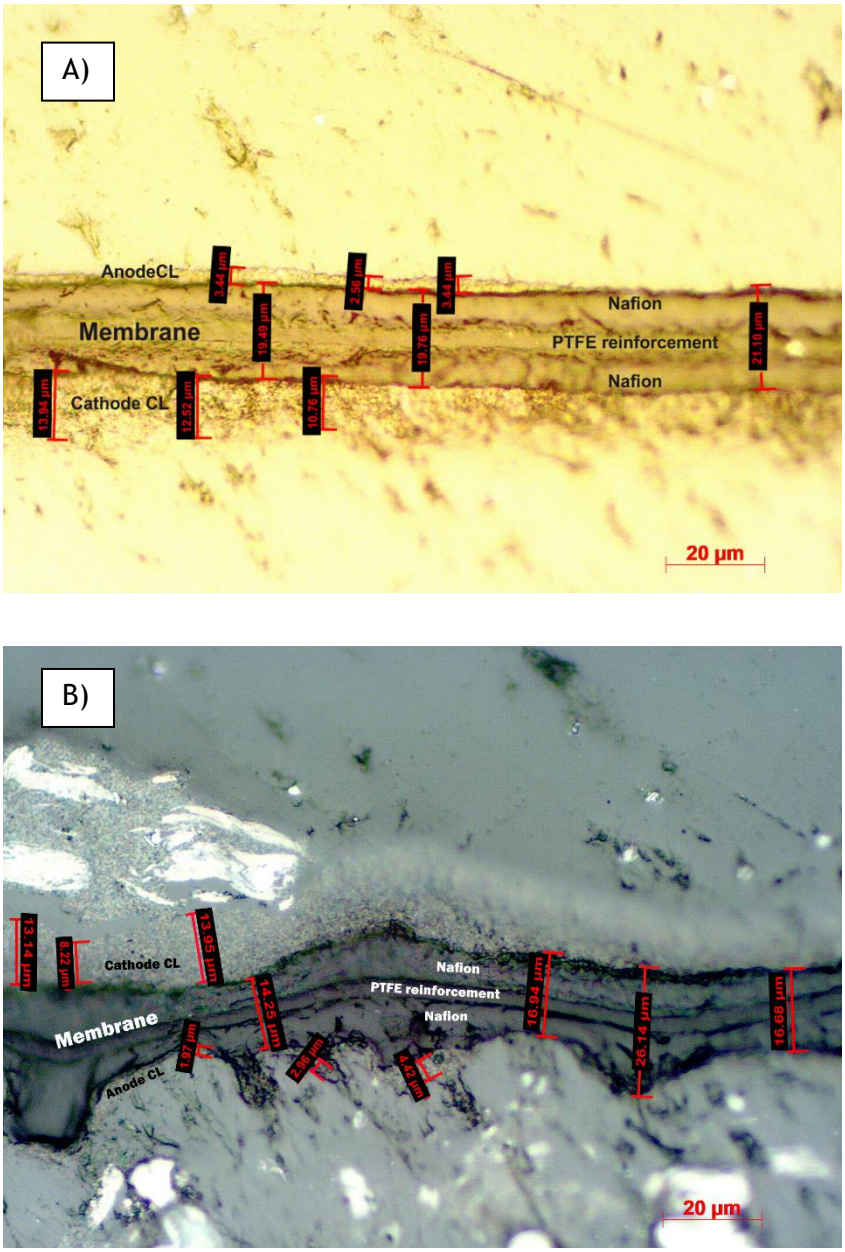

Figure A.12.1 – SEM images of cross sections of middle area CCM_2 samples prepared with epoxy resin impregnation: A) pristine CCM_2; B) Aged CCM_2 with 400 cycles with 15 % O_2 feed concentration.

A.13 SEM images of aged cross sections from middle CCM

Stressor 1

A) Stressor 1: Ion cut

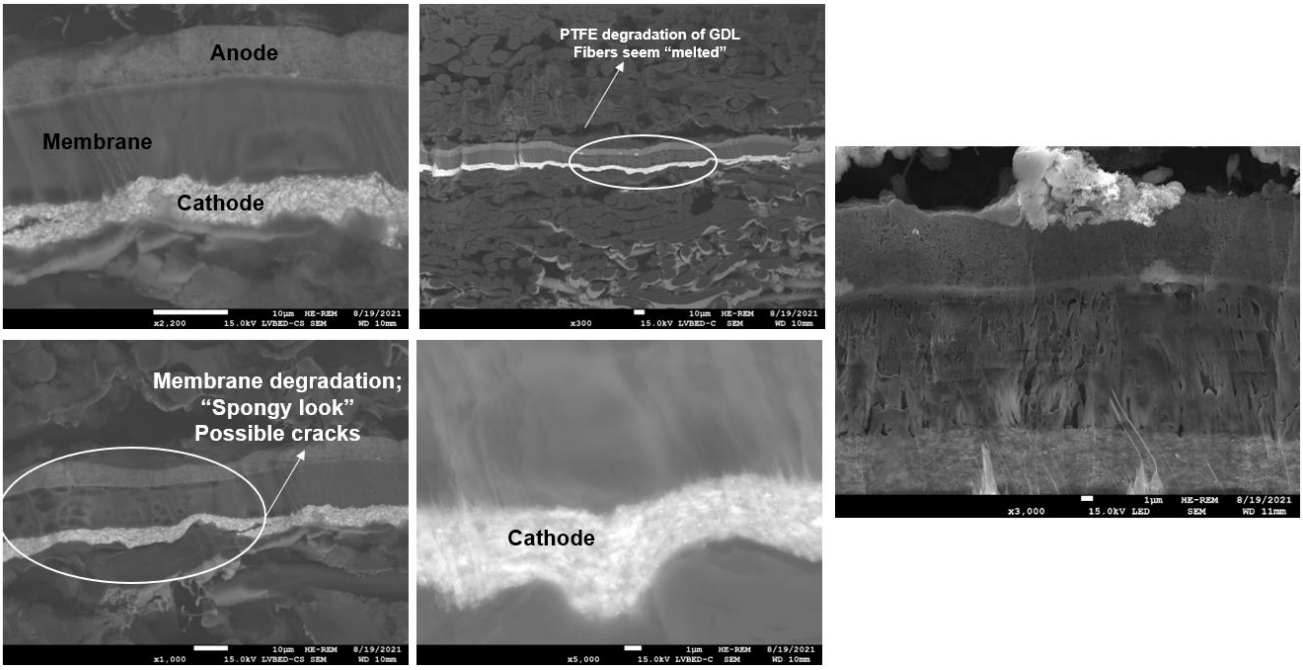

B) Stressor 1: Epoxy resin impregnation

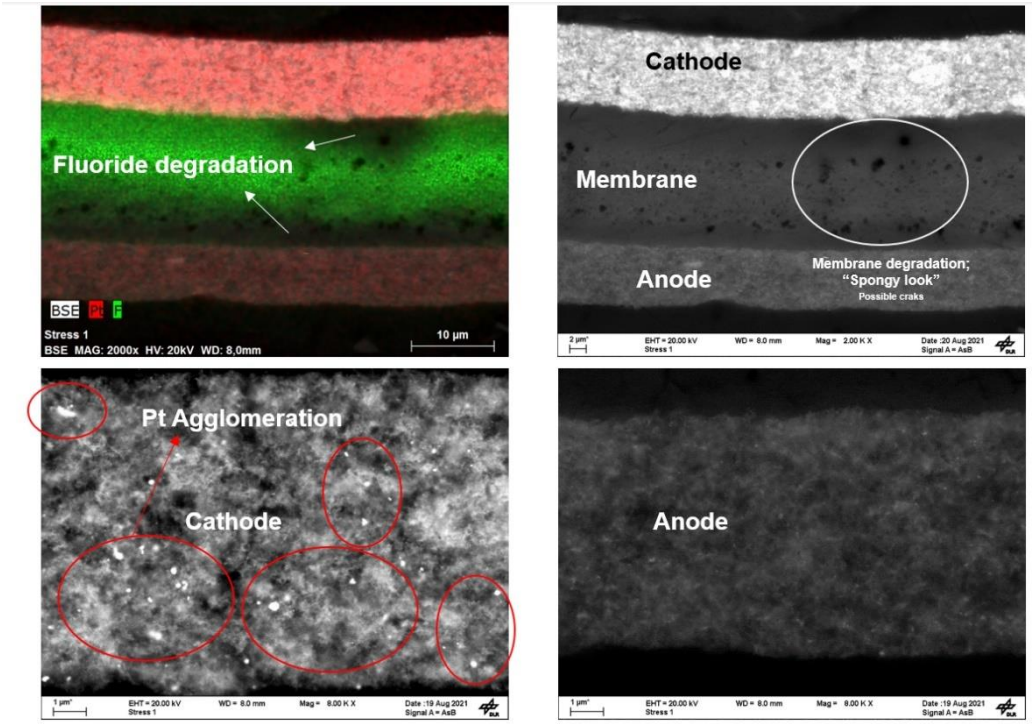

Figure A.13.1 – SEM images and mapping of cross sections of middle area aged CCM_1 from Stressor 1 EoL, prepared with A) ion cut and B) epoxy resin impregnation.

Stressor 2 – Reference condition

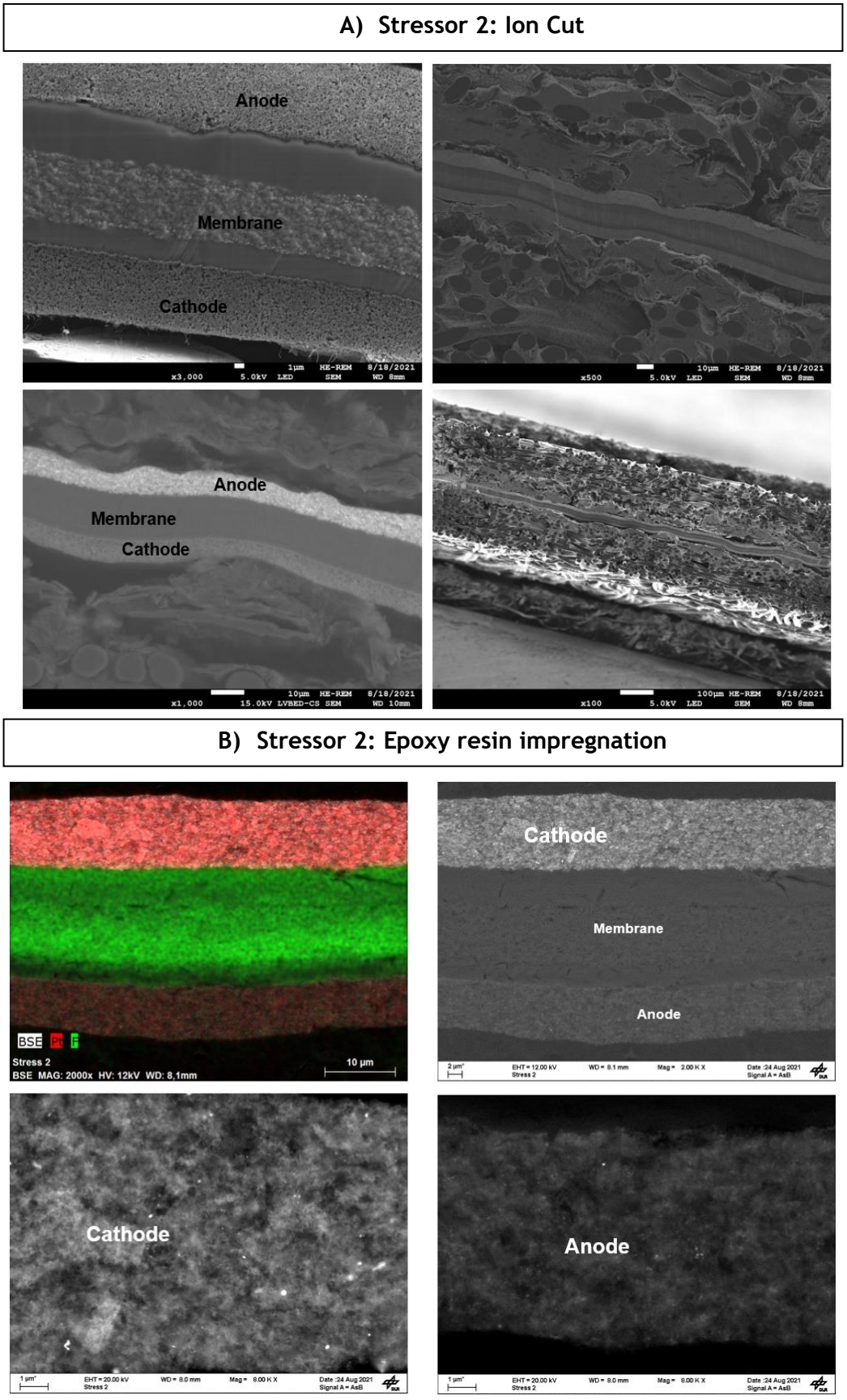

Figure A.13.2 – SEM images and mapping of cross sections of middle area aged CCM_1 from Stressor 2/Reference condition EoL, prepared with A) ion cut and B) epoxy resin impregnation.

Stressor 3

A) Stressor 3: Ion Cut

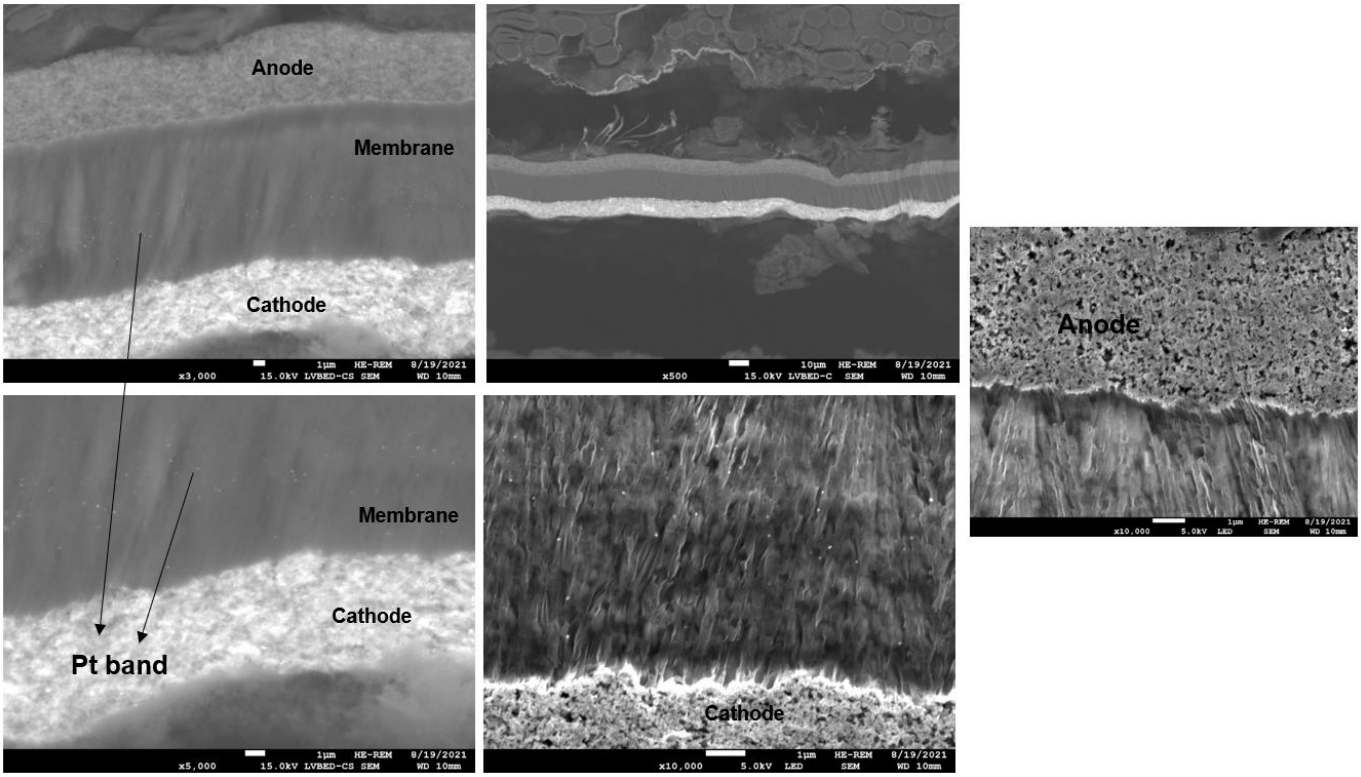

B) Stressor 3: Epoxy resin impregnation

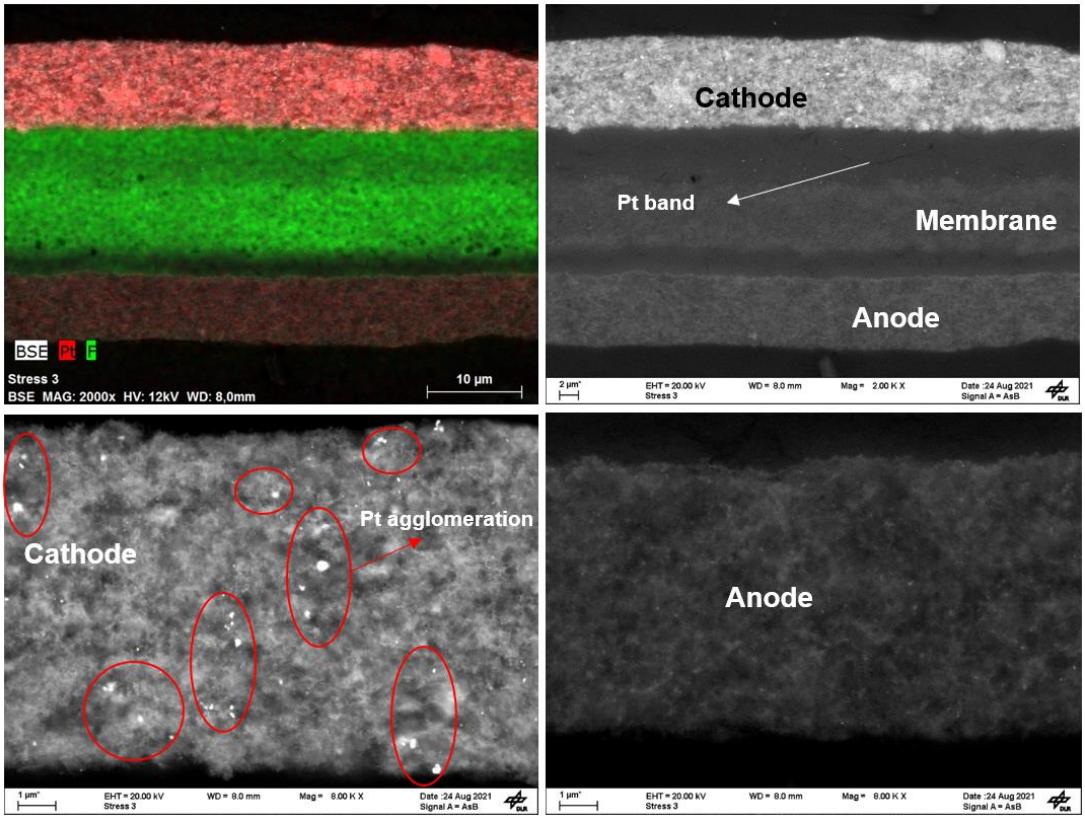

Figure A.13.3 – SEM images and mapping of cross sections of middle area aged CCM_1 from Stressor 3 EoL, prepared with A) ion cut and B) epoxy resin impregnation.

Driving cycle with 17.7 % O2 feed concentration

A) Driving cycle with 17.7 % O2 feed concentration: Ion Cut

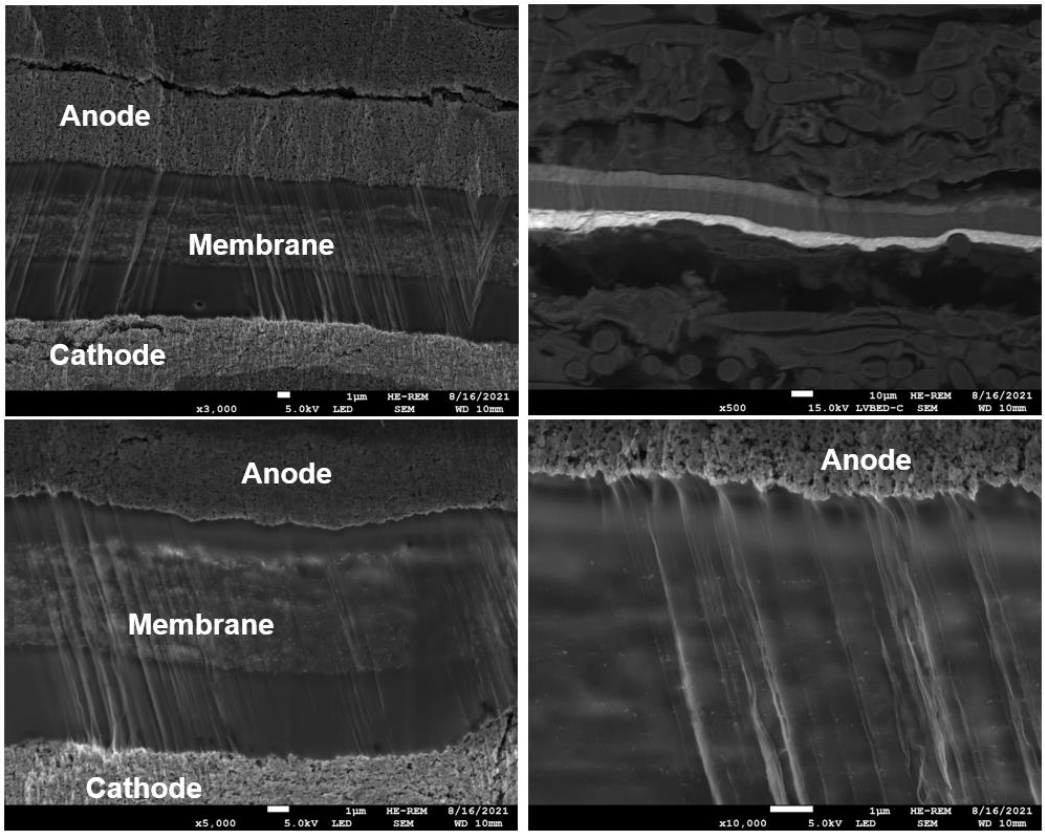

B) Driving cycle with 17.7 % O2 feed concentration: Epoxy resin impregnation

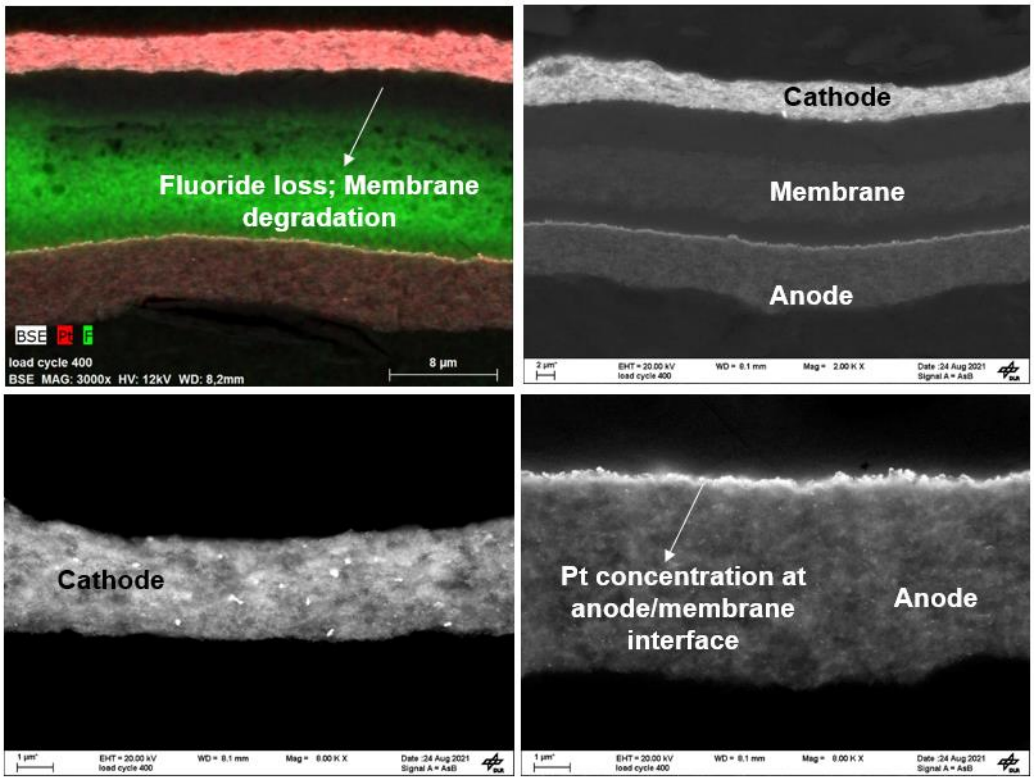

Figure A.13.4 – SEM images and mapping of cross sections of middle area aged CCM_1 from driving cycle with 17.7 % O_2 feed concentration, prepared with A) ion cut and B) epoxy resin impregnation.

A.14 EDX analysis results

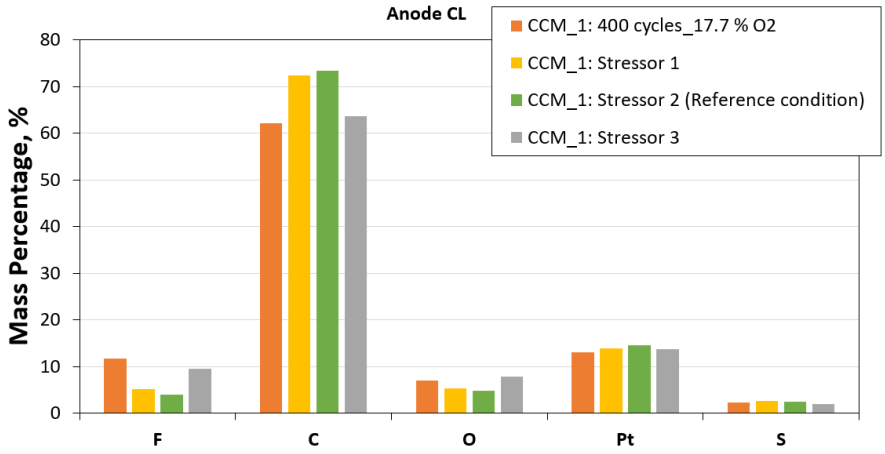

Figure A.14.1 – Anode CL elements' mass percentage, for stressor and driving cycle tests, determined by EDX, through cross sections from middle CCM prepared by epoxy resin impregnation method.

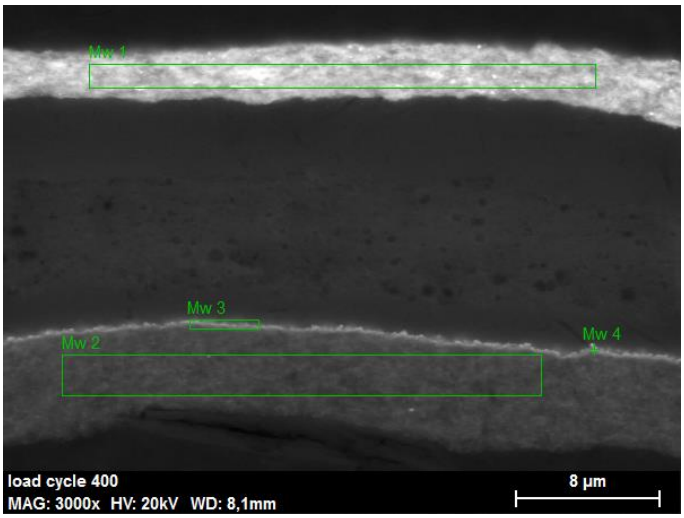

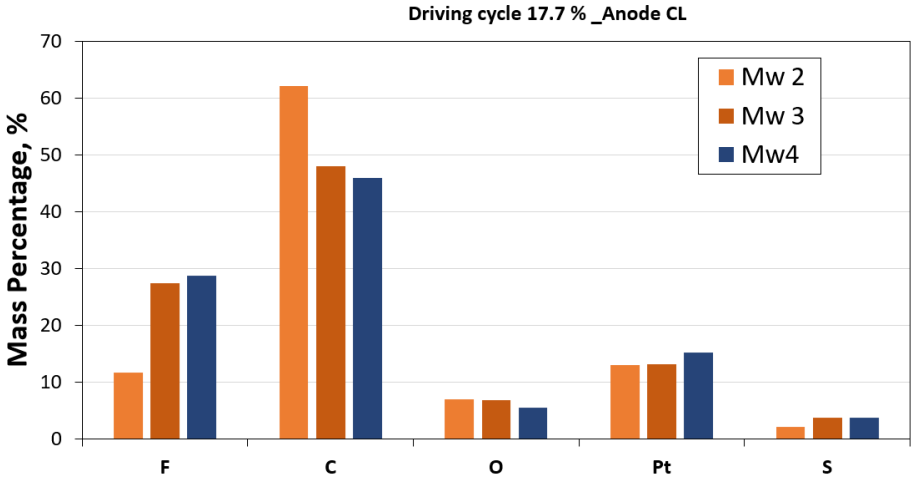

Figure A.14.2 – Anode CL elements´ mass percentage, for driving cycle test with 17.7 % O_2 feed concentration *with CCM_1, determined by EDX, through cross sections from middle CCM prepared by epoxy resin impregnation method.*

A.15 XPS analysis results

XPS Spectra

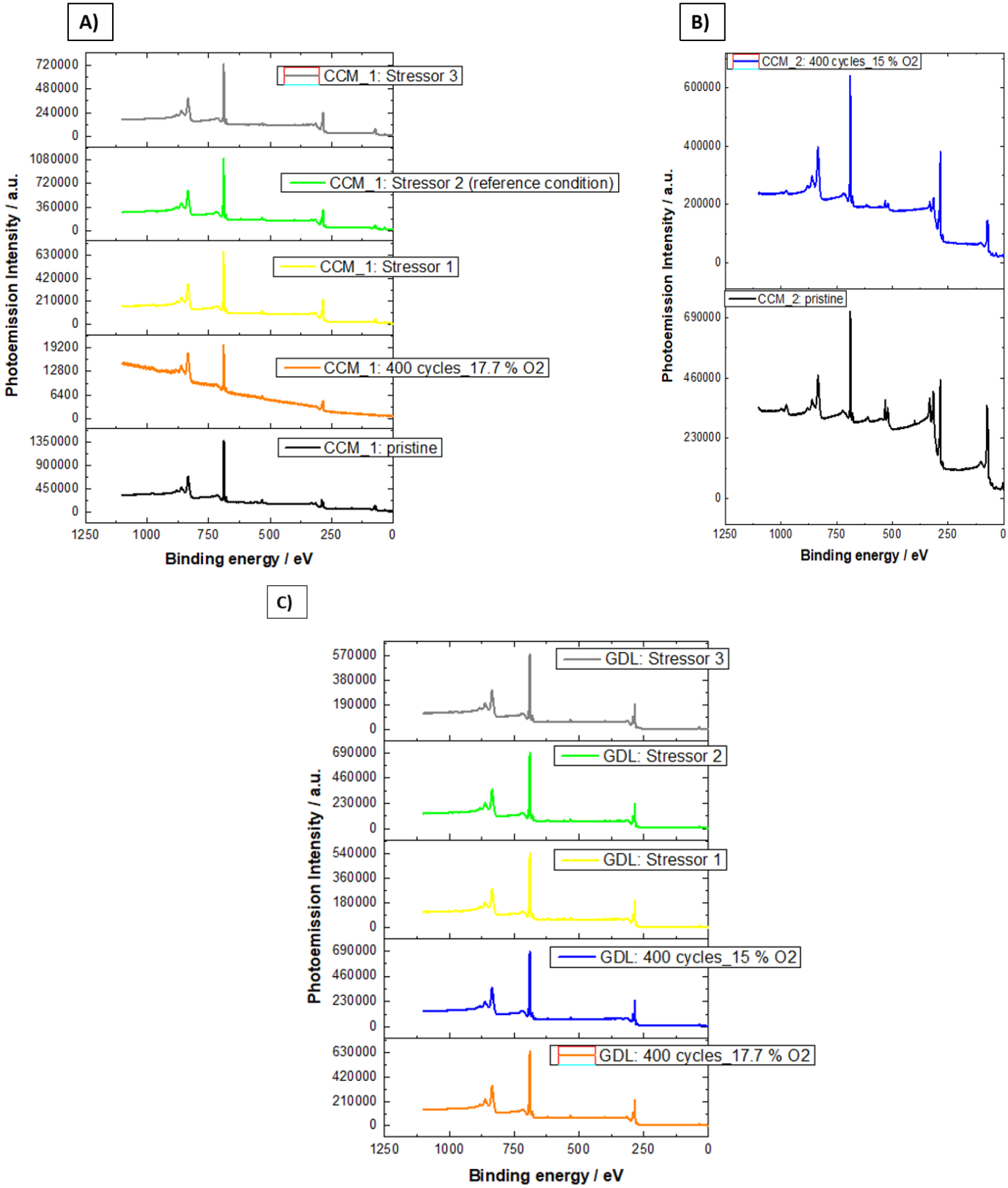

Figure A.15.1 – XPS spectra of A) CCM_1 aged and pristine samples from cathode side; B) CCM_2 aged and pristine samples from cathode side; C) Aged GDL from cathode side.

XPS Analysis

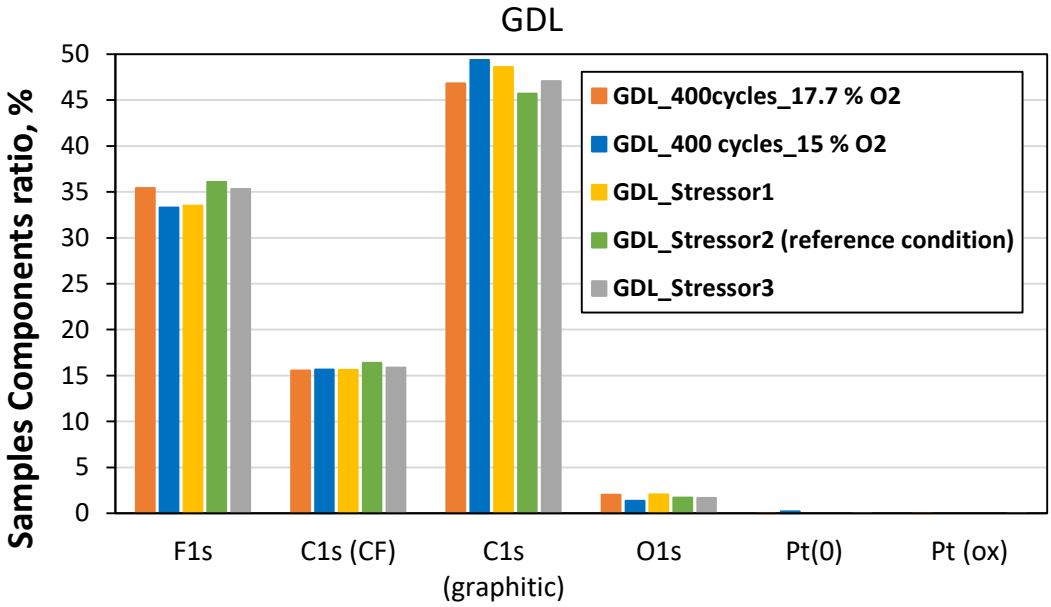

Figure A.15.2 - Bar chart of XPS analysis of aged commercial GDL, from the cathode side, for stressor and driving cycle tests performed.